Nanoscale Assembly Using DNA and Electromagnetic Fields

Antti-Pekka Eskelinen

Nanoscale Assembly Using DNA and Electromagnetic Fields

Antti-Pekka Eskelinen

A doctoral dissertation completed for the degree of Doctor of Science (Technology) (Doctor of Philosophy) to be defended, with the permission of the Aalto University School of Science, at a public examination held at the lecture hall Y124 of the school on 4 October 2013 at 12.

Aalto University
School of Science
Department of Applied Physics
Quantum Dynamics

Supervising professor
Prof. Päivi Törmä

Thesis advisors
Prof. Olli Ikkala
Prof. Mauri Kostiainen

Preliminary examiners
Prof. Martti Kauranen, Tampere University of Technology, Finland.
Prof. Markus Linder, Aalto University, Espoo.

Opponent
Prof. Tim Liedl, Ludwig-Maximilians-Universität, Germany.

NORDIC ECOLABEL

441   697
Printed matter

Abstract

In this work we demonstrate the control of nanoparticles and nanostructures with the help of the DNA origami method and dielectrophoresis. DNA nanotechnology is a subfield of nanotechnology where DNA is used as a construction material. The DNA origami method is a recent development in the field which enables the assembly of nanoparticles with nanometer scale accuracy through self-assembly. Here we take advantage of the method for efficient deposition and alignment of single-walled carbon nanotubes (SWCNTs). Especially the alignment of SWCNTs on substrates has been a major challenge for commercialization of SWCNT based devices, to which our approach could offer a potential solution. As an example, a crossed carbon nanotube junction, a basic geometry for a carbon nanotube transistor, is constructed. The high yields of assembled structures as well as correct alignment of SWCNTs are verified with atomic force microscopy.

The DNA origami method is used also for assembling a bow-tie antenna configuration from silver nanoparticles. The optical response of the system is based on the hybridization of the individual nanoparticle surface plasmon resonance modes. The formation of the structures is verified with transmission electron microscopy and complemented with agarose gel electrophoresis. The configuration could have potential use as an optical DNA sensor. The sensor performance is investigated with finite-difference time-domain numerical simulations. In addition to assembling nanoparticles, control over the DNA origami structure itself is demonstrated with dendrons and external trigger signals. Efficient control over the structure formation is investigated with atomic force microscopy, agarose gel electrophoresis and dynamic light scattering experiments. The external trigger signals can be chosen by choosing the dendron structure. We demonstrate our concept with dendrons which can be triggered either with UV-radiation or with a mild reducing agent such as dithiothretoil.

Dielectrophoresis is an electromechanical technique for manipulating micro-and nanoparticles. Here the method is used for developing a new nanoimprint lithographic technique named field-induced nanoimprint lithography. In this technique nanoelectrodes are used for producing dielectrophoretically a pattern of nanoparticles on a re-usable master stamp, which is then used for transferring the nanoparticle pattern on a target substrate by mechanical contact. Dielectrophoresis is also used for producing chains of gold nanoparticles between nano- and microelectrodes. The chains are investigated for sensing purposes with impedance studies.

Tiivistelmä

   Tämä väitöskirja käsittelee nanohiukkasten ja nanorakenteiden kontrollointia nanomittakaavassa DNA-origami-tekniikan sekä dielektroforeesin avulla. DNA-origami-tekniikka on DNA-nanoteknologian viimeaikaisimpia saavutuksia, jossa DNA:a käytetään geneettisen informaation säilömisen sijaan rakennusmateriaalina. Tässä väitöskirjassa DNA-rakenteita käytetään etenkin erilaisten nanopartikkelien kiinnittämiseen ja asemoimiseen. Ensimmäisenä DNA-origamien sovellutuskohteena osoitamme menetelmän yksiseinäisten hiilinanoputkien kontrolloituun asemoimiseen. Osoitamme lähestymistavan tehokkuuden muun muassa rakentamalla ristiliitoksen kahdesta yksiseinäisestä hiilinanoputkesta - rakenteen, jota voi käyttää hiilinanoputkitransistorina. Vastaavanlaisia rakenteita on erittäin vaikea tuottaa kontrolloidusti perinteisillä menetelmillä, mikä on ollut yksi este hiilinanoputkiin perustuvien laitteiden kaupallistamisessa.

   Hiilinanoputkien asemoinnin lisäksi sovellamme DNA-origami-tekniikkaa antennirakenteen kokoamiseen hopeananohiukkasista. Todistamme rakenteiden syntymisen atomivoima- sekä läpäisyelektronimikroskoopin avulla. Varmennamme tuloksemme myös geelielektroforeesin avulla. Yhtenä antennirakenteemme sovellutuksena voi olla DNA-anturi; tutkimme myös rakenteemme soveltuvuutta kyseiseen tarkoitukseen numeeristen simulaatioiden avulla. Viimeisenä DNA-origami-tekniikkaan liittyvänä tutkimuksena osoitamme, kuinka DNA-rakennetta itseään voidaan kontrolloida dendronien sekä ulkoisten signaalien avulla. Osoitamme atomivoimamikroskooppi-, geelielektroforeesi- sekä dynaamisten valonsirontakokeiden avulla pystyvämme tehokkaasti kontrolloimaan DNA-rakenteiden muodostumisen. Kontrollisignaalit määräytyvät käytettyjen dendronirakenteiden mukaan. Kokeissamme kontrollisignaaleja ovat ultraviolettivalo sekä mieto redusoiva aine dithiothretoil.

   Dielektroforeesi on elektromekaaninen menetelmä, jonka avulla voi kontrolloida mikro- sekä nanokokoluokan hiukkasia sähkökenttien gradienttien avulla. Käytämme metodia uuden nanopainamismenetelmän kehittämiseen. Menetelmän pääkomponentti on leimasin, johon kuvioimme nanoelektrodit. Käytämme näitä elektrodeja muodostamaan haluttuja kuvioita nanohiukkasista sähkökenttien gradienttien avulla. Lopulta siirrämme kyseisen kuvion halutulle alustalle mekaanisen painamisen avulla. Nanopainamismenetelmän lisäksi käytämme dielektroforeesia muodostaaksemme nanohiukkasketjuja kultananohiukkasista mikro- sekä nanoelektrodien avulla. Teemme myös impedanssimittauksia kyseisillä ketjuilla anturisovellutusta varten.

Preface

This thesis is a summary of work conducted during the years 2007-2013 at University of Jyväskylä and at Aalto University. I have had an opportunity to work in an innovative and inspiring environment with special people. In my opinion it would not be possible for me to write these words without these people.

First and foremost I would like to thank my supervisor Prof. Päivi Törmä for her excellent guidance. I am especially grateful for her entrusting me to take responsibility over my research tasks, which has enabled me to accomplish a huge personal growth during the years. I think that it is needless to say what a major impact her intuition and wisdom in science has had on the outcome of this thesis. I am also extremely grateful for her support during hard times and for the guidance she has given me concerning career and personal life.

In addition I owe a huge gratitude to Dr. Anton Kuzyk for his persistent guidance and for introducing me to the world of DNA nanotechnolgy. Dr. Mauri M. Kostiainen deserves also special mentioning for his inspiring guidance, it has been a true joy to work with him in several projects. I would like also to thank my thesis pre-examiners Prof. Martti Kauranen and Prof. Markus Linder. With the help of their comments, I was able to improve the thesis considerably. Moreover I would like to thank following persons for fruitful discussions and assistance during my PhD studies as well as for their friendship. Sincere thank you to Mr. Kevin Franke, Dr. Tommi Hakala, Mr. Jukka Hassinen, Mr. Miikka Heikkinen, Dr. Jussi Kajala, Mr. Toni K. Kaltiaisenaho, Dr. Andreas Johansson, Dr. Jami Kinnunen, Ms. Anna Korolyuk, Dr. Tuomas Lahtinen, Mr. Lauri Lehtola, Dr. Veikko Linko, Dr. Jani-Petri Martikainen, Dr. Francesco Massel, Mr. Joona Mikkilä, Mr. Heikki Rekola, Dr. Marcus Rinkiö, Dr. Marina Y. Timmermans, Dr. Jussi Toppari, Ms. Anne-Maria Visuri, Mr. Aaro Väkeväinen, and Mrs. Laura Äkäslompolo.

In addition I want to thank Mr. Jaakko Halkosaari, Ms. Anna Kalliola, Mr.

Sampo Kulju, Mr. Mikko Palosaari and Mr. Marko Vatanen for friendship and assistance in introducing me to the world of physics.

I dedicate this thesis to my family; my parents Ossi and Sirkka Eskelinen, my little sister Anna Laine, my daughter Niina Lyydia Eskelinen and to my wife Kaisa Teräväinen. I think I can without hesitation say that without them this thesis had never seen the daylight.

Helsinki, September 9, 2013,

Antti-Pekka Eskelinen

Contents

List of Publications

This thesis consists of an overview and of the following publications which are referred to in the text by their Roman numerals.

I A.-P. Eskelinen, A. Kuzyk, T. K. Kaltiaisenaho, M. Y. Timmermans, A. G. Nasibulin, E. I. Kauppinen, and P. Törmä. Assembly of Single-Walled Carbon Nanotubes on DNA-Origami Templates through Streptavidin-Biotin Interaction. *Small*, 7, 6, 746-750, 3 2011.

II A.-P. Eskelinen, R. J. Moerland, M. A. Kostiainen, and P. Törmä. Self-Assembled Silver Nanoparticles in a Bow-Tie Antenna Configuration. *Submitted to Small*, 29 pages 2013.

III A.-P. Eskelinen, H. Rosilo, A. Kuzyk, P. Törmä, and M. A. Kostiainen. Controlling the Formation of DNA Origami Structures with External Signals. *Small*, 8, 13, 2016-2020, 9 2012.

IV T. K. Hakala, V. Linko, A.-P. Eskelinen, J. J. Toppari, A. Kuzyk, and P. Törmä. Field-Induced Nanolithography for High-Throughput Pattern Transfer. *Small*, 5, 23, 2683-2686, 12 2009.

V C. Leiterer, S. Berg, A.-P. Eskelinen, A. Csaki, M. Urban, P. Törmä, and W. Fritzsche. Assembling Gold Nanoparticle Chains Using an AC Electrical Field: Electrical Detection of Organic Thiols. *Sensors and Actuators B: Chemical*, 176, 368-373, 1 2013.

Author's Contribution

Publication I: "Assembly of Single-Walled Carbon Nanotubes on DNA-Origami Templates through Streptavidin-Biotin Interaction"

The author did most of the experimental work. The author was the main writer of the paper.

Publication II: "Self-Assembled Silver Nanoparticles in a Bow-Tie Antenna Configuration"

The author did all the experimental work, and conducted the simulation studies. The author interpreted the results and wrote the paper together with the co-authors.

Publication III: "Controlling the Formation of DNA Origami Structures with External Signals"

The author did the experimental work with the DNA origami structures and dendrons. The author was the main writer of the paper.

Publication IV: "Field-Induced Nanolithography for High-Throughput Pattern Transfer"

The author took part in sample fabrication, trapping experiments and optical imaging. The author optimized the binding chemistry for target plate binding (PDACMAC).

Publication V: "Assembling Gold Nanoparticle Chains Using an AC Electrical Field: Electrical Detection of Organic Thiols"

The author fabricated the nanoelectrodes for the measurements, participated in electrical measurements in Espoo, Finland and in Jena, Germany. The author participated also in the imaging of the results and writing of the paper.

Other publications to which the author has contributed:

A A. I. Väkeväinen, R. J. Moerland, H. T. Rekola, A.-P. Eskelinen, J.-P. Martikainen, D.-H. Kim, and P. Törmä, Plasmonic surface lattice resonances at the strong coupling regime, *In review Nat. Commun.*, 2013.

B R. J. Moerland, H. T. Rekola, G. Sharma, A.-P. Eskelinen, A. I. Väkeväinen, and P. Törmä, Surface plasmon polariton-controlled tunable quantum-dot emission, *Appl. Phys. Lett.*, **100**, 221111, 2012.

C A. I. Väkeväinen, R. J. Moerland, A.-P. Eskelinen, H. T. Rekola, G. Sharma, L. J. Lehtola, and P. Törmä, Nanoantenna structures for strong coupling studies of surface plasmon polaritons and quantum dots, *Proceedings of SPIE*, **8424**, 84240B, 2012.

D R. J. Moerland, G. Sharma, A. I. Väkeväinen, A.-P. Eskelinen, H. T. Rekola, and P. Törmä, From vacuum Rabi splitting towards stimulated emission with surface plasmon polaritons, *Proceedings of SPIE*, **8096**, 809606, 2011.

E R. J. Moerland, T. K. Hakala, A. I. Väkeväinen, A.-P. Eskelinen, G. Sharma, J. J. Toppari, A. Kuzyk, M. Pettersson, H. Kunttu, and P. Törmä, Vacuum Rabi splitting for surface plasmon polaritons and Rhodamine 6G molecules, *Proceedings of SPIE*, **8070**, 80700D, 2011.

1. Introduction

Nanoscience and nanotechnology involves the study of materials in the size scale of 1×10^{-9} m. The etymological derivation of the prefix nano can be traced back to Greek word nanos meaning a dwarf or "little old man". Although the word nanoscience can be considered to indicate into experimental and theoretical aspects, while the nanotechnology word would cover development and applications sides, the division is somewhat arbitrary and therefore the two words are quite often used interchangeable.

It is hard to date back when human beings have started to take advantage of nanoscale materials. It is known that Roman glass makers used nanosized material to stain glass. Evidence from this can be found from the British museum where an artifact called the Lycurgus cup is held, picturing King Lycurgus being dragged into underworld by Abrosia. The cup appears green when illuminated from outside, but turns into red if illuminated from inside, except for the king who appears purple. Nowadays it is known that the colour originates from metal nanoparticles (66.2 % silver, 31.2 % gold and 2.6 % copper) embedded into a glass matrix. Beautifully coloured glass can also be found from the windows of medieval churches, colours stemming again from light scattering from metal nanoparticles.

There appear several new interesting phenomena in the nanoscale that are not visible in bulk materials. In these size scales quantum mechanical and thermodynamic properties such as confinement of the electron movement and the Brownian motion become important. As an example of applications harnessing these new features are the carbon nanotubes discovered by S. Iijima in the 1991 in the NEC laboratory or the quantum dots stemming from the first quantum wells grown by research groups at Bell Laboratories and IBM. Nanotechnology has also made possible the miniaturization of transistors and the emergence of the integrated circuit technology. The development of imaging techniques for nanotechnology, such as the scanning probe and electron microscope technolo-

gies, should also not be forgotten.

This thesis focuses on methods developed for assembling and positioning materials in a controlled and programmable manner in the nanoscale. The traditional approach for processing materials and building devices in the nanoscale is the top-down approach, which can be considered as removing, subtracting or subdividing bulk material. In Chapters 3. and 4. an opposite approach, taking advantage of DNA nanotechnology, is used for the structure assembly. In Chapter 3. DNA structures are used for controlled assembly of single-walled carbon nanotubes and a geometry that could be used for a transistor is demonstrated. In Chapter 4. DNA structures are used for constructing nanosized bow-tie antennas that could be used as an optical sensor taking advantage of surface plasmon resonances provided by spherical silver nanoparticles. In Chapter 2. the DNA nanotechnology and basics of DNA structure formation are presented. Chapter 5. presents a method for controlling the DNA structures themselves, used for assembling the nanomaterials in Chapters 3. and 4., with external trigger signals

In addition to the DNA structure-based positioning of nanoparticles, another approach based on electromechanics is introduced named as dielectrophoresis. The theoretical principles for the method are presented in Chapter 6. There the method is used for demonstrating a new nanoscale printing technique - the field-induced nanoimprint lithography. Finally in Chapter 7. the dielectrophoresis is harnessed for assembling gold nanoparticles into one-dimensional geometries suitable for sensor applications.

2. DNA nanotechnology

Nanotechnology can be considered as manipulation of matter with at least one dimension on the size scale below 100 nm. DNA nanotechnology, on the other hand, is a sub-field of nanotechnology where the deoxyribonucleic acid is used as a construction material rather than as a carrier of genetic information – a task it has in living organisms in protein production together with the ribonucleic acid molecules. As a specific feature, the DNA nanotechnology rests heavily on the self-assembly of structures, which can be defined as spontaneous and reversible organization of structural units with non-covalent interactions. The DNA based assembly can also be characterized as a bottom-up approach the original system being a subsystem of a more complex emerging construction.

DNA is extremely interesting material for nanotechnology for numerous reasons. Firstly, it is a small molecule with a diameter of 2 nm combined with a short structural repetition of 3.4-3.6 nm (the helical pitch). Moreover, although single stranded DNA being flexible, double stranded DNA is a relatively stiff molecule with persistent length of about 50 nm. Nowadays, arbitrary sequence strands can readily be synthesized by automated solid supports. The nature offers also several enzymes for DNA manipulation. However, as perhaps the most crucial feature, DNA offers programmability and predictability in the self-assembly process through a simple set of base pairing rules.

In the following sections DNA is briefly introduced as a building material for applications in nanotechnology. First, important factors related to the DNA molecule itself, bearing self-assembly in mind, are presented before going into actual DNA constructions. In Publications I–III of this thesis, the so-called DNA origami method has been exploited for manipulation of materials in the nanoscale and therefore the emphasis is in the method in question.
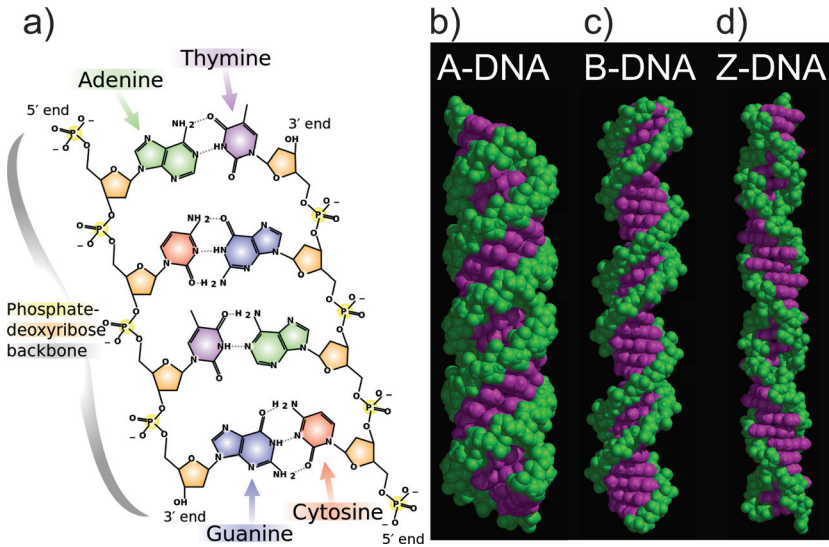
Figure 2.1. Deoxyribonucleic acid consists of two linear polymers running in opposite directions consisting of structural units called the nucleotides. The polymers are connected together with weak hydrogen bonds (a). The DNA can exist in many different conformations the three main families being A-DNA (b), the B-DNA (c) and the Z-DNA (d) [1].

2.1 The deoxyribonucleic acid

Deoxyribonucleic acid (DNA) contains the genetic information enabling organisms to develop, function and transfer genetic information to their offspring. The structure of the DNA is presented in the schematic Figure 2.1 (a). The DNA is built from two linear polymers, which themselves are made out of structure units named as nucleotides. These building blocks consist of a phosphate group (PO_4^-), a pentose sugar and a heterocyclic organic base. For the bases there are four possibilities, namely the purines adenine (A) and guanine (G), and the pyrimidines thymine (T) and cytosine (C). The nucleotides can bind from their sugar groups with the help of phosphodiester bonds to form the linear polymers called the single stranded DNA or in short ssDNA. The phosphate groups in the backbone of the DNA strand are negatively charged and therefore the DNA strand as a whole bears a negative charge. The strands end on the one side to a free phosphate group (the 5'-end), and on the other to a free hydroxyl group (the 3'-end). Therefore the strand has a running direction i.e. a polarity. The strands are classified according to the sequence of bases in the strand, which is listed starting from the 5' end progressing towards the 3'-end.

Two of the ssDNA strands can associate with the so called Watson-Crick-type base pairing to form a helical secondary structure – the DNA molecule (Figure 2.1 (a)). There the bases of adjacent strands bind together with weak

hydrogen bonds according to the Chargaff rule [2] which states that there are only two types of base pairs in DNA, namely the A-T and G-C pairs. The A-T bases bind with two hydrogen bonds with a total energy of hydrogen bonds E_{A-T} = 7.00 kcal/mol, and the G-C bases with three hydrogen bonds with a total energy of the hydrogen bonds E_{G-C} = 16.79 kcal/mol [3]. In addition to the base pairing, stacking interactions (π-stacking) take part in stabilizing the DNA-molecule structure. The total energies of stacking interactions between different type of base pairs range from 3.82 kcal/mol between A-T and T-A pairs to 14.59 kcal/mol between C-G and G-C pairs [4]. The other base pair options take stacking energy values between the mentioned ones. Thus, the base-pairing and base stacking interactions are of the same order of magnitude in strength. In addition to these two mechanisms, long-range intra- and inter-backbone forces, stemming from charged phosphate groups, influence in the stabilization of the DNA-molecule.

The stabilizing interactions are still relative weak compared, for example, to the covalent bonds (between two carbon atoms E_{C-C} = 83.1 kcal/mol [5]) and therefore the DNA strands can easily be separated from each other with the help of a strong base or by heating. The process is called denaturation. On the other hand, removal of the denaturant agent leads into double strand formation – process named as renaturation. Thus the process is reversible, a feature typical for the self-assembly.

The DNA-molecule can take several different helical conformations three main families being A-DNA, B-DNA and Z-DNA. Transition from a conformation to another can take place upon a change in environmental parameters, such as the salt concentration. From these families the B-DNA is the most stable conformation under physiological conditions. There the DNA-molecule has a right handed helix structure, where the adjacent bases are separated by 3.4 Å and rotated 36° with respect to one another. There are in total 10.5 bases in one complete turn corresponding to a length 34 Å. In addition to the mentioned DNA families, there are a variety of exotic forms such as the four stranded G-quadruplex structure [6].

2.2 Self-Assembled DNA nanostructures

The field of DNA nanotechnology can be considered to be founded by N. C. Seeman in the 80's. The DNA structures were realized in the those early days with short double stranded DNA material (oligonucleotides) having single stranded overhang extensions operating as sticky ends for attaching the DNA molecule
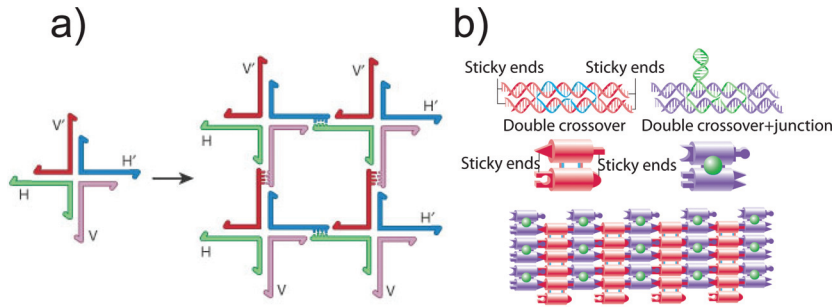
Figure 2.2. A branched structure is needed for assembling two-dimensional arrays from DNA. For the purpose, a Holliday junction with ssDNA overhangs was prepared (a). This structure, however, turned out to be too flexible and therefore a demand for a more rigid structure arose. The DX-tile blocks (b) provided the needed rigidity for assembling two-and three-dimensional structures. Figure (a) reproduced with permission from Ref. [8] and (b) from Ref. [9] ©Alice Y. Chen, 2004 for *Scientific American*.

into a complementary sticky end in a second oligonucleotide [7]. These efforts did not however lead into intended complex two dimensional shapes due to the fact that dsDNA is a linear structure. It was realised instead that a branched motif was required. This kind of motif was provided by Holliday junctions – branched structures consisting of four ssDNA arms (Figure 2.2 (a)) naturally occurring in living systems. In nature these structures form during meiosis from two dsDNA strands which dissociate first into four ssDNA strands and finally form the four arm structure illustrated in the figure 2.2 a). These structures equipped with sticky ends could in principle be used for assembling two dimensional arrays. Although Seeman and co-workers were able to prepare such branched junctions [10], it came e-vident that stiffer structures were needed in order to achieve two-dimensional constructions. The solution was provided by a DNA motif called the DX-tile (double cross over tile). The name refers to the two Holliday junction interconnections between two adjacent dsDNA regions. Figure 2.2 (a) presents the structure and illustrates the principle for preparation of two dimensional DX-tile DNA arrays.

Since the early days, several different two- and three-dimensional DNA structures have been demonstrated including a cube [11], an octahedron [12], a tetrahedra [13] as well as larger 2-and 3-D complexes based on DX-tiles [14, 15] and TX-tiles (triple cross over) [16]. A more recent advance in the methods of using DNA oligonucleotides as building blocks was provided by Ke et al. [17]. There the authors took advantage of 32-nucleatide long DNA bricks as modular components analogous to Lego building blocks (Figure 2.3). With the method the authors were able to produce a large number of arbitrary shaped complex 3-D structures.
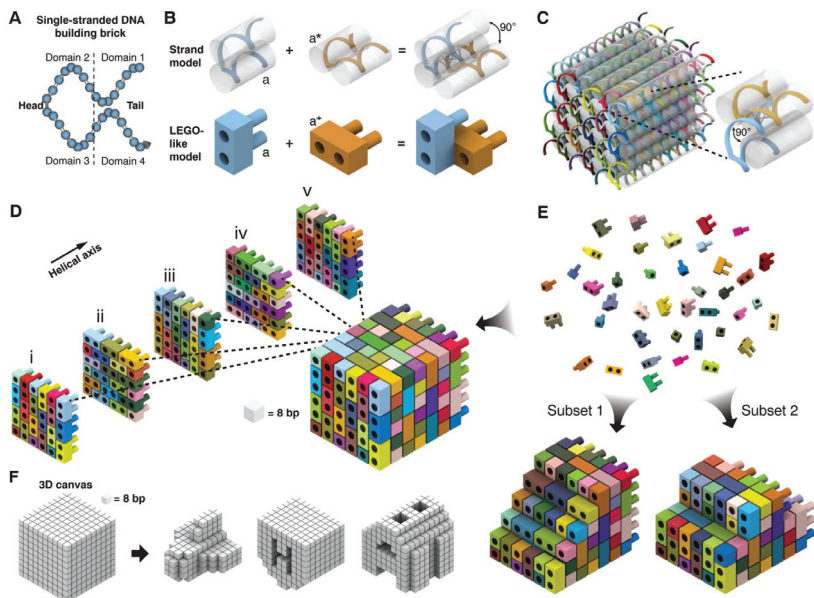
Figure 2.3. In Figure, short synthetic DNA molecules were used for assembling complex arbitrary shaped three-dimensional constructs. The method reminds closely of Lego brick assembly. The approach is based on 32 nt long ssDNA strands named as bricks consisting of four domains. These domains are grouped into a head and a tail (A). A tail group of one brick with sequence s can pair with a head group of another brick having sequence s* in a stereospecific manner as illustrated in (B). Figure (C) illustrates a 6 helix X 6 helix X 48 bp cubic structure assembled from the basic building units. Its Lego analogue is illustrated in (D). One can vary the structure by using only a subset of bricks used for building the complete cubic system (E). Actually, quite complex shapes can be constructed by leaving certain bricks away from a cubic structure with the help of computer aided design (F). Reproduced with permission from Ref. [17].

Figure 2.4. DNA origamis are arbitrary two-and three-dimensional shapes constructed by fold-
ing a long scaffold ssDNA strand with the help of a large set of short ssDNA strands
named staples. With a certain design of staple strand positions in the structure,
stress and strain can be induced in the structures enabling preparation of curved
shapes. Reproduced with permission from Ref. [19].

2.2.1 DNA origami

DNA origami [18] are arbitrarily shaped two-and three-dimensional self-assemb-
led structures made by folding a long single stranded DNA (ssDNA) scaffold
with the help of a large set of synthetic short ssDNA strands named staples.
Figure 2.4 illustrates the diversity of objects possible to prepare with the method.
The scaffold can be either linear or circular. In the articles of this thesis circular
natively single-stranded M13-phage viral plasmid (7250 bp long, isolated from
M13mp18) was used as the scaffold material.

As was mentioned in Section 2.1, ssDNA strands can be opened and asso-
ciated again with the help of heating. The most common approach for DNA
origami preparation is the thermal annealing of the staples and the scaffolds
in a buffered solution. The DNA material is heated above its melting temper-
ature followed by slow cooling of the substances to room temperature. During
the cooling step, the staples search their positions in the scaffold and fold it into
the desired shape. The planar 2-D structures can be formed in a couple of hours
with nearly 100 % yield [18], while the multi-layered structures might take up
to a week to form with relative low yields (5-20 %) [20]. In addition to the
thermal annealing, formation of the origami structures in a denaturing buffer
(formamide) has been demonstrated. There the DNA origamis formed when the
concentration of formamide was successively decreased by dialysis [21].

The structure and the formation principle of the DNA origami is presented in

Figure 2.5. Figure is a schematic presentation, and in reality, the scaffolds and the staple strands are floating in the reaction solution in a random conformation prior to the origami formation. As the first designing step, the scaffold is put to run through the whole structure in a raster pattern (Figure 2.5 (c)). This pattern determines the sequence of the staples strands needed for keeping the structure together. The staples accomplish their task by forming regions of B-DNA with the scaffold (Figure 2.5) (a). This DNA conformation means: a complete 360° turn of the DNA helix is 10.5 bases in length [23]. The staples join neighbouring dsDNA strands by forming immobilized Holliday junctions [24] – a junction composed of four ssDNA strands. These are formed from antiparallel crossovers of staples (or the scaffold) (Figure 2.5) (b), (d). The frequency of these crossovers has a significant impact in the outcome of the final origami structure. First, it has influence on the interhelix gap which is the separation between two adjacent dsDNA regions [18]. In the case of structures used in this thesis, the crossovers appeared with separation of 16 bases which means 1.5 turns of DNA [18]. This led into interhelix gap of 1 nm. In multilayered structures a more frequent division is used, and for example the density of one turn every 7 bp or 8 bp leads into interhelix gap smaller than 0.5 nm [20, 25]. Moreover, with a certain choice of crossovers, stress and strain can be induced into the origami structure enabling formation of curved structures [26] as illustrated in Figure 2.4. There are dedicated software for designing [27, 28] the DNA origami structures as well as for their analysis [29].

The scaffold does not necessarily need to be completely paired with the staples, but instead regions of ssDNA can be left behind. As was observed Section 2.1, the stacking interaction taking part in stabilizing the dsDNA structure is of the same order of magnitude in strength as the hydrogen bonding between the base pairs. Therefore blunt ends of dsDNA in the edges of DNA origamis can lead into uncontrolled aggregation of the structures. Due to this, quite often staples from origami edges are omitted. Sometimes, however, these stacking interactions can be favourable as was demonstrated by Woo et al. by programmed assembly of DNA origamis into larger entities with the help of the DNA blunt ends [30].

2.2.2 DNA Origami as a tool for nanoscale positioning of materials

The DNA origami structure has one important feature concerning the set of staple strands: all of them are unique in sequence. As a consequence, each strand has a predefined position in the DNA origami structure. Moreover, the staples can readily be chemically modified for example with biotin, amines, thiols and
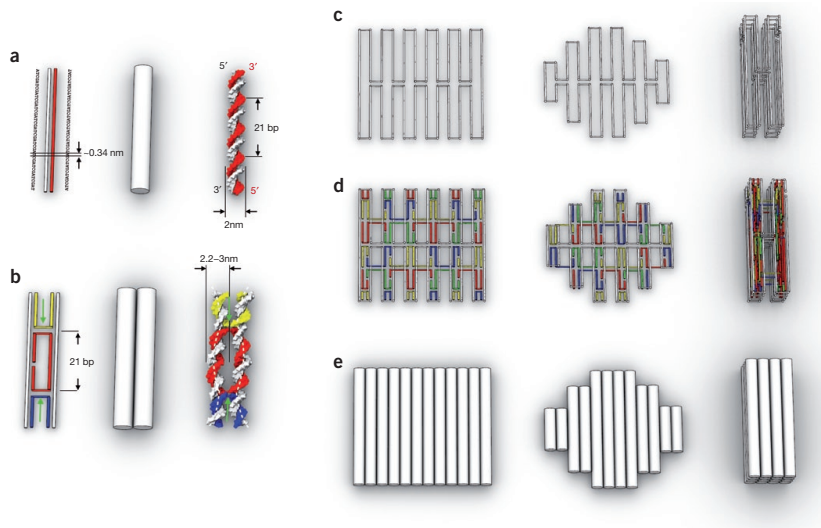
Figure 2.5. The DNA origami is formed from two sets of ssDNA material, namely the staples and the scaffold. The staples associate with the scaffold to form B-DNA (a). The positions, where staple strands run from one dsDNA helix to an adjacent one, are named as cross-overs (b). Through the hybridization of the two ssDNA materials combined with the formation of the cross-overs, the scaffold is forced to follow a raster pattern (c,d). For design purposes the structures can be visualized as solid cylinders (e). The dimensions in the structures are presented in (a) and (b). Reproduced with permission from Ref. [22].
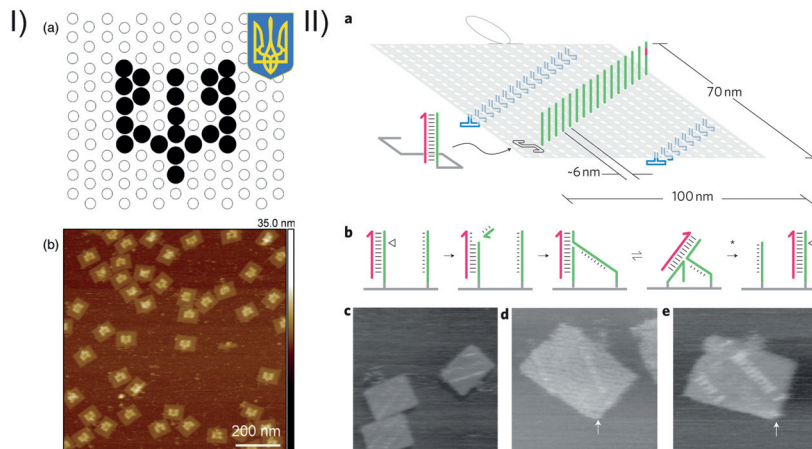
Figure 2.6. The DNA origami substrate can be used as a nanosized "breadboard" where the staple strands can be thought as binding pixels (I, a). In (I) a complicated pattern of streptavidin protein has been attached on the origamis into biotin-modified staple strands. In (I, b), there are atomic force microscope images of the assembled structures. In addition to proteins, a variety of other nanomaterials can be assembled with the DNA origami method. In (II,a), tracks for a DNA molecular walker have been attached. Figure (I,b) presents how the DNA molecular walker proceeds along the tracks with the help of a nicking enzyme. An AFM image of the system is presented in (c). The starting point of the molecular walker is an empty site in the DNA origami structure (d), where the walker hybridized with the gray ssDNA part (e). Figure (I) reproduced with permission from Ref. [31] and (II) from Ref. [32].
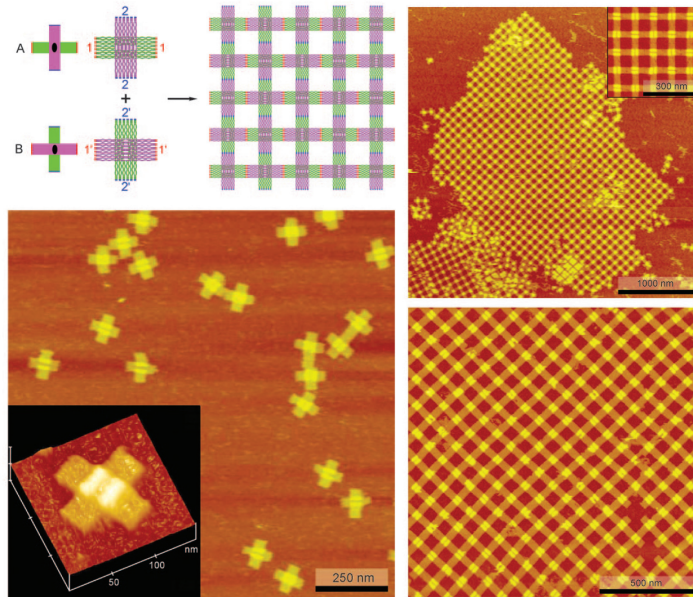
Figure 2.7. Large networks can be built with individual DNA origamis as building blocks. In Figure, cross-shaped DNA origami tiles have been assembled, with the help of ss-DNA overhangs sticking from the edges of the origamis, into micron-sized assemblies. The images about the individual tiles and networks of tiles have been obtained with AFM-imaging. Reproduced with permission from Ref. [48].

azides. This opens up a unique possibility to programmable address materials into arbitrary patterns on the origami substrate with resolution limited only by the size of the staple strands. In other words, the DNA origami can be used as a nanosized "breadboard". The concept is illustrated in Figure 2.6 (I). There biotin modified staple strands operate as pixels for generating a complex pattern of streptavidin protein on the DNA origami substrate. Similar biotin pixels were used also in Publication I of this thesis to produce single-walled carbon nanotube assemblies on origami substrates. There are several demonstrations on assembling different kinds of nanomaterials on the DNA origami substrate, such as proteins [31], carbon nanotubes [33–35], virus capsids [36] and metal nanoparticles [37–45]. Even tracks for DNA molecular walkers have been deposited on the DNA origami substrate [32] (Figure 2.6 (II)). The DNA mediated assembly of metal nanoparticles is dealt in more detail in Chapter 4, while the assembly of single-walled carbon nanotubes on different configurations is presented in the following chapter.

The size of the planar DNA origamis is roughly 100 nm in diameter i.e. the structures are relatively small restricting the overall size of the material patterns possible to assemble on the substrate. Therefore efforts have been taken for assembling larger structures of individual DNA origami structures as basic

building blocks [30, 46–48]. These structures can be achieved by using ssDNA overhangs sticking from the edges of the DNA origami structures complementary to overhangs in another origami structure. In Figure 2.7, a large network has been build from individual DNA origami tiles with the help of ssDNA sticky ends. These kinds of large origami networks could for example be used for manufacturing logic circuits from carbon nanotubes [49].

3. Assembly of single-walled carbon nanotubes with the DNA origami method

Single-walled carbon nanotubes (SWCNTs) are tubular structures with extraordinary electrical and optical properties stemming from the confinement of the electron wave-function in two dimensions. Moreover, SWCNTs have been found to be a very tough material. Due to their versatile properties, the SWCNTs have found applications ranging from memory [50,51] elements to material reinforcing fillers (Hyptonite). However, there are still several challenges hindering the use of the SWCNTs in commercial applications. In addition to being able to produce high quality material in mass scale, one should have control over the electrical properties of the SWCNTs meaning ability to sort the SWCNT material according to its chirality [52]. Moreover, the alignment of the SWCNTs on substrates for electrical contacting is still an open issue [53].

In Publication I of this thesis a solution for the SWCNT alignment issue, based on the DNA origami method, was presented. The method was demonstrated with three different SWCNT configurations. In the first one, a single SWCNT was bound and aligned on the origami structure. This configuration, combined with some other electrically, optically or biologically active nanoparticles, could be used for sensing, as information storage and for energy or information conversion. In the two other ones, two SWCNTs were bound in the same origami, aligned to form a cross junction – a geometry suitable for transistor operation. Although the method was demonstrated for SWCNTs, the approach can be adapted also for other nanotubes.

In the following sections the self-assembly and alignment of SWCNTs through the DNA origami method is discussed. The SWCNTs were attached to the DNA origami substrates with the help of streptavidin-biotin interaction. For this, the SWCNTs were functionalized with biotinylated ssDNA which was also used for dispersing the material in a water based solution. Therefore, as a crucial part of the method, the ssDNA functionalization of SWCNTs is discussed first in detail. For a general introduction to the preparation, properties and applications

of carbon nanotubes, see a recent review paper [54]. In addition, the book by Jorio et al. provides a comprehensive introduction to the properties of CNTs [52].

3.1 Functionalization of single-walled carbon nanotubes with deoxyribonucleic acid

Due to the tubular nature of the SWCNTs, they tend to form bundles that are difficult to separate and dissolve into both organic [55] and inorganic solvents, and yet there would be a demand for efficient separation and assembly methods [56]. The task can be carried out with the help of strong oxidizing acids which generate shorter and partially modified CNTs [57, 58]. Acids have also an important role in purifying the CNTs from catalyst residues. The downside of the approach is its tendency to damage the processed SWCNTs. Also super acids [59], charged nanoparticles [60], proteins [61] or polymers [62–64] can be used for dissolving the CNT material. In addition aqueous solutions of CNTs can be produced with ionic detergents such as sodium dodecyl sulfate [65], sodium cholate [66] or sodium dodecylbenzene sulfonate [63]. The problem with ionic detergents is the need to use them in high concentrations. Moreover, removal of excess unbound surfactants can cause rebundling of the CNTs.

Another approach for separating and dispersing SWCNT bundles into aqueous solutions is to use single stranded DNA. The advantage of the method lies in its nondestructive nature. Moreover, there exist well developed chemistries for DNA strand functionalization with various kinds of functional groups, biotins and thiols as examples. For this fascinating combination of two extraordinary materials, several practical applications have been proposed such as chemical sensors [67], DNA detectors [68, 69], field effect transistors [70] and using the approach for cancer cell destruction [71].

3.1.1 The functionalization mechanism

According to thermodynamic integration studies on the binding of individual DNA bases to SWCNTs, the bases stack on the CNT surface with van der Waals forces [72]. In the case of aromatic molecules, this interaction is also known as π-stacking. The distance between the base and the CNT surface appears to be roughly 0.34 nm which is the same as the distance between two sheets of planes in graphene [73]. The DNA bases bind strongly on the CNT surface and in the case of all the DNA bases the base-CNT binding free energy is in the
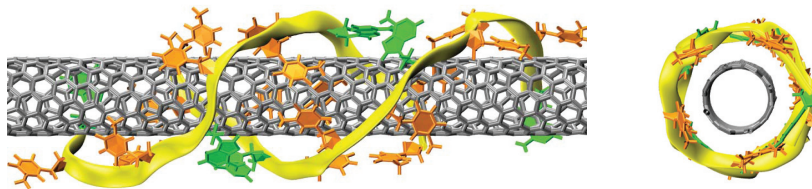
Figure 3.1. Single stranded DNA is efficient in opening SWCNT bundles and dispering them into aqueous solutions. The DNA bases stack on the CNT surface, while the sugar and phosphate groups are exposed to the solvent. As a consequence, the ssDNA forms barrel around the CNT as illustrated in Figure. Reproduced with permission from Ref. [76].

order of 10 kcal/mol, which is $17 \times k_B T$ [72]. Experimental results complement the observations, and solutions prepared with ssDNA/SWCNTs are stable for months at room temperature. Although all the bases have been found to bind into CNT surfaces, the purines (G, A) show increased affinity compared to the pyrimidines (T, C) [72]. Intuitively this is quite obvious to see – the purines are made out of two aromatic rings instead on one in the pyrimidines. The variation of the binding strength between the bases appears to follow a trend G<A<T<C, however different observations have also been reported [74].

As the bases stack with the van der Waals forces on the SWCNT surface, they go through a major conformational change. The bases rotate 90 degrees from the π-stacked conformation [73] encountered in native DNA and the phosphates and sugars, forming the DNA helix backbone, get more exposed to the solvent. This exposure of the sugars and phosphates is supposed to have a significant role in dispersing the SWCNTs [75]. The ssDNA functionalization of SWCNTs is illustrated in Figure 3.1. There the ssDNA has formed a single barrel like layer around the CNT. However, ssDNA is a very flexible polymer and therefore several different configurations, like right-handed helical, left-handed helical and straight wrapping is possible (Figure 3.2) [73, 77]. The salt concentration of the aqueous solution has also a major impact on the DNA configuration. Moreover ssDNA length-dependent binding has been reported and even the ability to sort CNTs to metallic and semiconducting species according to ssDNA length has been reported [75].

Interestingly, theoretical and experimental investigations have demonstrated that basically all sorts of ssDNA sequences should bind and solvate SWC-NTs [72, 73]. In addition, there should not be any preference in certain base sequences binding into certain chirality CNTs [72]. Still X. Tu et al. [76] reported on structure-specific recognition of CNTs by different sequences of ss-DNA. From their test set of 350 different ssDNA sequences, they were able to find more than 20 sequences that were able to purify certain chirality CNTs
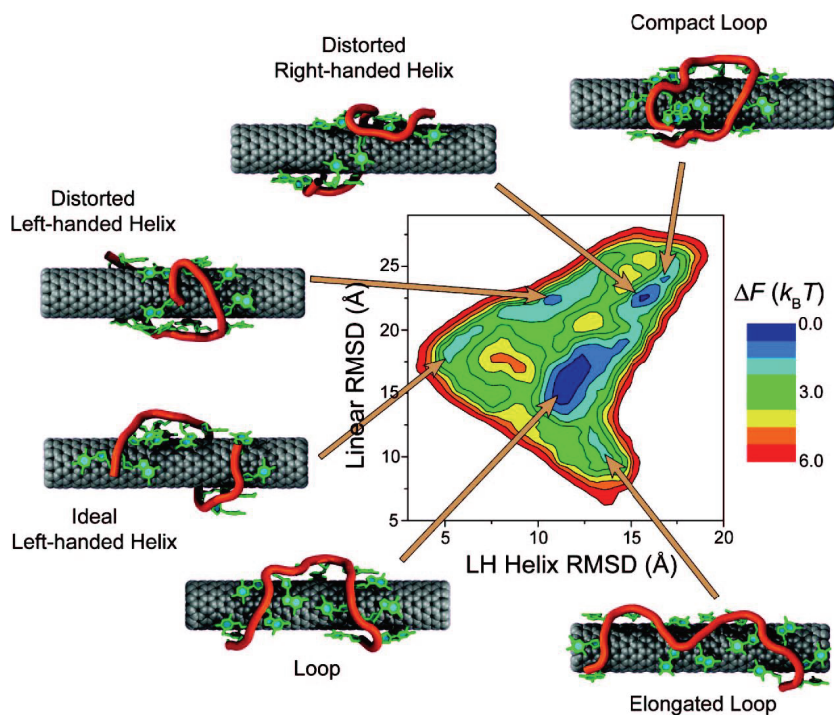
Figure 3.2. Free energy landscape for $(GT)_7$ ssDNA functionalized SWCNTs. The axes in the plot present the minimum root-mean-square deviations of the $(GT)_7$ phosphorous atoms from an ideal left-handed (x-axis) and linear (y-axis) conformations. According to simulation studies, there are several energy minima corresponding to different kinds of ssDNA wrapping on the CNT surface the loop configuration being a global minimum. Reproduced with permission from Ref. [77].

with the help of ion exchange (IEX) chromatography [76]. However, instead of chirality dependence in binding, the mechanism for the finding could lie in the formation of barrel like organized structure (as in Figure 3.1) with certain CNT chiralities with a given ssDNA sequence which then minimizes its van der Waals and hydrophobic interactions with the IEX-resin [72, 76]. Despite whatever the mechanism would be, the finding is extremely valuable and provides a new approach for SWCNTs separation, which is based on the ssDNA mediated sorting according to SWCNT chirality. Typically people have settled for separating the raw CNT material into metallic and semiconducting species, which is a significantly weaker conditions compared to the purification of CNTs into species of different chirality.

3.1.2   Experimental methods

The carbon nanotubes for the assembly of SWCNTs on the DNA origami substrates were prepared in the Aalto Univiresity by prof. Esko Kauppinen's group [78]. We tested also commercial semiconducting SWCNTs (Nanocyl Inc.), but for some reason the assembly process did not succeed with them. We were able to disperse the material into water, but we could not attach the ssDNA functionalized CNTs into the DNA origami substrates. We postulate that this could be a consequence of more residue-free material provided by Kauppinen's group combined with low bundling level of their SWCNTs. The SWCNTs were prepared with an aerosol (catalysis floating) CVD (chemical vapor deposition) reactor by ferrocene vapor decomposition in a carbon monoxide atmosphere. The length of the CNTs can be controlled with reaction conditions and in our experiments the average lenght of the CNTs was about 290 nm.

The properties of the SWCNTs can be probed optically. The optical properties of the SWCNTs stem from their 1-dimensional nature which leads into Van Hove singularities in their electronic density of states [79]. Each different chirality SWCNT has a different set of van Hove singularities and hence a different optical response. A typical approach for optical investigations of CNTs is the resonance Raman scattering method which involves inelastic scattering of light from the CNTs. There are Raman spectra, obtained with two different exciting lasers (633 nm and 488 nm), from a typical SWCNT raw material used in our experiments in Figure 3.3.

In the spectrum, typical features for the SWCNTs can be found. Firstly, radial breathing mode (RBM), the collective oscillation of the carbon atoms in the radial direction, is clearly visible in the spectrum. This is a unique property of the CNTs and can be used for determining the diameter of the SWCNTs in
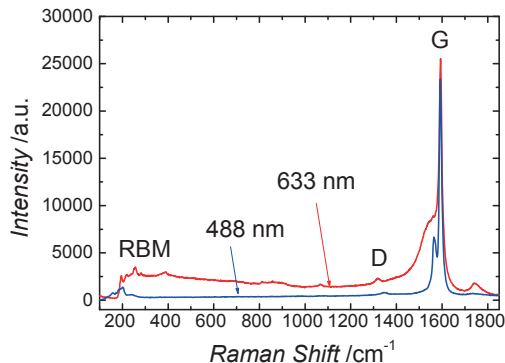
Figure 3.3. Raman spectrum from as-grown SWCNTs excited with 488nm and 633 nm lasers. Sharp G band peak and low D/G ratio indicate high purity SWCNT consisting mostly of semiconducting spieces. The radial breathing mode (RBM), the collective motion of the carbon atoms in the radial direction, is a fingerprint of the carbon nanotubes. Reproduced with permission from Publication I of this thesis.

the sample. Sharp features, instead of a Bright-Wigner-Fano type of profile, at roughly 1600 cm^{-1} prove our SWCNTs to be mostly semiconducting [79]. The intensity ratios of the G-band and defect related D-band is small ($I_D/I_G =$ 0.09 for the red laser and $I_D/I_G = 0.04$ for the blue one) indicating high-quality SWCNTs.

Despite the reports on the more efficient binding of purines to SWCNT surfaces and results obtained with repeats of sequence $(GT)_n$ [80], we decided to use poly T (T_{40}) strands as our ssDNA material. The same sequence was used also by Maune et al. in their DNA origami mediated SWCNT assembly experiments [33]. In our case the ssDNA strands had biotin modifications in the 3' end (or at the half way of the ssDNA strand). The SWCNTs (1 mg) were dispersed into milliQ water (0.8 ml), having 320 nM ssDNA and 0.1 M NaCl, with tip sonication (7 W, 90 min) in a water bath at about 15 °C. The sonication was conducted in pulsed mode with 2s pulse/pause length. In order to separate the SWCNTs bundles into individual ones, due to the rapid nature (in the scale of tens of nanoseconds) [77] of the ssDNA binding on the CNT surface, one needed to get the CNTs separated from each other only for a short period of time. Therefore minimal sonication power was needed. Moreover, small powers are desired in order not induce damage in the SWCNTs. The water bath was used to avoid elevated temperatures.

After sonication, excess SWCNTs that had not been dispersed by the ssDNA strands, were removed by centrifugation with 16000 g for 90 min at 4 °C. The centrifugation process pushes the undispersed SWCNT material to the bottom of the container and therefore the supernant was collected. This purification
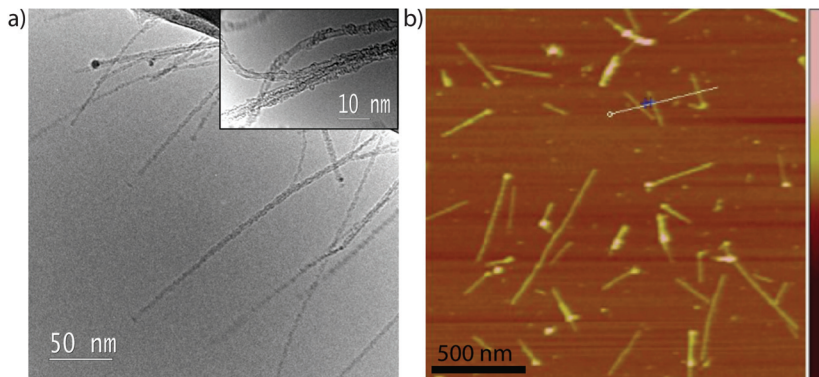
Figure 3.4. A transmission electron microscope image (a) and an atomic force microscope image (b) about ssDNA wrapped SWCNTs. The height of the CNTs in Figure (b) under the line is about 1.22 nm. Reproduced with permission from Publication I of this thesis.

step did not yet remove excess ssDNA strands and therefore the collected supernants were spin filtered three times. During the spin filtering, liquid containing excess ssDNA gets squeezed through the filter leaving functionalized SWCNTs behind. Every time the liquid that had gone through the filter was replaced with milliQ water having 0.1 mM NaCl. There is a transmission electron microscope (TEM) and an atomic force microscope (AFM) image about ssDNA functionalized SWCNTs in Figure 3.4.

3.2 Assembling single-walled carbon nanotubes with the DNA origami method

The assembly of the ssDNA functionalized SWCNTs on the DNA origami substrates is illustrated in Figure 3.5. In the figure, some of the staple strands in the origami structure have been replaced with biotinylated ones (Figure 3.5 (a)). In this particular case, there are in total 10 biotinylated staples forming two biotin lines on the same side of the origami structure. These biotins can bind Streptavidin, and by this way form two binding site rows for DNA/biotin functionalized CNTs (Figure 3.5 (c)). Each of the rows should bind a single SWCNT in a manner that they would align themselves according to the STV binding site rows (Figure 3.5 (d)). In this particular case, the SWCNTs should form a crossed junction on the one side of the origami structure.

The DNA origami substrate used for assembling SWCNTs comprised of 192 staple strands in total. Depending on the binding site configuration either 5, 10 or 21 staples had been replaced with biotinylated versions. Moreover, the staple strands from the edges were again left away in order to avoid uncontrolled
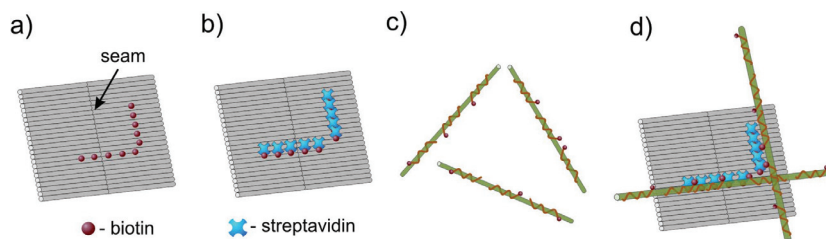
Figure 3.5. Schematic diagram on assembling single-walled carbon nanotubes on the DNA origami substrates. Some of the staple strands in the origami structures have been replaced with biotinylated ones (a). These operate as binding sites for the streptavidin proteins (b), which then form binding site rows for the SWCNTs. The carbon nanotubes, functionalized with the biotinylated ssDNA c), align themselves according to the STV binding rows (d. Reproduced with permission from Publication I of this thesis.

stacking of the DNA origami structures. The DNA origamis were formed by combining the M13mp18 scaffold with the staple strands in 50 μl reaction volume in 1 x TAE magnesium acetate buffer (40 mM TRIS, 19 mM acetic acid, 1 mM EDTA, 12.5 mM magnesium acetate). There the staples were used in 10 fold excess each compared to the scaffold strands.

The attachment of the SWCNTs into the DNA origami substrates was done in solutions with low ionic strength. Therefore the origami structures were strengthened with a ligation procedure [81]. There T4 polynucleotide kinase was used for incorporating a phosphate group in the 5' end of the staple strands. The enzyme operates best at 37 °C and therefore the DNA materials were incubated 37 min at that temperature. The incubation was followed by thermal anneal from 90 °C to 20 °C with 0.1 °C/min steps. The ligation process was completed after anneal with T4 DNA ligase, which catalyses the formation of a phosphodiester bond between juxtaposed 5' phosphate and 3' hydroxyl termini in dublex DNA. The ligation step was done overnight at room temperature. After the DNA origami fabrication process one ends up with 50 μl of roughly 1 nM DNA origami solution if assuming 100 % yield during the manufacturing process.

During the formation of the DNA origami substrates, staple strands were used in large excess compared to the scaffold strands to ensure proper formation of the structures. There especially the biotinylated staple strands, if not removed from the reaction volume, would interfere the SWCNT assembly by blocking binding sites from the origamis. Therefore excess staples were removed by spin filter columns having 100 kDa cut-off weight. The spin filtering step was repeated in total three times. Each time, the solution that had gone through the filter, was replaced with 1 x HEPES NaOH buffer solution (6.5 mM
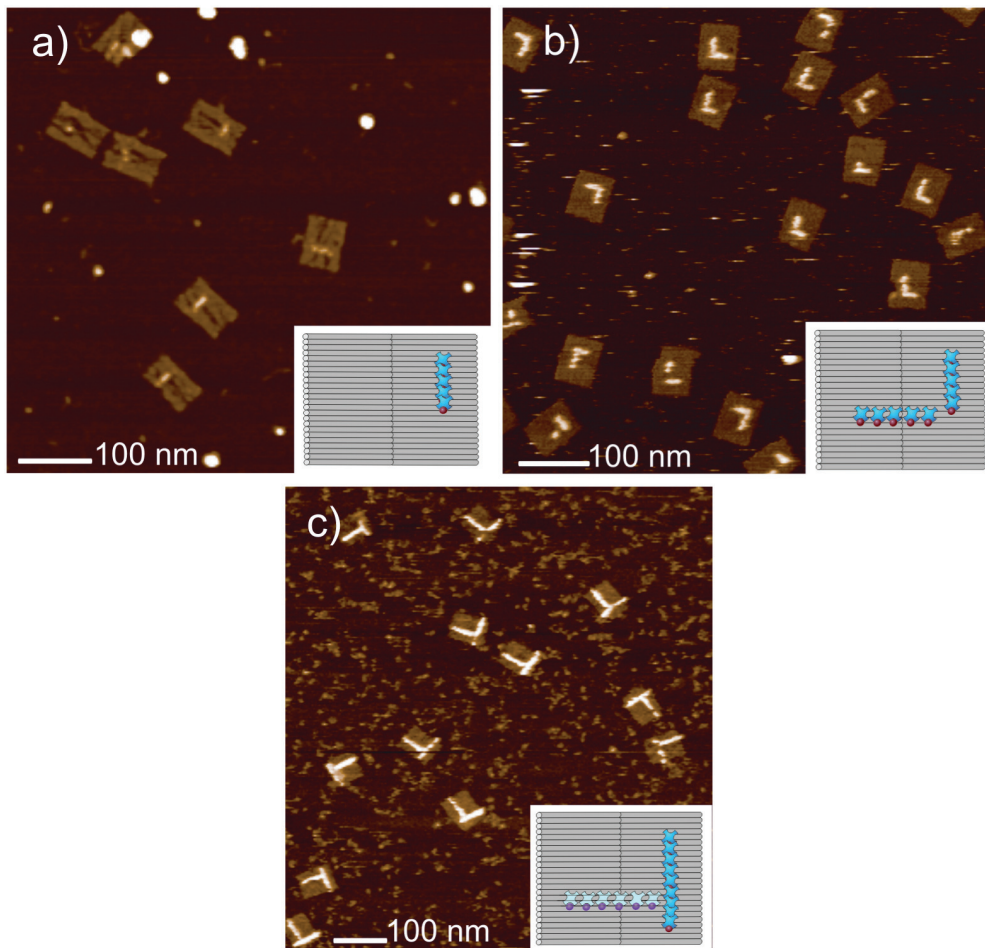
Figure 3.6. Atomic force microscope images of DNA origami susbtrates with a) 5, b) 10 and c) 21 STV binding sites for CNTs. The designed configuration is represented in the insets. Adapted with permission from Publication I of this thesis.

HEPES, 2.0 mM NaOH). After the last filtration step, the solution was brought to 100 μl volume with 1 x HEPES NaOH resulting in ~1 nM DNA origami solution. The binding sites for SWCNTs were formed by adding STV (recombinant streptavidin from *Streptomyses avidinii*) in 5-10 times excess compared to the DNA origamis. The solution was incubated overnight at 4 °C before removing unbound STV by spin filtering.

The AFM images in Figure 3.6 present the three different binding site configurations used in the experiments. In Figure 3.6 (a), there are five streptavidin pixels forming a single line on the origamis for hosting a single SWCNT. The single SWCNT binding scheme is already by itself an extremely important case. As was mentioned in the beginning of this chapter, in order to fabricate SWCNT transistors efficiently with UV or electron beam lithography, one has to have

control over the orientation of the SWCNTs on substrate surfaces for electric contact fabrication. Now that there are methods for positioning and aligning DNA origamis on semiconductor substrates [40, 82], the DNA origami method for assebling SWCNTs provides the needed controllability. Therefore the single SWCNT/origami could readily be used, after fabrication of electrical contacts to the SWCNT, as a transistor for example in a back gate configuration.

In addition to the crucial SWCNT alignment issue, the DNA origami substrate offers a unique possibility to address other types of electrically, optically, chemically or biologically active nanoparticles (for example proteins, quantum dots, metal nanoparticles, enzymes, various small molecules) to the template in addition to the SWCNT. Therefore the system can be used for example for sensing, as information storage and for energy and signal conversion. The CNTs are known to be efficient sensors, with, for example electrical [83] or optical [84] response. It has also been shown that CNTs can detect charges of few electrons up to 100 nm distances from the CNT [85]. Therefore the system could be used for detecting chemical/biological reactions, which include change in the electrical charge of the object. If the nanoparticle is optically active, for example a metal nanoparticle, one could use it to modulate the electrical conduction of the SWCNT i.e. the system could operate as an optical modulator. In all of these applications, the DNA origami substrate offers the possibility to control the interparticle distances in nanometer accuracy, feature that is important for example for nanoparticles where coupling of dipoles is desired. It is noteworthy that obtaining similar control and versatility over the interparticle separations with conventional top down methods is either extremely difficult or impossible.

In the other two configurations (Figure 3.6 (b), (c)), the DNA origamis have binding sites for two SWCNTs. The case (Figure 3.6 (b)) was introduced in the schematic Figure 3.5. The (Figure 3.6 (c)) differs from this by having 21 STV binding sites instead of 10. Moreover, the two STV lines are located on different sides of the DNA origami structure. Therefore, in this configuration, the two bound SWCNTs will be on the different sides of the DNA substrate. As one can observe from the AFM images, the STV binding site rows form on the DNA templates with excellent fidelity.

Whether having the SWCNTs on the same or on the opposite sides of the DNA origami substrate, depend on the desired application. It has been observed that substrates can cause deforming forces on crossed SWCNT junctions by imposing attractive forces on the SWCNTs [86]. According to *ab initio* pseudopotential density functional calculations SWCNTs forming a crossed structure on a substrate can come as close as 0.25 nm from each others as a

consequence of attractive forces between SWCNTs and the substrate [87]. This is significantly closer than the van der Waals separation (0.34 nm) and leads to a sizable intertube conductance. Depending on the SWCNT types forming the junction, conductance of 2 to 6 % of a quantum unit of conductance $G_0 = e^2/h$ for a metallic-metallic SWCNT junction has been reported. For a semiconductor-metallic SWCNT pair Schottky diode type of operation was reported for the junction with a Schottky barried of 200-300 meV [87].

In the case of having the SWCNTs on the same side of the DNA origami substrate, there the ssDNA wrapped around the SWCNTs will increase the separation between the SWCNTs and hence lower the intertube conductance. The distance between the SWCNT surface and the DNA bases is about 0.34 nm [73]. On the other hand, if the SWCNTs are on different sides of the DNA origami substrate, the separation between the SWCNTs gets increased by the thickness of the DNA origami substrate leading into better electrical isolation. The calculations revealed that with zero deforming force the junction conductance is practically negligible [87]. Hence, when good isolation is needed the SWCNTs should be attached on opposite sides of the DNA origami substrate and vice versa.

The SWCNTs were assembled on the DNA origami substrates by adding 10 μl of SWCNT solution in MilliQ H_2O having 0.1 mM NaCl into 15 μl of DNA origami solution. Incubation time was varied from 1 to 7 days in order to investigate the effect of time on the yield in structure formation. The incubation was carried out in 4 ºC.

3.2.1 Results

The results from the assembly experiments are presented in Figure 3.7, and analyses concerning the structure formation yields are presented in the table 3.1. In Figures 3.7 (b) and (c), there are results from assembling single SWC-NTs with the five STV pixel configuration. According to the table 3.1, the best results were obtained with 4 days incubation. There as high as 56 % binding efficiency was achieved and from these 48 % were aligned well according to the STV pixel line. As the incubation time was increased from 4 to 7 days, no increase in binding efficiency was observed. As can be observed from Figure 3.7 (c), in addition to having one carbon nanotube bound to individual DNA origami substrate, in some cases a single SWCNT hosted several origamis.

In the case of two SWCNTs per DNA origami best yields were obtained with a 3 day incubation with the configuration of having the SWCNTs on the same side of the origami i.e. the 10 pixel case (AFM images, Figure 3.7 (d), (e) and
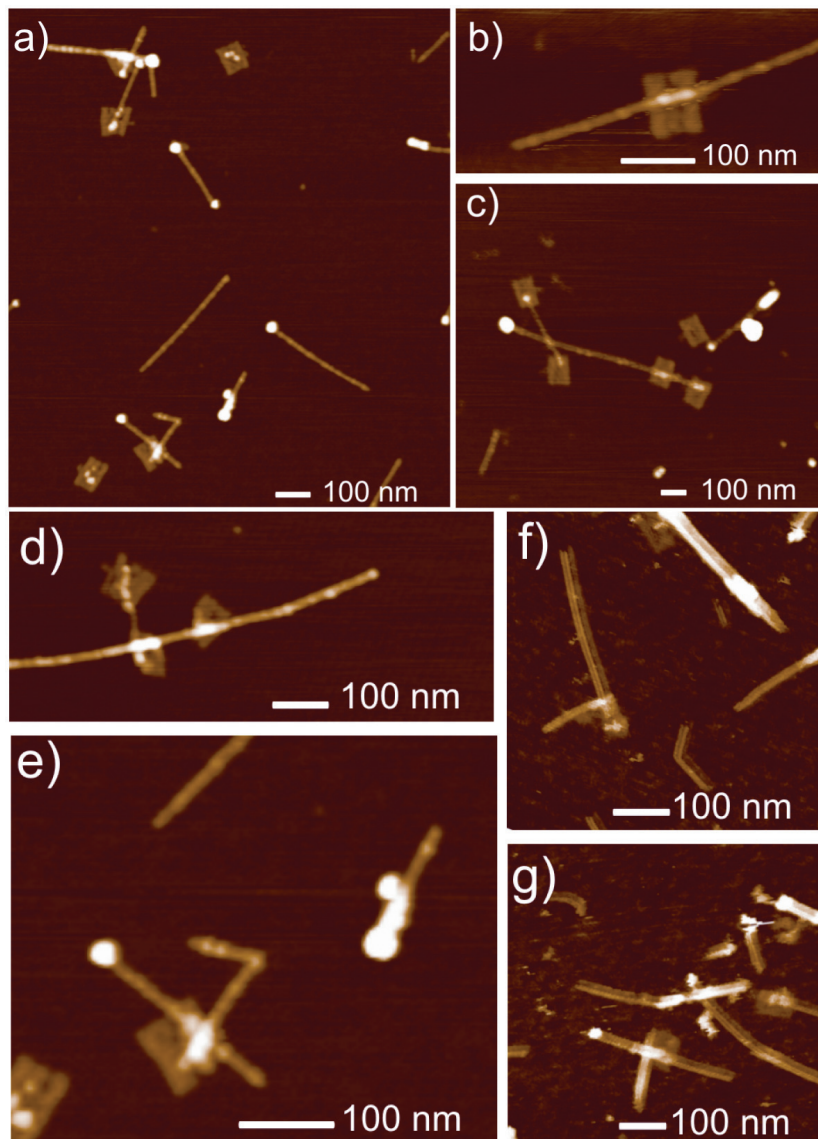
Figure 3.7. Atomic force microscope images about SWCNTs assembled on DNA origami structures in 5-pixel configuration (a), (b), (c), in 10-pixel configuration (d), (e) and in 21-pixel configuration (f), (g). The figure (a) illustrates the yields in structure formation. Adapted with permission from Publication I of this thesis.

Table 3.1. A table representing the yields in the structure formation. There the incubation time, the total number of origami/CNT structures analysed (N), number of structures having a single SWCNTs/origami (N single CNT), number of structures having two CNTs/origami (N two CNTs), and the number of structures having SWCNTs correctly aligned according to the binding site rows from those, which had two SWCNTs attached (N well aligned).

Type	Time [days]	N	N (Single CNT)	N (two CNTs)	N (well aligned)
5 pixels					
	1	283	123 (43.5 %)	NA	44 (35.8 %)
	4	370	206 (55.7 %)	NA	98 (47.6 %)
	7	208	69 (33.2 %)	NA	22 (31.9 %)
10 pixels					
	2	344	169 (49.1 %)	15 (4.4 %)	2 (13.3 %)
	3	287	225 (78.4 %)	40 (13.9 %)	13 (32.5 %)
23 pixels					
	1	184	63 (34.4 %)	8 (4.3 %)	1 (12.5 %)
	3	152	28 (18.4 %)	4 (2.6 %)	1 (25.0 %)

a wide field AFM image illustrating yields (a)). There as high as 78 % of the origamis had at least one SWCNT. In this case 14 % had two SWCNTs and from these 33 % were aligned according to the pixel lines. In the case of 21 pixel configuration (AFM images, Figure 3.7 (f) and (g)), again 34 % yield was gained in binding at least one SWCNT. The yield in binding two SWCNTs per origami was, however, a bit lower (4 %). It has been widely acknowledged that the DNA origami designed by P. W. K. Rothemund have some in-built stress and therefore the DNA origami structures, instead of being straight and open, are most likely bend in the solution [47]. Therefore we assume that there is some sterical hindrance for the second SWCNT to bind on the opposite sides of the DNA origami substrate.

3.2.2 Conclusions

As a conclusion, we were successful in assembling and aligning SWCNTs with the help of the DNA origami method. In the case of crossed structures, 33 % in alignment fidelity of the SWCNTs relative to the binding sites was achieved with the SWCNTs on the same sides of the origamis. Significantly better results were obtained in the case where SWCNTs were assembled on the same side of the origami structure in comparison to the case where the SWCNTs were aligned on opposite side of the origami (13 % in the same side case versus 5%

in the opposite side case). The binding yield of attaching at least one SWCNT on origami substrates reached as high as 78 %. Best fidelity of alignment was obtained in the single SWCNT per origami case (48 %).

The purpose of this study was to demonstrate a method for attaching SWC-NTs on the DNA origami structures with the help of STV-biotin interaction. We did not conduct any major optimization steps during the study. Thus the introduced approach could be improved with several methods. First, there was no optimization done for the SWCNT to DNA origami ratio. By adjusting this ratio, one could get rid of structures having multiple origamis/CNT and aggregates of structures. Moreover, optimization of concentrations could lead into shorter assembly times.

However, we assume that the binding efficiencies could be increased the most by improving the purification protocols for both the SWCNT/ssDNA conjugates and the DNA origami substrates. In this study, all the purification steps were conducted with spin filtering. In this procedure the solution to be purified is injected to a container having a filter membrane. During centrifugation, the material to be removed goes through the filter. On the other hand the desired structures, being too large to go through the filter, stay in the container. During the process the entire volume of the purified solution does not go through the filter membrane which means, that there is always some residues left in the container. Therefore, in our case there is always some free biotinylated strands taking binding positions from the SWCNTs in the DNA origami substrate. Nowadays a much more efficient approach, namely the agarose gel electrophoresis, has become a standard tool in the DNA origami structure purification. In addition in being superior in purification power compared to the spin filtering approach, recently progress has been made in the recovery levels of the structures. As an example, G. Bellot et al. reported 71 % recovery yield for their 6-helix bundle 3-D DNA origami structure [88]. Therefore, purification of the ssDNA/SWCNT solutions and the DNA origami substrates before assembly would for sure lead into significantly larger yields. One could also separate the case of having two SWCNTs/origami from the case of a single SWCNT/per origami by conducting a gel electrophoresis purification step after the assembly.

Moreover, after the introduction of DNA origami design and analysis software, people have switched into using their own designs rather than the original structures designed by P.W.K. Rothemund. This has allowed the possibility to design fast and easily stress free structures. We would assume that these kinds of new designs would ramp the yields up, especially in the case of assembling the SWCNTs on the opposite side of the origami structure.

4. Assembling noble metal nanoparticles on DNA origami substrates

The surface plasmon resonance (SPR) and the localised surface plasmon resonance (LSPR) involve the collective oscillation of the surface charge density. In the first case the resonance is bound to a planar interface, while in the other one on nanoparticle surfaces. In both cases light can be confined to dimensions well below the wavelength of light. This confinement of light leads into strong electromagnetic fields in the close vicinity of the particle or the interface surface. In the case of the SPR, the field decay length is in the range of couple of hundreds of nanometers, while in the case of the LSPR the decay length is a couple of tens of nanometers. The strong electric fields of the SPR and LSPR can be harnessed for sensing applications. For more information on biosensing applications taking advantage of plasmonics, there is an excellent recent focus issue in the Nature Photonics covering this topic [89].

In Publication II of this thesis, silver nanoparticle bow-tie antennas were assembled with the DNA origami method. The system was designed to operate as an optical DNA sensor taking advantage of the LSPR resonances provided by spherical silver nanoparticles. There exists already a variety of DNA sensors such as the TaqMan probes and the molecular beacons. However, these methods require PCR (polymera chain reaction) multiplication steps, which could possibly be avoided with the origami/bow-tie antenna system due to the strong optical response of the silver bow-tie antennas.

Before dwelling into more detail in the bow-tie antenna system, the physics behind SPR and LSPR are introduced. In addition, the optical response of metals in general is presented briefly. The operation of the bow-tie antenna involves the collective behaviour of several single nanoparticle plasmon modes. Therefore the theory of hybridization of plasmon modes is also introduced.

4.1 Optical properties of noble metal nanoparticles

4.1.1 Optical response of metals

The dielectric response of an electron gas can be described by the relation [90]

$$\vec{D} = \epsilon_0 \vec{E} + \vec{P} = \epsilon_0(1+\chi)\vec{E} = \epsilon\epsilon_0\vec{E}. \tag{4.1}$$

The external electric field $\vec{E}$ gives rise to a polarization density $\vec{P} = \epsilon_0\chi(\omega)\vec{E}$ and a electric flux density $\vec{D}$. The terms in the equation are the permittivity of vacuum ϵ_0, the electric susceptibility χ and the electric permittivity ϵ of the medium.

One can derive a relation for the material permittivity for metals by considering the response of non-interacting conduction electrons to an oscillatory electric field. This treatment is known as the Drude-Lorentz-Sommerfeld model [91]. If a damping constant $\Gamma = \tau_{coll}^{-1}$ is incorporated into the equation of motion for the electrons, arising from collisions of the electrons with lattice impurities and phonons with τ being the average time between collisions, one gets the relation [92]

$$\epsilon(\omega) = 1 - \frac{Ne^2}{\epsilon_0 m(\omega^2 + i\Gamma\omega)} = 1 - \frac{\omega_p^2}{\omega^2 + i\Gamma\omega} = 1 - \frac{\omega_p^2}{\omega^2 + \Gamma^2} + i\frac{\omega_p^2\Gamma}{\omega(\omega^2 + \Gamma^2)}, \tag{4.2}$$

or

$$\epsilon(\omega) = 1 + \chi^{DS}(\omega). \tag{4.3}$$

The $\chi^{DS}(\omega)$ represents the Drude-Sommerfeld susceptibility. In Equation 4.2, ω is the angular frequency of the oscillating electric field, N the electron density, m is the effective electron mass and ω_p the plasma frequency described by the equation

$$\omega_p^2 = \frac{Ne^2}{\epsilon_0 m}, \tag{4.4}$$

where the e is the electron charge and m the effective electron mass.

The simple free-electron scheme is successful in describing the response of some metals, e.g. alkali metals like lithium and sodium, fairly accurately [92]. However, in many cases, such as in the case of the noble metals gold and silver, a treatment involving only conduction electrons is not enough and a more sophisticated model is needed. In addition to the conduction electrons, core electrons give a significant contribution to the optical response and therefore interband transitions have to be taken into account in permittivity Equation [93]
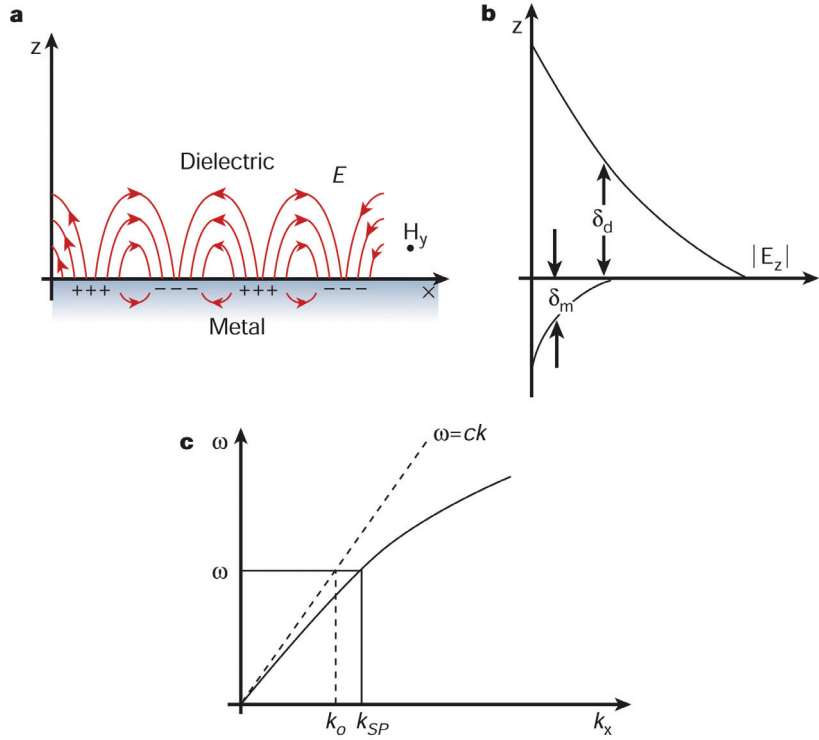
Figure 4.1. Surface-plasmons are collective oscillations of the surface charge density at an interface between a dielectric and a metal (a). The electromagnetic fields localized on both sides of the interface are exponentially decaying evanescent fields (b). The decay lengths of the electric field in the dielectric is in the order of $\delta_d = 100$ nm and in metal $\delta_m = 10$ nm, respectively. The dispersion relations for a surface plasmon mode along with free space light $\omega = ck$ is presented in (c). Reproduced with permission from Ref. [94].

$$\epsilon(\omega) = 1 + \chi^{DS}(\omega) + \chi^{IB}(\omega). \tag{4.5}$$

With this equation the polarizability and absorption properties, and hence the optical response of metals can be described.

4.1.2 Surface plasmon polaritons

Surface-plasmon-polaritons (SPPs) are quanta of oscillation of the surface charge density coupled with electromagnetic fields i.e. photons . The SPPs can occur at any interface fulfilling a condition $\epsilon_m < -\epsilon_d$ between the permittivities of the materials forming the interface [94]. This condition holds e.g. for an interface between a noble metal, such as Au or Ag, having a large negative real part of

29

the dielectric constant, and a dielectric like air. The oscillatory nature of the surface charge density is illustrated in Figure 4.1 scheme (a). The electromagnetic fields localized on both sides of the interface are evanescent in nature with exponential decay lengths being in the range of $\delta_d = 100$ nm in the dielectric and $\delta_m = 10$ nm in the metal respectively, Figure 4.1 (b).

One can derive a dispersion relation which relates the SPP wave-vector to its angular frequency (or energy) for the SPP mode at a dielectric-metal interface from the Maxwell's equations [95]

$$k_{SPP} = \frac{\omega}{c} \sqrt{\frac{\epsilon_d \epsilon_m}{\epsilon_d + \epsilon_m}}. \tag{4.6}$$

In the equation the frequency dependent permittivities are marked for the dielectric as ϵ_d and for the metal ϵ_m, while ω is the angular frequency and c the speed of light in vacuum.

The dispersion relation (Equation 4.6) is illustrated for a dielectric-metal interface along with a light line (dispersion relation for light $\omega = vk$, where $v = \frac{c}{n}$ is the phase velocity of light, ω the angular frequency, k the wavenumber, n the refractive index of the medium and c the speed of light) in Figure 4.1 (c). The SPP dispersion relation approaches the light-line with small wave-vector values starting to significantly deviate from it quite rapidly with increasing wavenumber. This imposes a challenge in exciting the SPPs by light and therefore special arrangements, such as the Kretschmann or the Otto -configurations, have to be used to compensate the mismatch between the momentum of the free space light and that of the SPP illustrated in Figure 4.1 (c) [94].

The most interesting properties of the SPPs stem from the strong confinement of the electric fields in the metal-dielectric interface. This strong confinement has enabled the possibility to take advantage of the SPPs in applications such as surface-enhanced Raman-scattering based sensing [96] and in enhancement of fluorescence [97].

4.1.3 Localised surface plasmon resonance

In the previous section, a collective resonance of the surface charge density at planar interfaces coupled to photons was introduced. In this section, a brief introduction will be given on the optical response of small metal particles to an electromagnetic excitation. The focus will be in nanosized noble metal nanoparticles. The optical response of the nanoparticles can be investigated analytically for spherical and ellipsoidal particles of arbitrary refraction index with the Mie-theory, although more complex shapes and particle arrays require numerical

techniques such as the finite-difference time-domain (FDTD) method, the finite element method (FEM) or the T-matrix method [98].

One can get an insight into the physics of LSPR with the quasistatic approximation. There the particles are assumed to be significantly smaller compared to the wavelength of the electromagnetic field. Although time variation of the electromagnetic field is taken into account, the spatial dependency and therefore retardation effects are ignored. The treatment gives good results for particles with dimensions less than ∼ 1% of the wavelength of the incident light [91]. However, quite often the approximation is used for significantly larger particles.

The static polarizability of a spherical particle of radius R can be expressed by the relation [91]

$$\alpha = 4\pi\epsilon_0 R^3 \frac{\underline{\epsilon_p} - \underline{\epsilon_m}}{\underline{\epsilon_p} + 2\underline{\epsilon_m}}, \qquad (4.7)$$

there $\underline{\epsilon_p}$ and $\underline{\epsilon_m}$ are the complex permittivities of the particle and medium hosting the particle, respectively. The internal electric field of the nanoparticle shows resonance behaviour when

$$|\underline{\epsilon_p} + 2\underline{\epsilon_m}| = \text{minimum}. \qquad (4.8)$$

If a frequency-dependent form of the complex permittivity is used, defined as $\underline{\epsilon}(\omega) = \epsilon'(\omega) + i\epsilon''(\omega)$, and a real constant value for the permittivity of medium is assumed, the following condition is obtained

$$\underline{\epsilon_m}(\omega) = -2\underline{\epsilon_p}. \qquad (4.9)$$

This is the resonance condition for a dipole resonance in the quasistatic approximation. If neglecting the damping effects introduced in material model Equation 4.2, a simple model for a Drude metal for the metal particle permittivity can be given by $\epsilon(\omega) \approx 1 - \frac{\omega_p^2}{\omega^2}$, where the plasma frequency is defined by Equation 4.3. Thus combined with Equation 4.9 a relation for the resonance frequency is obtained [92]

$$\omega_{SP} = \frac{\omega_p}{\sqrt{1 + 2\underline{\epsilon_p}}}. \qquad (4.10)$$

The equation holds for dipole resonances induced in small particles. Conditions for higher order resonances can also be derived with the quasistatic approximation. For these a more general relation for the LRSP resonance position states [98]
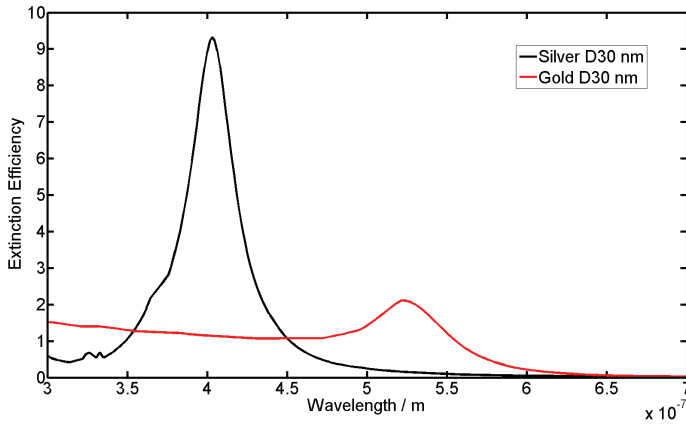
Figure 4.2. Calculated extinction efficiencies for a spherical gold and silver nanoparticle of 30 nm diameter with the Mie-theory. For the calculation, water was chosen as the medium with the refractive index of n=1.33. The maximum value for silver, 9.3, occurs at $\lambda = 403.1$ nm and for gold, 2.1, at $\lambda = 521.5$ nm, respectively.

$$\omega_{SP}^{l} = \sqrt{\frac{l}{l+(l+1)\epsilon_m}}\omega_p \quad l = 1,2,3\cdots. \tag{4.11}$$

In the equation, l is the multipole order, and for a dipole l=1. The LSPR frequency derived with quasistatic approximation is independent of particle size. However, with increasing particle size, the LSPR shifts to longer wavelengths, a phenomenon the Mie-theory is able to predict.

In Figure 4.2, there are plots of extinction efficiencies for a silver and a gold nanoparticle calculated with the Mie-theory. The particle size is the same as in for assembling silver nanoparticle nanostructures with the DNA origami method that will be presented later in this chapter. The nanoparticles have been embedded in water (refractive index n=1.33). The calculation reveals also the differences between the two noble metal materials. Although the plasmon energies for the two are relatively close to each others (9.0 eV for silver and 8.55 eV for gold) [99], they have quite different threshold values for the interband transitions (for Ag 3.9 eV and 2.4 eV for Au) [91]. In the case of Au, this leads to considerable absorptive losses at wavelengths shorter than about 500 nm, which leads to a significant damping of the LSPR [92]. The phenomenon is evident in the figure.

4.2   Hybridization of localised surface plasmon resonances

In the previous section the response of individual metal nanoparticles to electromagnetic excitation was discussed. When two of these particles are brought

to close proximity of each other to form a dimer of particles, in addition to the external electric field, the particles start to feel the near-field of the other particle. This leads to considerable changes in the optical properties of the system, which can be explained with a plasmon hybridization model introduced by Prodan et al. analogous to the hybridization of atomic orbitals in molecules [100, 101]. There individual plasmon modes hybridize to form a lower energy mode (named as the bonding plasmon mode) and a higher energy mode (named as the anti-bonding mode) [102]. These are basically the in-phase and out-of phase oscillations of the individual surface charge densities. The splitting of the individual particle plasmon mode into new ones is illustrated in Figure 4.3.

The strength of the coupling between the individual particle plasmon modes is dependent on several parameters, one being the polarization of the exciting electromagnetic field [103]. The coupling is strongest when the electric field is polarized along the line connecting the centres of the particles. There the bonding plasmon mode, being lower in energy, leads into red-shift in the far field spectrum. In the case of a homodimer i.e. particles of the same size and morphology, the out-of-phase oscillation is not visible in the far-field spectrum and is therefore named as a dark mode. The weakest coupling stems from the E-field polarized perpendicular to the line connecting the particle centres. There again the out-of-phase oscillation is a dark mode, while the in-phase oscillation leads into a slight blue shift of the far-field spectrum. The atomic model analogue can be taken even further by naming the two hybridized resonances as the $\sigma/\sigma*$ and the $\pi/\pi*$ modes referring to bonds in molecules [104].

In addition to the electric field polarization, the strength of the plasmon hybridization is strongly dependent on the interparticle separation [105]. The effect is so prominent that it could be used as nanosized ruler [105]. The interaction strength grows with diminishing interparticle separation until the quantum regime where tunneling of electrons from one particle to the other becomes possible [106, 107]. When the interparticle separation gets smaller the individual nanosphere plasmons with a given angular momentum can interact with plasmons of different angular momenta (illustrated in Figure 4.3 with the dashed green lines) causing extra shifts of modes illustrated in Figure 4.3 with the green arrows [102]. The scattering of electromagnetic radiation from nanospheres is naturally described in spherical coordinates. The multipolar modes described in 4.11 are solutions of the Maxwell's equations in spherical coordinates giving also angular momentum numbers.

The discussion so far has concentrated on plasmon hybridization in dimers composed of identical particles. The case of non-identical particles, such as
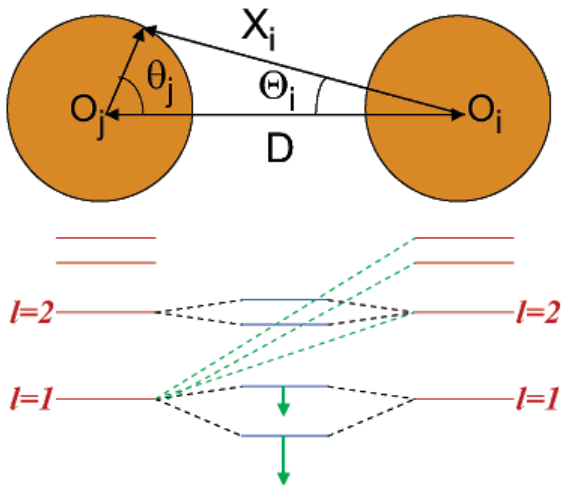
Figure 4.3. Coupling of individual spherical nanoparticle plasmon modes leads into new hybridized modes. The coupling strength is dependent on the interparticle separation and when the distance between the particles gets smaller, plasmon modes with angular momentum l can mix with different angular momentum on the other particle (indicated with green dashed lines). This interaction causes extra shifts for the dimer plasmon (solid blue lines and green arrows). Reproduced with permission from Ref. [102].

particles of different size or material, leads into several new spectral properties such as Fano-resonances and an optical nanodiode effect [108]. Pena-Rodriques et al. observed that coupling of the individual particle plasmon modes in a dimer composed of silver and gold nanoparticles with the size-ratio 3:1 lead to strong Fano-resonance signals which could be used for optical sensing [109]. In our work, we have considered hybridization of modes in a bow-tie antenna configuration. This will be discussed in Section 4.3.3.

4.3 Assembling plasmonic structures with DNA

In addition to the DNA construction material, the nanoparticles themselves play an important part in building plasmonic structures. Nowadays there are methods available for manufacturing practically all sorts of metal nanoparticle shapes from spheres [110] to rods [111] and complex branched structures [112]. In addition to the size of the metal nanoparticle, there are other factors influencing in the particles' optical properties. In spherical particles, the LSPR resonance is mainly dipolar in nature. However, the number of resonance peaks increases as the number of possible ways to polarize the particle increases. In addition, sharp features like corners effect in the position of the LSPR frequency [113]. These factors eventually influence the outcome of the plasmonic

construction.

Assembly of these different metal nanoparticle shapes into complex geometries involves several forces such as van der Waals, electrostatic, solvation / depletion, friction/lubrication and capillary forces [114, 115]. As an example, electrostatic forces tend to easily aggregate gold and silver nanoparticles in ionic solutions. As a solution, to prevent uncontrolled aggregation of the nanoparticles, they are coated with some soft organic material, such as the alkanethiolates [116, 117]. K. Aslan et al. were able to prepare 11-mercaptoundecanoic acid covered AuNPs in the presense of nonionic Tween 20 surfactant resulting in nanoparticles stable in broad pH ranges. Moreover, the carboxylic acid groups readily provided means for 1-ethyl-3-(3-dimethylaminopropyl)carbodiimide (EDC) / N-hydroxysuccinimide (NHS) mediated coupling reactions [118].

Another extremely practical coating ligand option is DNA. Due to its versatility, it can be used to compensate for the Van der Waals forces-driven aggregation of nanoparticle cores by steric hindrance provided by the DNA strands. Moreover the effect can be easily controlled by adjusting the length of the DNA strands. The stiffness of the ligand can be also controlled by using dsDNA instead of ssDNA. On the other hand, the electrostatic-driven aggregation can be controlled through ionic strength of the solution containing the ssDNA functionalized particles. Even more importantly, DNA provides a means for controlled assembly of the nanoparticles through Watson-Crick base recognition.

The first reports on gold nanoparticles assembled with the help of thiolated ssDNA strands, a method that has become afterwards a standard tool for preparing high concentration AuNP dispersions in high ionic strength solutions, was reported by Mirkin et al. [119] and A. P. Alivisatos et al [120]. After the reports of Mirkin and Alivisatos, research groups have prepared ever more complicated metal nanoparticle structures ranging from plasmonic molecules [121], linear polymers [122] to 2 [123] and 3 -D crystals [124] with the help of DNA-driven assembly. These different kinds of particle geometries are illustrated in Figure 4.4. In the first reports, the nanoparticles had full surface coverage of ssDNA strands. Later a more complicated homofunctionalization [120] (where a single DNA strand/nanoparticle is used) and asymmetric functionalization [126] (DNA linker strands are not symmetrically distributed on the particle surface) have provided means for fabricating complex plasmonic structures.

Besides directly connecting nanoparticles together with a DNA linker, the nanoparticles can be organized on DNA scaffolds such as DX and TX tiles offering possibility for preparing 2-D crystals illustrated in Figure 4.4. The more recent templating strategy, namely the DNA origami method, can also be used
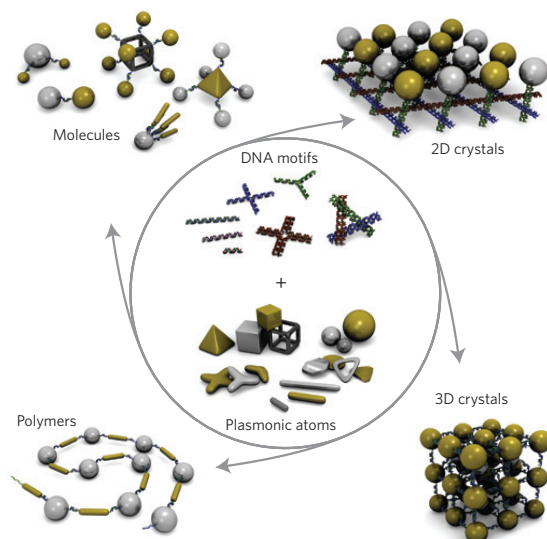
Figure 4.4. After the first DNA-driven assembly of nanoparticles into larger constructions, ever more complicated systems have been reported starting from plasmonic molecules even to 3D crystals. Reproduced with permission from Ref. [125].

for the purpose. Figure 4.5 highlights some gold nanoparticle assemblies obtained through the DNA origami method. There in Figure 4.5 (A), a chain of nanoparticles with altering dimensions was assembled on triangular-shaped DNA origamis [38]. In 4.5 (C), a gold nanoparticle dimer has been formed on a DNA origami pillar standing on a substrate, enhancing the fluorescence emission from dye molecules [41]. The DNA origami method has been used even to prepare chiral plasmonic molecules with tailored optical response (B) [42].

4.3.1 Functionalization of silver nanoparticles with DNA

When it comes to assembling metal nanoparticles on the DNA origami substrates, the work has mainly focused on gold nanoparticles. The reason for this might be in the strong coordination chemistry between sulphur and gold offering opportunity to take advantage of thiolated oligonucleatides. Silver undergoes oxidation more readily than gold making the ligands more labile on the AgNP surface and the particles tend to aggregate irreversibly in solutions of high ionic strength [39]. To overcome this issue, methods have been developed where multiple sulphur moieties are used instead of single thiols [127–130]. The same approach was adapted for the functionalization of our AgNPs for AgNP bow-tie antenna fabrication.

Preparation of the ssDNA functionalized AgNPs was adapted from Pal et al. [39] with slight modifications. The sodium citrate stabilized silver nanopar-

Figure 4.5. Some selected AuNP assemblies on DNA origami substrates. In (A) a row of AuNPs with altering particle diameter has been formed on triangular DNA origamis, in (B) chiral plasmonic molecules have been assembled with DNA origami sticks and in (C) an AuNP dimer has been constructed on a DNA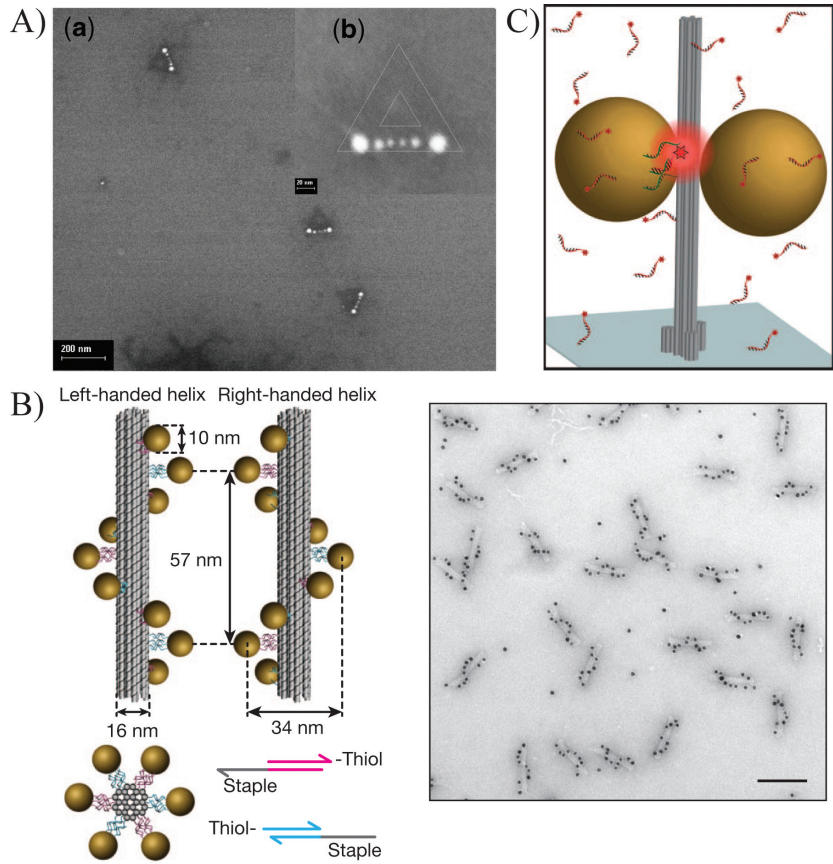 pillar attached to a substrate. Figure (A) reproduced with permission from Ref. [38], (B) from Ref. [42], and (C) from Ref. [41].
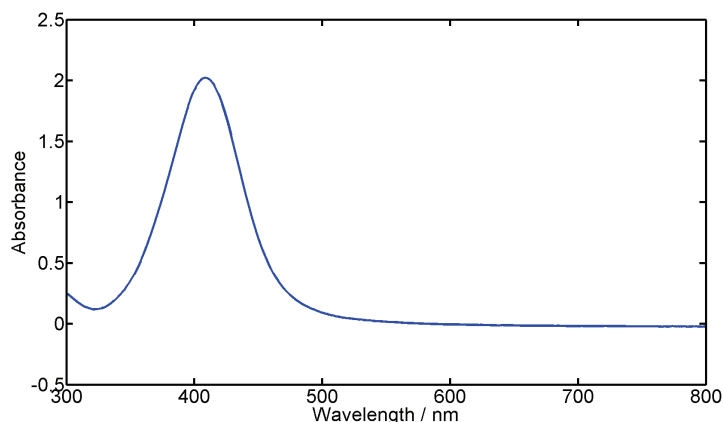
Figure 4.6. A typical absorbance spectrum recorded from ssDNA functionalized silver nanoparticles of 30 nm in diameter. The peak of absorption $A \approx 2.0$ occurs at $\lambda = 409$ nm. The particles were in 1 X TBE, 350 mM NaCl buffer solution.

ticles in water were bought from Ted Pella (Biopure 50X concentrate) with average diameter of 28.7 nm with first standard deviation of 3.6 nm (68 % of the nanoparticles will have a size within (28.7±3.6) nm). According to the manufacturer the peak of absorbance occurred at $\lambda = 402$ nm. The ligand exchange was performed in 0.5 x TBE (44.5 mM TRIS, 44.5 mM Boric acid, 1 mM ethylenediaminetetraacetic acid) buffer solutions having chimeric phosphorothioated (ps-po-chimeric) DNA of sequence ($5'$ $TTTTTTTTTTTTTTT^*C^*A^*T^*G^*C^*G^* G^*G^*C$ $3'$) (bought from Integrated DNA technologies) where the bases marked with a star have been replaced with phosphorothioated ones. The purpose of this region is to anchor the ssDNA strand on the AgNP surface with multiple sulphur chemisorptions. The ssDNA was used in 8000 times excess compared to the AgNPs to ensure full coverage of the particle surfaces. The AgNP concentration in the starting solution containing ssDNA material was 5 nM. The ligand exchange was done on a course of overnight incubation followed by sodium chloride addition in 1 μl steps over 24 h to obtain 350 mM salt concentration in the final solution. Excess ssDNA material was removed by spin filter columns (450 kDA cut-off weight) and the DNA conjugated AgNPs were brought up into desired concentrations with 1 X TBE, 350 mM NaCl buffer solution. Figure 4.6 presents a typical absorbance spectrum from a ready ssDNA functionalized AgNP solution.

4.3.2 Assembling silver nanoparticle trimers and bow-tie antennas with the DNA origami method

The DNA origami AgNP bow-tie antenna assembly process is illustrated in the schematic Figure 4.7. The bow-tie antenna was composed of two different origami structures, named as Tile 1 and Tile 2. The nomenclature has been adapted from research conducted with DNA origami to form larger polymer and 2-D structures through using individual DNA structures as tiles. Both structures were rectangular (92 nm x 72 nm) planar DNA origamis consisting of the M13mp18 scaffold plasmid and in total 192 staple strands. In both cases, staples from the edges of the origamis were mainly omitted in order to prevent uncontrolled stacking of the origami structures stemming from π-staking of the blunt DNA-strand ends. However, in the case of both tiles, three staples with 11-base-long ssDNA extensions were included in the structures. In the case of Tile 1, these strands located in the left edge and in the Tile 2 case in the right edge, respectively. The 11-base long ssDNA extensions of the individual tiles were complementary to each other and therefore pairs of origami could be assembled through thermal annealing of the structures.

In addition to these ssDNA extensions, both of the tiles had three binding positions for the DNA functionalized AgNPs. Each of the binding position consisted of a group of three modified staple strands having 11-base-long ssDNA extensions complementary to the ssDNA strands in the AgNPs (the thymine repeat). Most likely a single ssDNA binder strand would not have been sufficient for holding the silver nanoparticles (especially this large) attached in the DNA structure and therefore three strands for anchoring was used. When the individual DNA tiles were combined with the ssDNA functionalized AgNPs, the bow-tie antenna structures could form upon thermal annealing (Figure 4.7). Usually when referring to bow-tie antenna structures, antennas made out of two triangles are meant. However, as our three particle systems form triangle-like shapes, we call our united nanoparticle trimer systems as bow-tie antennas.

The individual DNA origami tiles were themselves prepared with standard thermal annealing from 90 °C to 20 °C with the rate of 1 °C/min in 0.1 °C steps in 1 x TAE Mg^{2+} (40 mM TRIS, 19 mM acetic acid, 1 mM EDTA, 12.5 mM magnesium acetate). The DNA structures were formed in a large excess of the staples compared to the scaffold strands. Efficient removal of these excess oligonucleotides is of extreme importance for the AgNP origami structure formation. Especially the modified staples, responsible for AgNP binding and
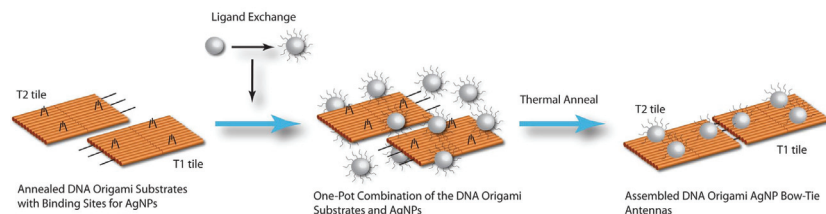
Figure 4.7. The DNA origami bow-tie antenna consists of two individual DNA origami tiles having predefined binding positions for the DNA functionalized AgNPs. The two-origami tiles were annealed together with the AgNPs overnight to form the DNA origami AgNP bow-tie antennas.

DNA origami pair formation, can considerably interfere the structure formation process. A traditional and straightforward approach would be the spin filtration used in Chapter 3 for the SWCNT assembly. However it has been observed that obtaining a good binding efficiency of nanoparticles into the origami structures requires more delicate purification methods. As was discussed earlier, spin filtration leaves a considerable amount of the undesired residues. Therefore the DNA structures for these experiments were purified with the help of agarose gel electrophoresis. Ready annealed DNA origami structures were run in 1 % agarose gel (in 1 X TAE Mg^{2+}) for 45 min with 90 V applied between the electrodes. Purified structures were extracted with spin filter columns (BioRad freeze and squeece columns).

The relatively large particle size used (30 nm in diameter) posed another challenge in AgNP structure formation with the DNA origami method, in addition to the purification of the DNA origami structures. Namely now that the whole AgNP surface is covered with ssDNA, complementary to the binding positions in origamis, there is a risk that a single particle binds to more than a single binding position. This can take place inside an individual origami, or a single particle can bind to several different origamis. The latter case leads to aggregates of DNA origami structures. This problem can be circumvented by using a high particle to origami ratio. As an example, Kuzyk et al. used AuNP particle concentrations in the range of several hundreds nanomolar [42].

The high gold-nanoparticle concentrations in high ionic strength buffers can be achieved with the help of the drug 2,6-di-tert butyl-4-(3-hydroxy-2-spiropentylpropyl)-phenol (BSPP). Thiolated ssDNA ligands can readily replace the molecule leading into ssDNA functionalized AuNPs with high concentration. However, BSPP was found to be incompatible with AgNPs. Incubation of AgNPs in solution containing BSSP led in our experiments into destruction of the particles. Another option would be to functionalize the AgNPs in the presence of a non-ionic protective surfactant Tween 20 [118]. The surfactant attaches to the AgNP

surface by physisorption forming a protecting layer against AgNP aggrega-
tion. This layer can be replaced with sulfur modified ssDNA strands binding by
chemisorption. Some experiments were conducted with Tween 20 for bow-tie
antenna formation, but no major improvements were observed. More experi-
ments should be conducted to harness the full potential of the surfactant.

Due to the aggregation issues related to the AgNPs, the structure formation
possessed an optimization problem between the relative concentrations of Ag-
NPs and the origamis. In the assembly process, the DNA origami concentration
was kept intentionally quite low, in order to prevent cross linking of the DNA
origami caused by multiple origami binding into single particle. The best re-
sults were obtained when particles were used in 3:1 concentration excess com-
pared to the DNA origamis with the following mixing protocol

- 10 μl Tile 1 + 10 μl Tile 2 + 10 μl DNA functionalized AgNPs + 20 μl 1 X
  TBE (89 mM TRIS, 89 mM boric acid, 2 mM EDTA) 350 mM natrium chloride
  (NaCl).

Prior to the assembly of DNA origami bow-tie antennas, DNA AgNP trimers
i.e. DNA structures with three particles, were prepared. These structures were
formed with the same protocols as the antennas. As the only difference: only
single tile type of was used (either Tile 1 or Tile 2) and the other tile was re-
placed with 1 X TBE 350 mM NaCl buffer. The 50 μl reaction volume was
thermally annealed overnight from 45 $^{\circ}$C to 4 $^{\circ}$C.

The results were investigated with transmission electron microscope (TEM)
on carbon grids. Due to the fact of basically having carbon on carbon, getting
sufficient contrast for DNA structure detection is challenging. Therefore the
samples to be imaged were negatively stained with uranyl acetate. There are
TEM images in Figure 4.8 (a) about well formed DNA origami AgNP trimers
and in (b) DNA origami AgNP bow-tie antennas. The structures appear well
formed and the DNA substrate is clearly visible under the particles. According
to TEM measurements, the separation between the two central particles in the
bow-tie structure was 6.4 ± 0.9 nm and between the AgNP pair at the edge of
the antenna was measured to be 12.2 ± 1.1 nm.

Agarose gel electrophoresis was used after DNA origami AgNP structure for-
mation for verifying the proper assembly of the DNA origami AgNP structures.
The structures were run in 1 x TBE magnesium chloride gel for 2 h with 80
V applied to the electrodes. The applied voltage induces heat in the running
buffer and therefore to prevent DNA strand melting, the gel was placed in an
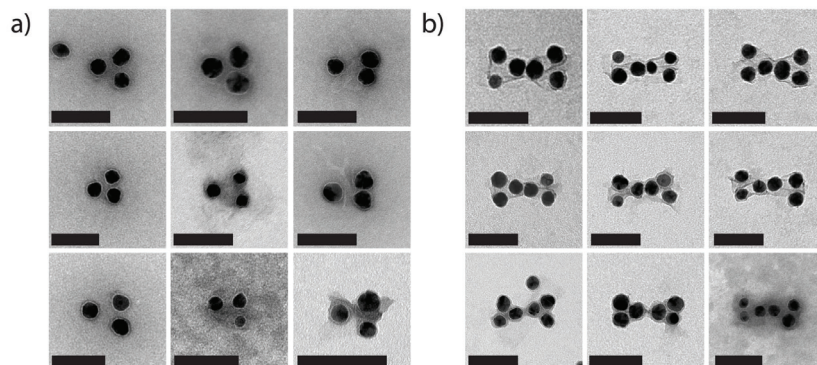
Figure 4.8. Transmission electron microscope images about DNA origami AgNP trimers (a) and bow-tie antennas (b). The scale bars are 100 nm.

ice bath. The gel was stained with SYBR gold (Invitrogen) DNA intercalating dye for UV-imaging of the results. Figure 4.9 presents the results. Three different sample sets were run in the gel. In lane three (L3) a sample containing pairs of DNA origami without AgNPs have been run. There are two bands visible. The faster running lower faint band contains individual DNA origami while the upper brighter one has the DNA origami pairs. In the lane two (L2) DNA origami AgNP trimers and in lane one (L1) DNA origami AgNP bow-tie antennas have been run. The bands containing bow-tie antennas and trimers are marked as I) and II), respectively. This was verified by extracting the material out from the gel and by imaging the extracted material with TEM. There is a faint band visible in L2 below the trimer band. This most probably contains pairs of origami, due to the fact that the Tile 1, used in this set of material to make the trimers, tended to pair slightly with itself to form origami pairs. However this was not verified by TEM imaging. The relative intensity of fluorescence was measured from the bands, with DNA origami pair band in L3 operating as the reference. The results are listed in the table next to Figure 4.9. According to the numbers, the DNA origami AgNP bow-tie antennas have formed with good yield.

4.3.3 FDTD-simulations on the optical properties of silver nanoparticle bow-tie antennas

As was mentioned in the beginning of this chapter, the DNA origami AgNP trimer/bow-tie antenna system could operate as a sensitive DNA detector. The ssDNA overhang strands in the DNA origamis should be designed in a fashion that they together form a complementary sequence for the cDNA to be detected. The presence of the cDNA would unite the individual origamis to form

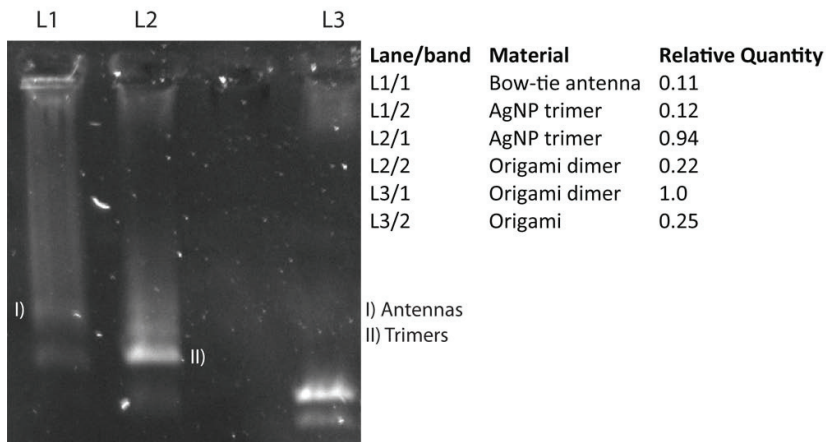| Lane/band	Material	Relative Quantity
L1/1	Bow-tie antenna	0.11
L1/2	AgNP trimer	0.12
L2/1	AgNP trimer	0.94
L2/2	Origami dimer	0.22
L3/1	Origami dimer	1.0
L3/2	Origami	0.25

Figure 4.9. Agarose gel electrophoresis mobility shift essay (EMSA) on AgNP DNA origami bow-tie antennas (L1) and AgNP DNA origami trimer structures (L2). As a reference, pairs of DNA origami tiles without AgNPs have been run in the gel (L3). Relative intensities obtained from the bands are also listed with DNA origami pair band being as reference.

a bow-tie antenna configuration with qualitatively distinct optical spectrum. The approach differs from conventional plasmonic nanoparticle based sensing methods. Instead of functionalizing the particles themselves with DNA complementary to the target DNA auxiliary structures, namely the DNA origamis, where used. This leaves more freedom to design a complex nanoparticle assembly optimal for sensing. FDTD-simulations were conducted for investigating the performance of such a scheme. The performance of the system was compared against a simple AgNP dimer setup. A metal nanoparticle dimer sensor, whose operation is based on the target-substance driven binding of two individual nanoparticles together, is one of the simplest configurations demonstrated for sensing purposes [131]. Therefore, it is natural to compare our more complex two-origami scheme, whose sensing operation is based on the binding of two individual AgNP trimers into a bow-tie antenna configuration, against the dimer configuration. The simulations were conducted with a commercial software package (FDTD-solutions, Lumerical). All the simulations were conducted in water (refractive index n=1.33) and the material parameters for silver were obtained by fitting to tabulated values of the permittivity of silver [132]. The structures were excited with a plane wave. The polarization of the electric field as well as the propagation direction of the plane wave was varied.

In Figure 4.10, simulation results for all the three different particle configurations are presented with electric field (E-field) polarized along the x-axis (Ex) and the plane wave have propagated along the z-axis (kz). Figure 4.10 (f) illustrates how the Cartesian coordinates are orientated relative to the particle
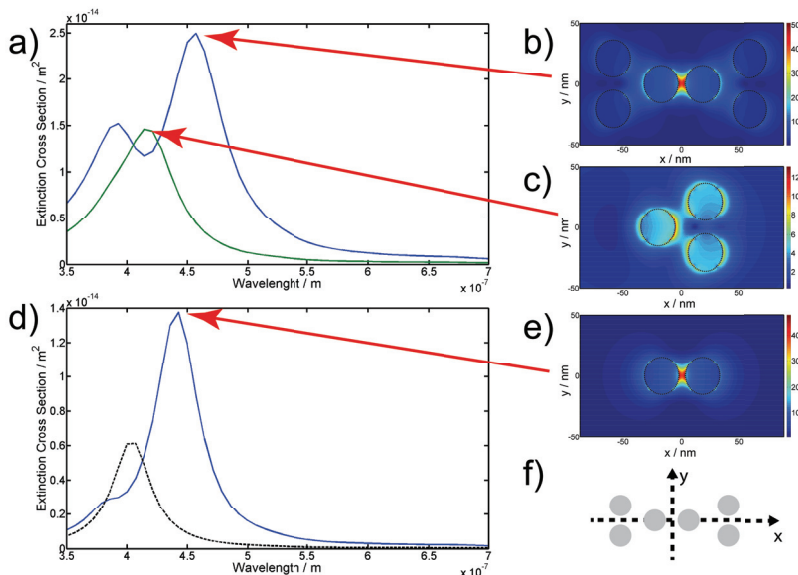
Figure 4.10. Finite-difference time-domain (FDTD) simulations with AgNP dimer, trimer and bow-tie antenna configurations. In (a) the extinction cross sections are plotted for an AgNP trimer consisting of three 30 nm AgNPs, together with extinction cross section from a bow-tie antenna consisting of six AgNPs also of 30nm in diameter. The absolute values for the electric field amplitudes are plotted for the bow-tie antenna (b) and for the trimer (c) at the peak locations indicated with the red arrows. In d) the extinction cross sections for an individual 30 nm AgNP together with the extinction cross section from an AgNP dimer consisting of particles of the same size has been plotted. When two AgNP trimers are coupled to form a bow-tie antenna, the extinction cross section profile changes dramatically due to the hybridization of LSPR-modes: a two-peak structure appears (a). The changes in the far-field spectra are more profound compared to the case when two nanoparticles are bound to a particle dimer where merely a shoulder is seen (d).The absolute value for the electric field at the peak location indicated by the red arrow for the dimer configuration is presented in (e). The coordinate system relative to the particle geometry is presented in (f). In all of the cases the structures were excited with a plane wave polarized along the x-axis with propagation direction along the z-axis.

configurations. There the bow-tie antenna lies in the (x,y)-plane the origin being in the center of the gap located between the two central particles. For the dimer configuration one just removes the four outer particles from the bow-tie system. As was observed in Section 4.2, the hybridization of individual plasmon resonances of two metal nanoparticles is strongly dependent on the interparticle separation. Therefore, for being able to compare the bow-antenna system against the dimer configuration, the gap between the two nanoparticles in the dimer was the same 6 nm as was in the bow-tie antenna between the two central particles.

In Figure 4.10 (d) the extinction cross section [m^2] for an AgNP sphere of 30 nm in diameter (black dashed line) and for a AgNP dimer with the same

particles size has been plotted. As a consequence of the hybridization of the single particle LSPR-modes, the resonance peak (at $\lambda = 443$ nm) has red-shifted about 39 nm from the single particle resonance (at $\lambda = 404$ nm). According to the molecule analogue picture, introduced in Chapter 4.2, the resonance peak represents the bonding σ mode while the antibonding $\sigma *$ one, being a dark mode, is not visible in the far-field spectrum.

Figure 4.10 (a) presents the extinction cross section profiles for the trimer and bow-tie antenna configurations. The peak value for the trimer occurs at $\lambda = 414$ nm representing the collective response of the combined three single AgNPs. When two AgNP trimers get united into the bow-tie antenna configuration, the extinction cross section spectrum changes dramatically: the trimer resonance peak splits into two new ones with split in energy $\Delta E = 443.2$ meV exhibiting strong coupling of the trimer LSPR modes. Hence, this more profound change in the AgNP trimer/bow-tie antenna configuration compared to the individual/dimers of particles case would suggest increased sensitivity in sensor action. Note that now both modes appear as bright modes, in contrast to the dimer where the other mode is (nearly) dark.

The extinction cross section profiles discussed above represent the far-field properties of the systems. In Figures 4.10 (b), (c) and (e) the absolute values for complex electric field amplitudes $|\vec{E}(\vec{r})|$ for the bow-tie antenna, trimer and dimer has been plotted at the peak wavelength values indicated by the red arrows. In the case of the bow-tie antenna, the E-field is largest in the gap between the two central particles. The enhancement of the electric field in the gap was 50. The stronger coupling between central two particles compared to the rest of the particles in the antenna structure was an expected result due to short interparticle separation and due the fact that the centres of the particles coincide at the x-axis.

Simulations with E-field polarized along the y (kz) and z (kx) -axis for the bow-tie antenna configuration are represented in Figure 4.11. The blue line represents the Ey-case while the black line the Ez, respectively. The case of Ex has been plotted again as a comparison (the red dashed curve). The inset reminds of the coordinate system. It is evident from the figure that for the cases of Ey and Ez, the coupling between two trimers is significantly lower compared to the case of Ex. The stronger coupling in the Ex case can be seen as larger red-shift of the main resonance peak from the individual trimer of particles case compared to the Ey and Ez polarizations and, in particular, the two-peak structure appears clearly only in the Ex polarization case. Actually, the Ez case reminds of the extinction spectrum that one would get from individual nanopar-
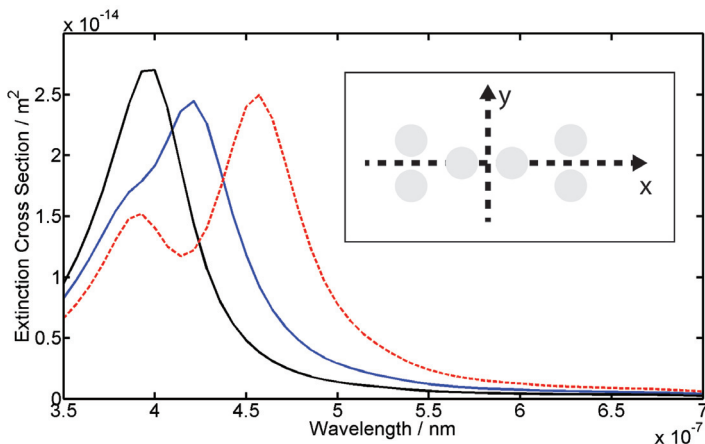
Figure 4.11. Finite-difference time-domain simulation results with AgNP bow-tie antenna configurations. The blue line represents extinction cross section obtained with E-field polarized along the y-axis propagation direction being along the z-axis. In the case of the black line, the E-field was polarized along the z-axis with x-axis as the wave propagation direction. The dashed red line is the x-polarized case operating as comparison. The red-shift of the main resonance peak in the case of Ex polarized excitation is significantly larger compared to the other E-field polarizations and, in particular, the two-peak structure appears clearly only in the Ex polarization case. This indicates stronger coupling of the trimer plasmon modes in the Ex case compared to the Ey and Ez cases.

ticles, although the peak is slightly blue shifted. This is a consequence from the coupling of the modes oscillating orthogonal relative to the interparticle spacing [104].

4.4   Conclusions

In this chapter, the fabrication of silver nanoparticle bow-tie antennas with the DNA origami method was presented. The system was constructed out of spherical nanoparticles. Hence, no complicated particle geometries, such as nanoprisms, were needed. The structures formed with high yields. Moreover, FDTD-simulations confirmed that one can use the origami trimer/bow-tie antenna system as a DNA sensor. There the presence of a target DNA caused the formation of the bow-tie antenna from the individual silver particle trimers, leading to more pronounced and quantitatively different (two-peak structure) changes in the optical spectrum compared to a simple particle dimer setup.

5. Controlling the formation of DNA origami structures with external trigger signals

5.1 Introduction

Dendrimers, first reported independently by Tomalia et al. [133] and Newkome et al., [134], are monodisperse repetitevily branched macromolecules with a compact three-dimensional structure. The structure of a dendrimer is schematically illustrated in Figure 5.1 (a). The molecule consists of a chemically distinct core, interior and surface groups. The structures can be synthesized with two approaches, either divergently or convergently [135]. In the first case one starts from the functional core by adding monomer units, and by this way build the structure layer by layer outwards. In the second approach one progress with the growth from periphery inwards, towards the core. The size of the dendrimer depends on the number of iterative growth steps, and therefore on the number of repeats of the monomer units making the branched structure. According to the amount of steps, the dendrimers are classified into different generations. Dendrons, on the other hand, are segments of dedrimers (Figure 5.1 (b)) with a chemically accessible focal point and a similar branched structure as in the case of the dendrimer. The large number of functional surface groups in these dendritic structures makes them very appealing offering possibility for multiple interactions – property named as multivalency.

In Publication III of this thesis, Newkome-type (PLLG1, generation 1) and polylysine dendrons (SSG2, generation 2), both with spermine surface units, were used in the DNA origami control experiments. The spermine surface units have been demonstrated to be able to bind strongly in the DNA phosphate sugar backbone with multivalent electrostatic interactions [136–138]. Moreover, the surface units in the dendrons were linked into the dendron frame structure with degradable linkers. The Newkome-type dendron's o-nitrbenzyl groups can be degraded with UV-light ($\lambda = 350$ nm) [139] while the polylysine den-
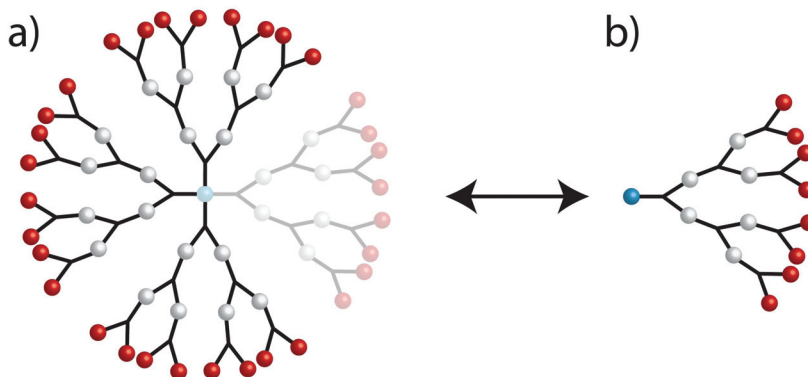
Figure 5.1. Dendrimers are repetitevily branched three-dimensional structures (a) with large number of surface groups. Denrdrons (b), on the other hand, are sections of dendrimers.

dron's dithiol linkers get cleaved with mild reducing agents such as dithiotretoil (DTT) [137]. After degradation, both dendrons loose their multivalent properties leaving behind individual amines and negatively charged carboxylic acid surface groups. The individual amines bind only weakly to the DNA backbone while the carboxylic acids rebel it. As a consequence, the bound DNA complexes get released. The dendron structures and their degradation pathways are represented in Figure 5.2 (a) and (b).

The controlling mechanism was demonstrated for three different configurations. First, the dendrons can be used for complexing the ssDNA building blocks of the DNA origamis, namely the scaffold or the staples, and by this way control the DNA origami structure formation. In addition several dendrons can be used at the same time to complex the scaffold or the staple strands. Consequently, in the second case, both dendrons were used to complex the scaffold requiring multiple trigger signals in order to the DNA origami to form. In the third approach we took advantage of multivalent electrostatic interactions in controlling the triggered release of ready annealed DNA structures.

The control over the DNA origami formation with the dendrons is of great interest for several reasons. To begin with, controlling the self-assembly of nanomaterials with external stimuli such as pH, light, temperature or electric field are important in wide range of applications [140, 141]. Especially interesting scheme would be the controlled delivery of only certain subsets of the staple strands into the origami structure. Therefore, in the presence of a trigger signal, these certain staples (possibly with some functionalization) would anneal into the DNA origami structures. This property could be taken advantage of for example in sensing applications.
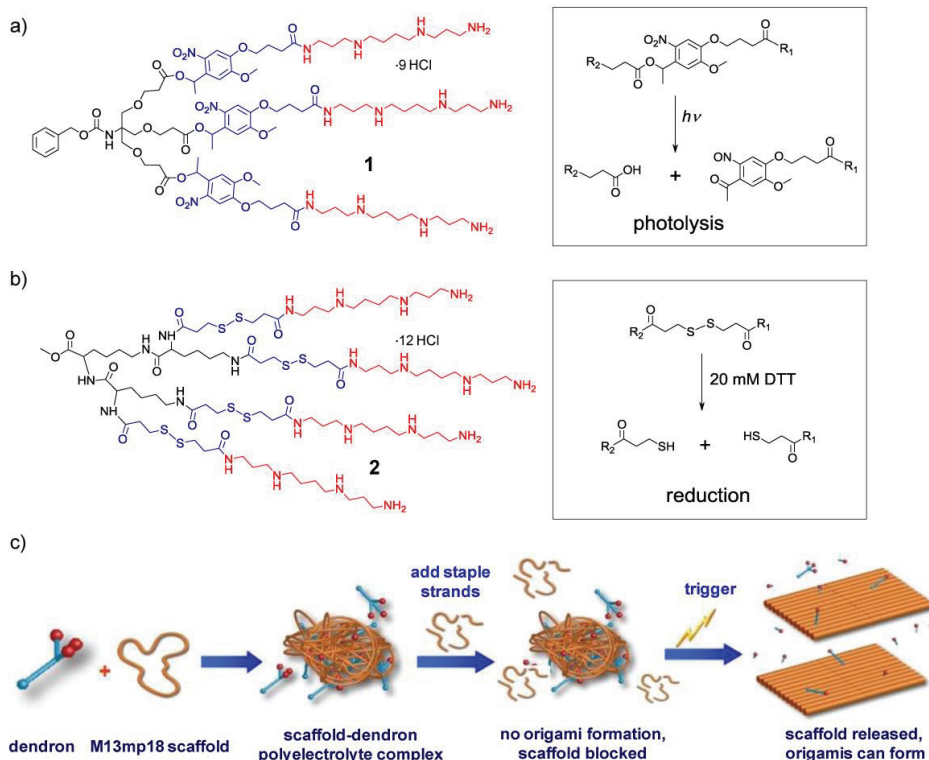
Figure 5.2. Structures of a (a) photodegradable Newkome-type dendron with *o*-nitrobenzyl link-
ers and (b) a polylysine dendron with reduction sensitive linkers used for complex-
ing DNA origamis. The controlling mechanism is represented schematically in (c).
The dendrons form a polyelectrolyte complex with the M13mp18 scaffold which
block DNA origami formation even in the presence of the staple strands. Degrada-
tion of the dendrons with a trigger signal releases the scaffold and enables origami
formation. The operation principle is the same for staple strand complexing. Repro-
duced with permission from Publication III of this thesis.

In the third control scheme the complexing and triggered release of the DNA
origami was presented. Addition of cargo material into DNA origami structures
is straightforward and therefore the origami/dendron -complexes could be used
for non-viral gene therapy. Especially the reducable polylisine dendron DNA
complexes appear very appealing for the purpose due to the possibility to cleave
the disulfide bonds by biological reducing agents, such as glutathione, naturally
present inside cells [142].

5.2 Experimental methods

The controlling experiments were conducted with the same rectangular (72 nm
x 92 nm) DNA origami structures as was used for the SWCNT and for the

AgNP bow-tie antenna assembly experiments. This time, however, the DNA origamis did not contain any modified staple strands. The formation of these DNA origami structures is based on the Watson-Crick base pairing between the scaffolds and the staple strands – a process that we disturbed with the help of the dendrons.

The two degradable dendron types (PLLG1 and SSG2) used in the experiments were introduced in the previous section. The control mechanism taking advantage of these dendrons (Figure 5.2 (a, b)) is illustrated in the schematic Figure 5.2 (c). There the dendrons bind in the M13mp18 scaffold with multivalent electrostatic interactions causing formation of large complexes. In the absence of trigger signals, the scaffold is blocked from base pairing and the DNA origamis are not able to form upon thermal annealing even in the presence of staple strands. However, if a trigger signal (UV-radiation in the case of PLLG1 or DTT in the case of SSG2, respectively) is applied, base pairing is enabled and DNA origami can form again.

The DNA origami components were combined with the dendrons in a 1 x TAE buffered reaction volume (40 mM, Tris 19 mM acetic acid, 1 mM EDTA) containing 12.5 mM magnesium acetate, pH 8.1. NaCl was used in 0.1 M concentration to promote the release of the DNA material from the dendrons. Staple strands were applied in 10 fold excess compared to the scaffold strands to ensure proper folding of the DNA origami structures. The PLLG1 dendron carries a total charge of +9 and SSG2 +12, respectively. For the DNA a molecular weight of $330 \ \text{gmol}^{-1}$ and one negative charge per nucleotide was assumed. The DNA material was combined with the dendrons with a desired dendron to DNA charge ratio, named as the CE-ratio. Several different ratios were probed to find an optimal operation region. The DNA material, for example the M13mp18 scaffold, to be complexed was added to the reaction volume followed by the dendrons with the desired CE-ratio. The material was incubated 5 min before adding the second DNA material which in the case of complexed scaffold was the staple strands. The reaction volume was divided into portions, where the one was treated with a trigger signal and the other one was left untreated as a reference sample. In the case of PLLG1 90 s ($P \approx 9.2 \ \text{mW/cm}^2$, $\lambda \approx 350 \ \text{nm}$) UV-radiation, and in the case of SSG2 20 mM DTT incubation for 1 h was used as trigger signals. Both, triggered and untreated samples were thermally annealed from 90 °C to 20 °C at a rate of 1 °C min^{-1} with 0.1 °C steps.

In the case of controlling the release of ready annealed DNA origami structures, dendrons were added after the thermal anneal with the desired CE-ratio. The DNA origami were prepared in the same reaction buffer as was used for

the scaffold and staple strand complexing with 0.1 M NaCl concentration in the final solution containing the dendrons. Trigger signals were applied in the same manner as explained above.

Experiments were conducted in order to verify that the dendrons indeed prevented DNA origami formation and the thermal annealing did not provide aggregates of origamis. PLLG1 dendron was added to scaffold material with CE=0.4 charge ratio, and in this case UV-treatment was done after thermal annealing to investigate whether any DNA structures had formed. This was followed by an additional annealing step to verify that the origami components had been released by the trigger signal and therefore the structures were able to form again.

The results from the experiments were investigated with atomic force microscopy (AFM). The imaging was conducted in 1 x TAE buffered solutions containing 12.5 mM magnesium acetate in tapping mode on freshly cleaved muscovite mica substrates. The results obtained with AFM were complemented with electrophoretic mobility shift assays (EMSA) with 1 % agarose gel stained with Ethidium Bromide in 1 x TAE buffer without magnesium. The samples were run for 45 min with 90 V applied between the electrodes.

5.3 Results

As can intuitively be expected, the complexing and releasing efficiency depended on the CE-ratio i.e. on the dendron to DNA charge ratio. A significant excess of the dendrons resulted in large aggregates increasingly difficult to degrade with applied trigger signals. On the other hand, a too small ratio could not efficiently prevent the origami formation in untriggered cases. With the triggering conditions used in our experiments, CE-ratio range of 0.4 for PLLG1 and 5.6 for SSG2, respectively, were found to work efficiently.

Atomic force microscope results from the triggered release of the M13mp18 scaffold are presented in Figure 5.3. The upper row of images represent the cases where no trigger signal has been applied ((a) PLLG1, (b) SSG2) and the lower row the triggered cases respectively. The differences between the triggered and untriggered cases are evident. In the cases where no trigger signal had been applied, only aggregates could be found. On the other hand, in the triggered samples, DNA origamis were able to form with high yield. According to the AFM measurements, the dimensions of formed structures match with the design of the long rectangular origami structure. The results implied that dendrons were not only able to bind into the scaffold strands, but also efficiently
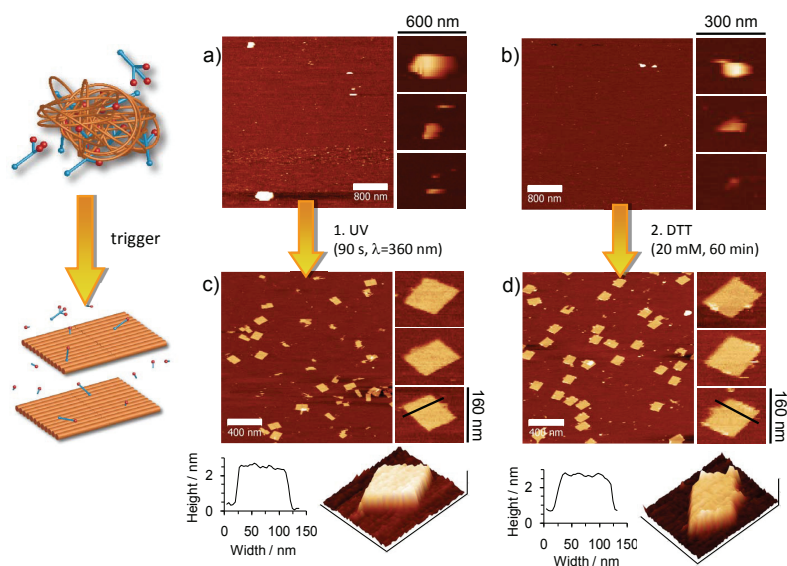
Figure 5.3. Triggered formation of DNA origami structures with the help of degradable PLLG1 and SSG2 dendrons. Combining (a) PLLG1 or (b) SSG2 into a reaction volume with scaffold strands lead into complex formation. The complexes can be opened with the help of trigger signals which enable DNA origami formation with high yield through thermal annealing (c, d). The images (a-c) have been taken with AFM in liquid mode. Reproduced with permission from Publication III of this thesis.

Dendron **1**						+	+	-
Dendron **2**		-	+	+		-	-	-
20 mM DTT		-	+	-		-	-	-
$h\nu$		-	-	-		-	+	-
relative intensity (origami band)		1.00	1.01	0		0	1.04	1.00

Figure 5.4. Agarose gel electrophoresis mobility shift assay (EMSA) experiments on complex formation between the dendrons and the scaffold plasmids. DNA ladder on lanes 1 and 5 as also the pristine DNA origami structures on lanes 2 and 8 operated as reference. In the case of a trigger signal, DNA origami have been able to form with thermal annealing (lanes 3,7). On the other hand, the absence of a trigger signal has lead into aggregates that have not been able to enter the gel (lanes 4 and 6). The lanes 1-4 and 5-8 are from two separate gel experiments. On lanes 3-4 the CE-ratio was 5.6 and on lanes 6-7 CE=0.8. Reproduced with permission from Publication III of this thesis.

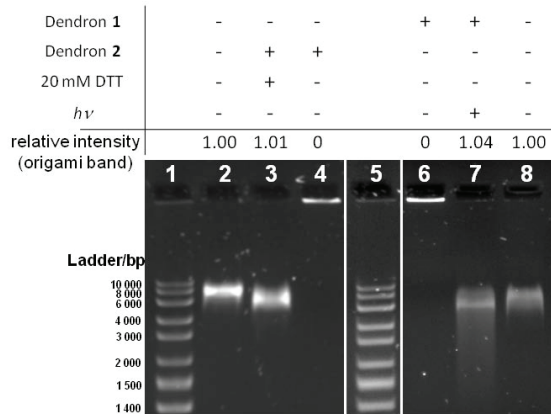prevent thermal annealing of the structures. Moreover the cleaved spermine ligands, released from the dendron structure upon applying the trigger signals, did not disturb base-pairing process and hence origami formation.

The agarose gel electrophoresis mobility shift assay experiments complement the observations made with AFM experiments (Figure 5.4). There the formation of the complexes can be seen as large aggregates that have not even been able to enter the gel in the limits of our running times (lanes 4 and 6). On the other hand, trigger signals have efficiently released the scaffolds and origamis have been able to form with excellent yield (lanes 3 and 7). In the gel the DNA ladder (lanes 1 and 5) and pristine long rectangular DNA origami structures (lanes 2 and 8) operated as references. One can get some quantitative information on the yields by comparing the intensity of the triggered cases to pristine origami bands. In both dendron cases the relative intensities indicate perfect yields.

In the results so far only one type of dendron was used at a time. There are AFM images in Figure 5.5 concerning a case where both PLLG1 and SSG2 dendrons have been applied to the scaffold DNA material at the same time. If only (Figure 5.5 (b)) UV-radiation or (Figure 5.5 (c)) DTT-reduction was applied, DNA origamis were not able to form. The formation of the structures requires both trigger signals (Figure 5.5 (d)). In that case, the structures were able to form in high yields.
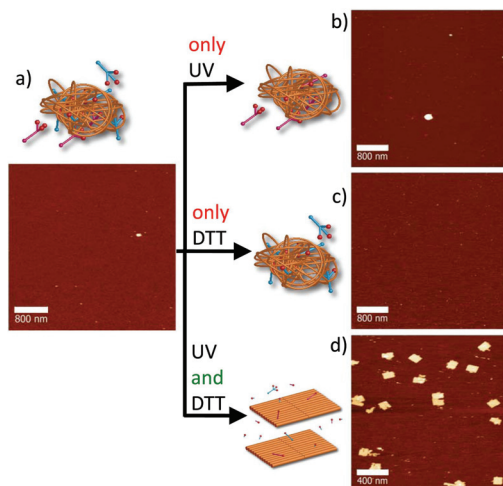
Figure 5.5. The M13mp18 scaffold has formed comlexes with both PLLG1 and SSG2 dendrons (a). If only UV (b) or DTT (c) is applied as the trigger signal, DNA origamis are not able to form even in the presence of staple strands. However if both trigger signals are applied, DNA origami structures can form with thermal anneal with high yield. Reproduced with permission from Publication III of this thesis.

5.4 Conclusions

The results presented in the last section show the efficiency of using dendrons for controlled formation of the DNA origami structures with the help of external trigger signals. When the dendrons were applied to the scaffold strands, DNA origamis were able to form with thermal annealing only in the case when a trigger signal was applied. Absence of control signals led into aggregates of DNA/dendron material preventing base pairing, and hence the DNA origamis were not able to form even in the presence of staple strands. The additional experiments mentioned in the last section proved that thermal annealing of the scaffold/dendron complexes in the presence of the staple strands did not produce origami structures. Triggering the annealed complexes followed by an additional annealing step did, however, produce origamis again with high yields.

Although the method operated already with high yields, there would still be room for improvements. One factor that could be optimized is the dendron type used for complexing the DNA. The dendrons bind to the DNA strands with multivalent electrostatic interactions. Therefore the size i.e. the dendron generation has an impact on the strength of dendron to DNA binding. In addition one can improve the approach by optimizing the reaction conditions. We had a fixed power UV-source and perhaps higher powers could enhance the release mechanism for the PLLG1 dendron. With these optimizations one could be able

to get rid of only partially formed origami structures still visible especially in the case of PLLG1 dendrons (Figure 5.3 (c)).

The results presented in the last section considered only the case of triggered release of the M13mp18 scaffolds. However, as was mentioned in the introduction of this chapter, the dendrons can be used to complex staple strands as well as ready annealed DNA origami structures. Experiments were conducted on these matters with both dendron types and the results verified our claims. The case of dendrons bound to the staple strands operated equally well with high yields as the case with dendrons in the scaffolds. Moreover, both dendron types were able to efficiently form complexes with annealed DNA origami structures which then got released with trigger signals in high yields.

6. Field-induced nanolithography

In Chapters 3 and 4 methods for positioning nanoparticles with nanometer precision with the DNA origami method was presented. There single walled carbon nanotube and silver nanoparticle patterns were prepared on the origami substrates, in the first case with streptavidin-biotin interaction, and in the second with ssDNA strand hybridization. In the previous chapter, a method for controlling the formation of the DNA origami substrate was introduced. In this chapter a general technique, based on electric fields, is presented for patterning arrays of nanoparticles. Although the method was demonstrated with semiconductor quantum dots (QDs), it can be extended to other nanoparticles and structures such as the DNA origamis.

6.1   Introduction

Nanoimprint lithography (NIL) is a large scale high-precision method for pattern transfer on target substrates by way of pre-patterned moulds. Typically the substrate contains a resist layer, which can be cured thermally [143] or with UV-radiation [144], although methods with no resist have also been reported [145, 146]. The operation principle is illustrated in the schematic Figure 6.1. The pattern in the mould is transferred to the substrate by mechanical contact accompanied by some method driving the class transition of the resist. Although large throughputs and precision can be achieved, the approach has one major drawback – the mold itself. Namely, changing the pattern means necessity for preparing a new mould. Microcontact printing [148], a tool similar to the NIL-method using polydimethylsiloxane (PDMS) stamps, suffers from the same issue.

In Publication IV of this thesis, a novel approach to the nanoimprint lithography was presented – named as the field-induced nanolithography (FINAL). The method is illustrated in Figure 6.2. A master stamp, having two rows of finger-
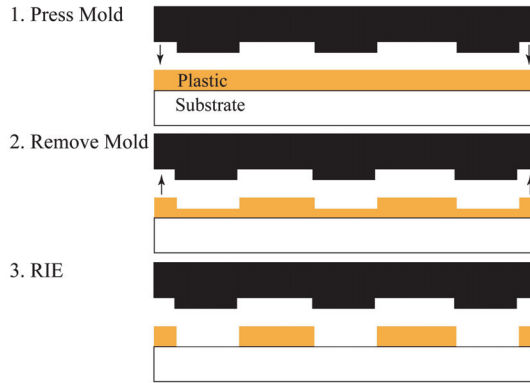
Figure 6.1. A Schematic figure illustrating nanoimprint lithography process steps. A mould is used for pattern transfer on target substrates. After pattern transfer (step 1.), the resist is turned into glass, e.g. with UV-radiation, and the mould is removed (step 2). Excess resist is removed from patterned areas, usually with reactive ion etching (step. 3). The procedure can be further continued with standard lithographic steps, such as etching and metal deposition. The method can be used for patterning features with large scale and high-precision [143, 147].

tip electrodes facing each others, was used for preparing a desired pattern of nanoparticles. Although the operation principle was demonstrated with a single row of fingertip electrode pairs, a 2-D matrix of them would be as straightforward to fabricate. A sinusoidal voltage between the electrodes causes large electric field gradients in gaps located between the fingertip pairs (Figure 6.2 (a)), which can be used for trapping polarizable nanoparticles – method known as dielectrophoresis (DEP) [149]. Figures 6.2 (b) and (c) illustrate this process. There the initially randomly moving nanoparticles (b) get trapped between the electrodes that have been connected to a voltage source (c). A transparent target substrate was brought mechanically into contact with the stamp (Figure 6.1 (d)) and as a result: the trapped nanoparticle pattern was transferred from the stamp into the target substrate (Figure 6.1 (e)).

There are several advantages in the FINAL-approach over the existing methods, such as fluidics [150], magnetic fields [150], electrophoresis [151, 152], light-induced electrophoresis [153], dielectrohporesis [154], light-induced dielectrophoresis [155], optical tweezers [156], and surface plasmon resonance [157], for manipulation of nanoparticles. Some of these methods offer high spatial resolution in manipulation [151, 156, 158, 159], but are limited in throughput. On the other hand, some methods give high throughput but lack in resolution [153, 160] or the nanoparticles are bound to the master chip [150, 154, 157, 161]. The field-induced nanolithography method addresses to all of these issues by offering high resolution limited only by the lithographic fabrication of the master stamp electrodes. The master stamp with a 2-D matrix pattern
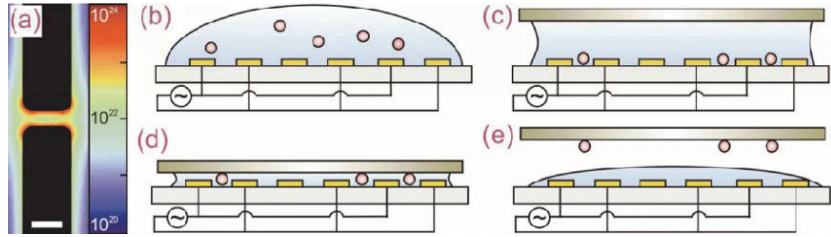
Figure 6.2. A schematic presentation of the field-induced nanolithography approach. The method takes advantage of strong electric field gradients generated between fingertip electrodes patterned on a master stamp (a,b). In (a) there is a finite elements method (FEM) simulation demonstrating the electric fields confined in a gap between two fingertips. The strong field gradients can be used to trap nanoparticles (c) – a process known as dielectrophoresis. After preparation of the desired particle pattern on the stamp, a target substrate was brought into mechanical contact with it (d) for the pattern transfer (e). Reproduced with permission from Publication IV of this thesis.

of electrodes is universal meaning that arbitrary patterns of nanoparticles can be formed on the stamp, which can then subsequentially be transferred on the target substrate. Moreover the stamp is reusable and therefore, in addition to high resolution, the method provides high throughput. As a contrast to the electrophoretic approaches, the particles need not to be charged. The only requirement is that the particles are polarizable. The dielectropheric approach is also non-destructive, offering possibility to operate with delicate nanoparticles such as DNA [82] and proteins [162].

The FINAL method is represented in more detail in the following sections. The method lies heavily on dielectrophoresis and therefore some background information is given on the subject before going into actual experimental details. In Publication IV of this thesis, the system was demonstrated for quantum dots. As these are extremely fascinating zero dimensional objects with unique optical and electrical properties, a brief introduction to quantum dots is also given.

6.1.1   Quantum dots

The dimensionality of a system can be determined based on some physical behaviour of the system. For example, the dimensionality can be related to the electron mean-free path length Λ. Then the system is said to have reduced dimensionality if in some orthogonal direction the mean-free path length is determined by boundary scattering instead of some intrinsic scattering mechanism [163]. Another approach for determining the dimensionality is to relate the structure dimension to the exciton Bohr-radius
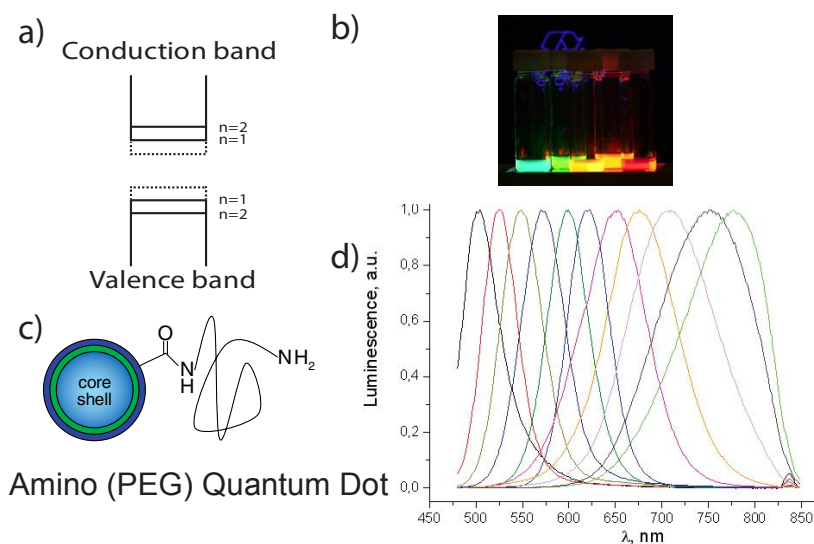
Figure 6.3. Due to quantum confinement resulting from reduced dimensionality, the electronic properties of the quantum dots (QDs) differ from their bulk material values. As a result from this confinement, the conduction and valence bands split into new levels. This is illustrated in (a), where the dashed line represents the bulk material case. The optical properties of QDs are dependent on the particle size and by adjusting this parameter, practically the whole visible spectrum can be covered. The emission properties of quantum dots of different sizes are illustrated in (b,d). In order to enhance the optical properties of the QDs, they are often passivated with a thin shell. This is illustrated in (c) by a green shell surrounding the core. In addition, ligands can be added to incorporate functional groups for example for biomolecule targeting (c). Figure (c) Copyright ©2013 Life Technologies Corporation. Used under permission, www.lifetechnologies.com.

$$a_0^* = \frac{4\pi\epsilon\epsilon_0\hbar^2}{\mu e^2}, \qquad (6.1)$$

where ϵ is the dielectric constant of the material, $\hbar$ is the Planc's constant, e the elemental charge and $\mu = m_e^{*-1} + m_h^{*-1}$ is the reduced mass of the exciton composed of the electron and hole effective masses. In this case the system is said to posses reduced dimensionality if in some direction the size of the system $\{L_i; \quad i = (x,y,z)\}$ is less than the Bohr-radius of the exciton i.e. $L_i \leq a_0^*$ [163].

Quantum dots are said to be zero-dimensional systems because the electron wave function is confined in all three dimensions. Two distinct regimes for confinement, namely a weak and a strong confinement regimes, can be defined depending on the relation between the system size (here the radius of the particle R) and the Mott-Wannier exciton Bohr radius [164]. In the strong confinement regime $R/a_0^* \leq 2$, the motion of the exciton is hindered so much that the situation reduces into particle-in-a-box problem, with energy levels for a particle of mass m according to

$$\varepsilon_n = -\frac{\hbar^2 \pi^2 n^2}{2mR^2}. \qquad (n = 1,2,\cdots) \qquad (6.2)$$

This leads to splitting of the energy bands giving rise to atomic-like energy levels as illustrated in Figure 6.3 (a). This is the reason why QDs are sometimes referred as artificial atoms. In the n=1 state the exciton has energy according to [163]

$$\varepsilon \simeq \frac{\hbar^2}{2\mu}\frac{\pi^2}{R^2} - \frac{1.8e^2}{4\pi\epsilon\epsilon_0 R}. \qquad (6.3)$$

Eventually the creation of an electron-hole pair leads to recombination and emission of a photon. When the excitation energy has been obtained from a photon, the emission by the QD is called photoluminescence. As an important consequence from quantum confinement, the band gap of the QDs is dependent in addition to material composition on the size of the dot. This can be seen also from Equation 6.3 for the exciton (1s state) binding energy. Therefore the band gap can be tuned by tuning the particle size. By this way one can tune the emission wavelength of the QD, and practically the whole visible spectrum can be covered (Figure 6.3 (b, d)). Moreover, recently a method for post-fabrication tuning of the QD emission wavelength using surface plasmon resonance was reported [165].

Due to a large surface-to-volume ratio in the quantum dots, the surface defect states play a major negative role in the properties of the quantum dots [166]. As an example, roughly 15 % of the atoms in a 5 nm CdS QD lie on the dot's
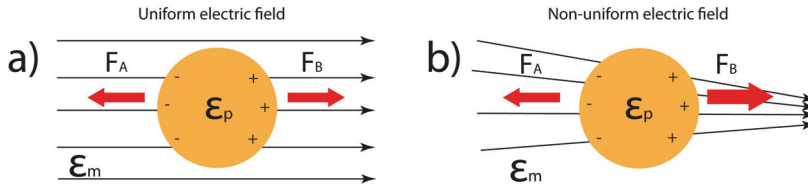
Figure 6.4. As a response to an electric field, a dielectric particle (permittivity ϵ_p) in a dielectric medium (ϵ_m) gets polarized. In the case of a uniform electric field (a) the forces exerted on the particle, although being opposite in direction, are of the same magnitude. Therefore the particle does not feel any net force due to the electric field. If the electric field is non-uniform (b) the forces on the opposite sides are no longer same in magnitude, and as a consequence, a net force is exerted to the particle.

surface [167]. Therefore thin surface passivation layers, organic or inorganic, are used for getting rid of surface states which are efficient traps for electrons, holes or excitons. The passivation layer forms also a potential barrier for the excitons leading to more photostable QDs [168].

The quantum dots (bought from Invitrogen) used in our experiments had CdSe core with ZnS shell, Figure 6.3 (c). The lattice parameter mismatch for the pair is 10.6 %, which is below 12 % – a value that should not be exceeded in order to avoid strain and misfit dislocations [169]. Moreover, the ZnS has significantly larger band gap (3.6 eV) than CdSe (1.73 eV) [170] providing potential barriers for the excitons. In addition to the passivation layer, ligands can be added to the QDs for coupling reactions. In our case the QDs had amino-PEG (polyethylene glycol) coating.

6.1.2 Dielectrophoresis

Dielectrophoresis (DEP) is a phenomenon of translational motion caused by forces exerted on particles by a non-uniform electric field (E-field) [149]. Distinguished from electrophoresis, the particles need not to be charged. The only requirement is that the particles are polarizable. A schematic Figure 6.4 presents the principle of DEP. A dielectric particle in a host medium gets polarized by an external electric field. In the case of a uniform field (Figure 6.4 (a)), the forces on the opposite sides of the particle cancel each other. On the other hand, if the E-field is not uniform, different sides of the particle experience forces of different magnitude. This is caused by differences in the density of the electric field, and as a consequence the particle experiences a net force (Figure 6.4 (b)).

The dielectrophoretic force exerted on a polarized particle in an external electric field can be obtained from the analysis of a point dipole. The sum of the Coulombic forces on the opposite charges is $\vec{F} = q\vec{E}(r + \vec{d}) - q\vec{E}(\vec{r})$, where $\vec{d}$ is

the separation between the dipole charges (q and -q). Supposing an infinitesimally small dipole, the first term can be expanded into Taylor's series and by this way one obtains a solution for the force

$$\vec{F} = q\vec{d} \cdot \vec{\nabla}\vec{E} + \cdots. \tag{6.4}$$

Keeping only the linear term, one gets

$$\vec{F} = (\vec{p} \cdot \vec{\nabla})\vec{E}, \tag{6.5}$$

where $\vec{p} = q\vec{d}$ is the dipole moment.

When a dielectric particle is immersed in a dielectric medium, the dipole moment in Equation 6.5 can be replaced with an effective dipole moment [171], that is proportional to the electric field

$$\vec{p} = \alpha\vec{E}, \tag{6.6}$$

where α is the effective polarizability

$$\alpha = 3V\epsilon_m Re[K]. \tag{6.7}$$

The approach of replacing the dipole moment with an effective one is named as the effective moment method [172]. The effective polarizability is dependent, in addition to the particle volume V and the dielectric constant of the medium, on the so called Clausius-Mosotti factor defined as [173]

$$K = \frac{1}{3} \times \frac{\underline{\epsilon_p} - \underline{\epsilon_m}}{\underline{\epsilon_m} + A(\underline{\epsilon_p} - \underline{\epsilon_m})}. \tag{6.8}$$

Here A is a geometrical factor and for example for a sphere A = $\frac{1}{3}$. The complex permittivity $\underline{\epsilon_{m,p}}$, with subscripts m for the medium and p for the particle, is defined as

$$\underline{\epsilon_{m,p}} = \epsilon_{m,p} - i\frac{\sigma_{m,p}}{\omega}. \tag{6.9}$$

There $\sigma_{m,p}$ is the conductivity of the medium and the particle, respectively, and ω is the angular frequency of the electric field. Combining Equations 6.5, 6.6 and 6.7 and taking the time averaged value, one gets the following expression for the time averaged dielectrophoretic force on an isotropic homogenous spherical particle in a non-uniform electric field [171]

$$< \vec{F}_{DEP} >= 2\pi\epsilon_m V Re[K(\omega)]\vec{\nabla}(\vec{E}_{RMS}^2), \tag{6.10}$$

where RMS means the root-mean-square value of the electric field with the assumption of a sinusoidal signal.

Couple of important remarks on the derivation of the dielectrophoretic force should be made. First, in the derivation the particle was approximated as an infinitesimally small dipole, which is called the dielectrophoretic approximation. This assumption is of course not true with objects of finite size. However, if the scale of the electric field non-uniformity is large compared to the particle size, the approximation is valid and can usually be used with situations, for example, where the electrodes are large compared to the particles. Otherwise multiple terms in the Taylor's series expansion should be taken into account [172, 174].

Secondly, in Equation 6.8 there is an assumption of lossless particles and medium with complex permittivity given by Equation 6.9. A more general form of the representation for Equation 6.9 would be [171]

$$\underline{\epsilon(\omega)} = \epsilon^{'}(\omega) - i(\epsilon^{''}(\omega) + \frac{\sigma}{\omega}), \tag{6.11}$$

where $\epsilon^{''}(\omega)$ represents the dielectric loss and σ/ω the low-frequency ohmic loss. In these situations, in order the effective dipole moment method to be valid, the form 6.11 should be used and the effective dipole moment (Equations 6.6, 6.7) should be somewhat modified [171] or one should use a more general Maxwell's tensor method [175]. However, quite often the dielectric loss term is significantly smaller than the conductivity term and therefore can be neglected.

Despite of its limitations, the effective moment method provides insight into the physics of the dielectrophoresis. One can readily make following observations from Equation 6.10.

1. The force is linearly dependent on the particle volume. Therefore the smaller the particle, the smaller the force.

2. The force does not depend on the electric field orientation. Although the direction of the electric field vector changes, the direction of the DEP force is always the same, and therefore time averaged values can be used for AC-signals. Moreover it does not matter whether the E-field is AC or DC of origin. The use of AC-fields assumes that the polarization response of the particles is immediate.

3. The force is dependent on the magnitude and sign of the Clausius-Mosotti factor.
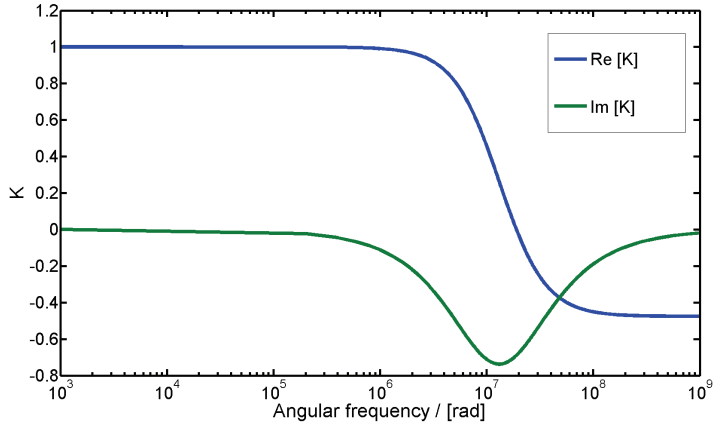
Figure 6.5. The real and imaginary parts of the Clausius-Mosotti factor as a function of angular frequency for a dielectric latex nanoparticle.

From the point three of the list, one can derive two distinct types of dielectrophoresis. As the real part of the Clausius-Mosotti factor can get values from $-0.5 \leq K \leq 1$, then when the constant is positive, the particle gets pushed towards the electric field maxima. On the other hand, when the constant has a negative value, the particle drifts towards the E-field minima. These two cases are named as the positive and negative DEP. In Figure 6.5, the real part of the Clausius-Mosotti factor for a dielectric sphere is plotted. As can be observed, the sign of the factor can be changed by changing the E-field frequency. The relative magnitudes of the permittivities of the medium and the particle influence also the type of DEP through the Clausius-Mosotti factor.

The particles embedded in a dielectric volume experience also other forces that compete with the DEP-force [176]. One of these is caused by random thermal motion of the particles named as Brownian motion, the maximum value of which for a spherical particle of radius R can be expressed with Equation [177]

$$F_{thermal} \approx \frac{k_B T}{2R},$$
(6.12)

where k_B is the Boltzmann constant and T the temperature. An important observation from the equation is the inverse dependence on the particle radius. Due to this dependency, the force plays a major role with nanosized particles. In addition to the thermal motion, Joule heating of the medium caused by the electrodes induces the motion of the fluid imposing forces on the particles. Moreover, a tangential electric field component on the electric double-layer formed on the electrode-electrolyte interface causes steady motion of the solution hindering the DEP-effect [176]. However the competing forces can be won with
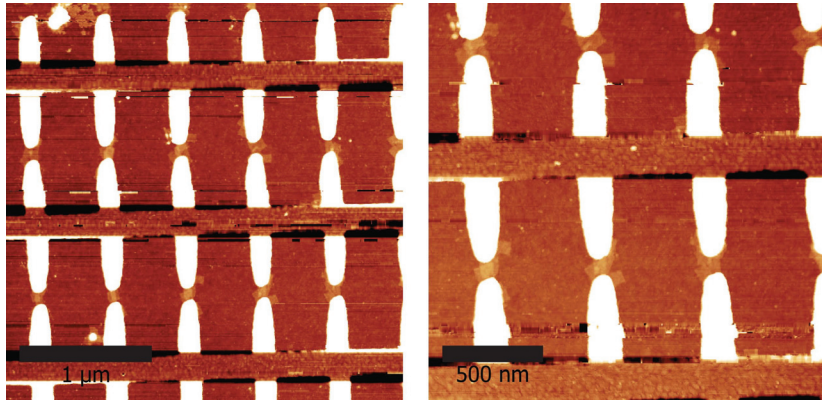
Figure 6.6. Atomic force microscope images of DEP of rectangular DNA origamis on large scale. The DNA origami have been trapped in the gaps (gap size roughly 50 nm) between two fingertip electrodes.

nanoelectrodes creating large electric field gradients. As an example: we have trapped rectangular DNA origami of 92 nm x 72 nm size dielectrophoretically on large scale between fingertip electrodes in a matrix (Figure 6.6).

6.2   The FINAL-method

The FINAL-method was introduced in Section 6.1 and in Figure 6.2. Now, in what follows, the experimental details concerning the approach are presented. A Si/Si$_3$N$_4$ substrate was patterned with standard electron beam lithography and was used as the master stamp. The structure consisted of two parallel plates with fingertip electrodes facing each other. The electrodes were 170 nm wide with a 50 nm gap between the fingertips. The electrodes were made out of Au (15 nm) with a 2 nm titanium adhesive layer, both prepared with e-beam evaporation. Before trapping the QDs through dielectrophoresis, the master stamp was treated with an adhesion block chemical (SuperBlock blockin buffer in PBS, Pierce) in order to prevent non-specific binding of the nanoparticles on the stamp. In the case of the transparent target substrate, efficient binding of QDs was desired and therefore the surface was treated with an adhesion promoter poly(diallyldimethylammonium chloride)(PDACMAC). Some different options for adhesion promoter was tested, such as poly-L-lysine, however the chemical chosen gave the best results. The imaging of the results was conducted with a confocal microscope.

The pattern transfer was conducted on the course of the following steps. First, a sinusoidal voltage with 3.5 V amplitude was applied between the two parallel plates. This voltage was kept on for the rest of the process. Next, a drop of
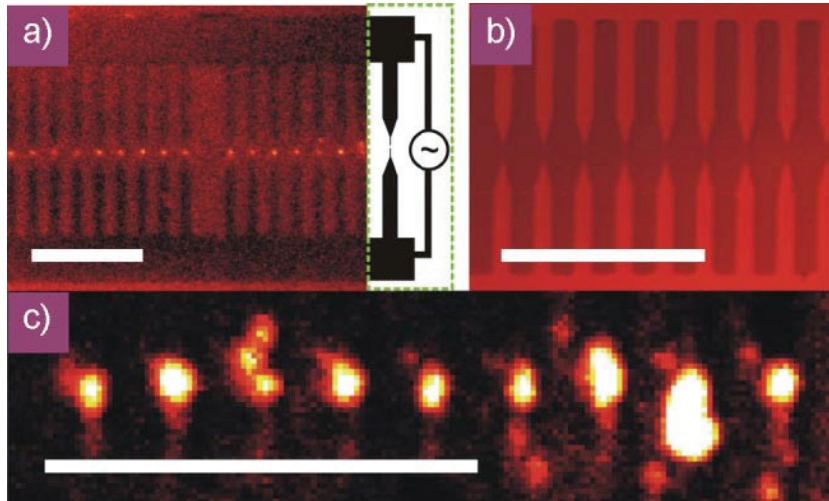
Figure 6.7. Quantum dots (QDs) were dielectrophoretically trapped between fingertip electrodes, patterned on a master stamp, through an AC-voltage signal. The trapping process was monitored in real time with a confocal microscope (a). After the pattern transfer process, the stamp appeared clean from QDs and ready to be used for further patterning (b). The trapped pattern of quantum dots was transferred with high fidelity on a target substrate (c). The scale bars in the images are 50 μm. Reproduced with permission from Publication IV of this thesis.

quantum dots (80 nM in water, emission wavelength $\lambda = 655$ nm) was injected on the substrate followed by a 10 min incubation time to ensure efficient dielectrophoretic trapping of the quantum dots. The process was however very rapid, and one could observe build up of fluorescence from the electrode gaps nearly instantaneously after injecting the QD solution. In the second step, excess quantum dot solution was removed by rinsing the master stamp surface several times with water. This procedure increased the signal-to-noise ratio (the intensity ratio between the trapping location and the background on the target plate) 50-fold compared to a reference sample without rinsing. In the third step the target plate was brought into contact with the liquid on top of the stamp, followed by bringing the substrate into mechanical contact with the stamp. As a last step the stamp and the target substrates were separated, the stamp was washed with water and dried with nitrogen, while the target substrate was dried with nitrogen respectively.

Confocal microscope imaging was conducted during the DEP-process through the substrate. As can be observed from Figure 6.7 (a), the QDs were efficiently trapped between the electrodes. If the voltage was switched off, the QDs diffused very rapidly from the gaps due to brownian motion. After setting up the voltage again, the same pattern of quantum dots as in (a) was readily obtained. Finite elements method -studies conducted on the dielectrophoresis of 10 nm

QDs, with polarizabilites obtained from [156], complement the experimental observations: the DEP force $F_{DEP} = 1.3x10^{-10}$ N was found to be orders of magnitude larger compared to the brownian motion $F_B = 4x10^{-13}$ N (Equation 6.12). After the pattern transfer process the master stamp with the electrodes was found to be clean from QDs Figure 6.7 (b) demonstrating the possibility to reuse the stamp. On the other hand, the pattern transfer process produced the trapped QD pattern on the target plate with high fidelity as represented in Figure 6.7 (c).

6.3   Conclusions

The work was conducted to demonstrate the capacity of the FINAL method to produce nanoparticle patterns with high throughput and precision. As the results imply, the designed quantum dot pattern was efficiently transported on the target substrate surface, even without any major process optimization. Moreover, after the deposition process, the master stamp appeared clean from quantum dots and ready for further pattern transfers. The approach is extremely versatile and can be used to variety of nanoparticles, the only requirement being: the particle has to be polarizable. As the target substrate was brought into mechanical contact with the stamp by hand, preparing a more sophisticated micromechanical system would already be a major improvement. In addition, by varying the gap size, QD concentration and trapping time, the amount of nanoparticles trapped between the electrodes could be controlled.

7. Assembling gold nanoparticle chains using AC electric fields

In the previous chapter, dielectrophoresis was used as a tool for developing a new nanoimprint technique named field-induced nanoimprint lithography. There the dielectrophoretic-driven process was demonstrated with semiconducting quantum dots. However, as was presented in the introduction part of that chapter, dielectrophoresis can be used for polarizable objects whether they are charged or not. Therefore the theories introduced there apply to charged particles such as gold nanoparticles (AuNPs). In this chapter the dielectrophoresis is harnessed for assembling AuNP chains between both micro- and nanoelectrode gaps. The assembly process was demonstrated in Publication V of this thesis.

Noble metal nanoparticles have been harnessed for sensing over many years [178]. Films of such particles, with insulating layers of organic molecules (metal-insulator-metal, MIME), for sensing applications were also introduced a decade ago [179]. In Publication V of this thesis and in what follows the gold nanoparticle chains are demonstrated being capable of operating as efficient sensors, miniturizing the noble-metal sensor from 2-D to 1-D. Although the electrical properties of such chains have been widely studied [180–182], the sensing prospect has been addressed very rarely [183, 184].

7.1 Experimental details and results

The AuNP chain formation experiments were conducted with three different sets of electrodes, two of them being microsized with 1 μm and with 10 μm gaps. In addition, an array of nanoelectrodes with gap size varying from 40-100 nm was tested. The microelectrodes were patterned in the IPHT (Institut für Photonische Tegnologien), Jena, Germany with standard photolithographic techniques on silicon/silicon oxide substrates. The electrodes were made from 100 nm sputtered Au. The 50 nm tall (with 2 nm Ti adhesion layer) nanolectrodes,
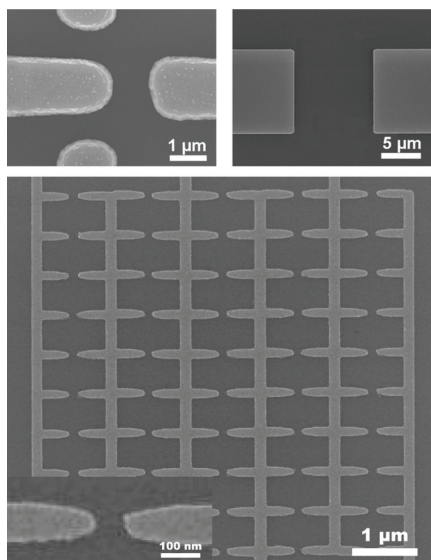
Figure 7.1. Scanning electron microscope images about three different sets of electrodes used in the experiments. In the round electrode configuration (top left) the gap in the structure was 1 μm, and in the square electrode (top right) 10 μm. In addition, nanoelectrodes with gap size varying from 40-100 nm was tested. Reproduced with permission from Publication V of this thesis.

both metals thermally evaporated, were fabricated with e-beam lithography in Aalto University, Espoo, Finland on silicon/silicon oxide substrates. There are images of the electrodes in Figure 7.1. The gold nanoparticles for the experiments were bought from BBI (British BioCell) with diameters 5 nm (1×10^{13} P/ml), 15 nm (1.4×10^{12} P/ml), 30 nm (2×10^{11} P/ml)and 60 nm (2.6×10^{10} P/ml). The particles were used in the experiments with the same concentrations as they were received.

The trapping and the formation of the AuNPs chains through dielectrophoresis was performed with a signal generator with voltage varying from 0.7 V to 2.5 V and frequency from 1 kHz to 1 MHz. The values depended on the electrode structure type as well as on the particle size. Figure 7.2 presents the chain formation in the case of the square electrodes. The process starts from the areas of largest field gradients and the chains appear to grow according to the electric field lines. With this particular electrode type the voltage had to be slowly ramped down in order to obtain constant field strength. This procedure led into more well defined particle chains. The step was not necessary for the 1 μm gap electrodes nor for the nanogaps. The frequency used in the case of Figure 7.2 was 1 kHz with voltage ramped from 2.5 V to 1.0 V during the 8 min trapping time.

The formation of the AuNP chains was monitored in real time with an oscil-
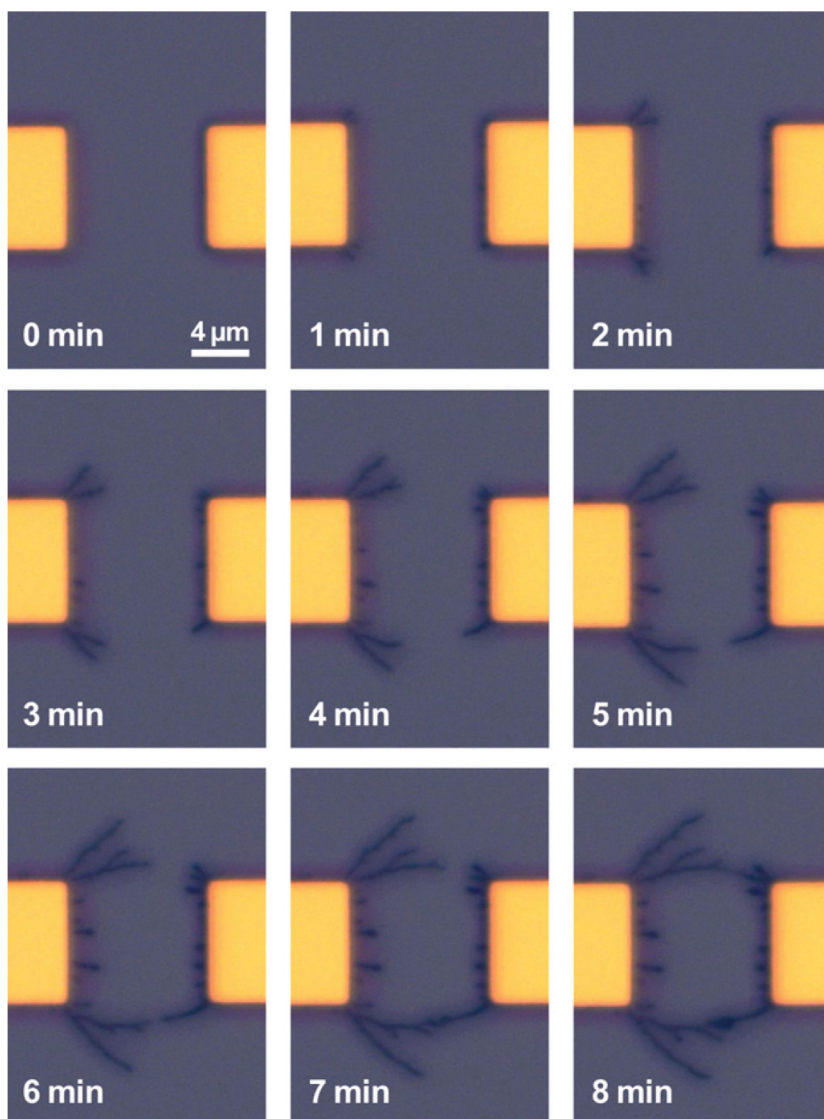
Figure 7.2. Formation of the AuNP (30 nm in diameter) chains with an AC-voltage signal (1 kHz). The voltage has been successively ramped down during the process from 2.5 V to 1.0 V. The nanoparticles in water have been applied to the electrodes and the chain formation begins immediately after applying voltage between the electrodes. The images have been obtained with an optical microscope. A more detailed scanning electron microscope analysis revealed that the chains of particles were actually melt into a continuous wire. Reproduced with permission from Publication V of this thesis.

loscope by measuring the voltage across a 100 ohm resistor put in series with the electrode gap. The chain growing could be observed as an increase in the voltage across the resistor. At the point where the chains growing from opposite ends of the gap met to form a bridge, the measured voltage increased rapidly (Figure 7.3). This was a consequence from the formation of a conduction channel between the electrodes and therefore from the increase of current flowing through the resistor. There appeared also to be a threshold value for the voltage and values below this threshold did not lead into chain formation (Figure 7.3). The monitoring method appeared to work efficiently with all the electrode types and interestingly, this increase in conduction could be used for automation of the process.

The sensor operation of the AuNP chains was tested with 10 mM 1-mercapto-6-hexanol (MCH) target molecule as the substance to be detected. End-point and real-time measurements were conducted with both the square and round electrodes. The detected substance bound to the AuNP chains with strong thiol bonds which caused a change in resistance. In the case of end-point measurements, the resistance between the gaps was measured before and after analyte exposure in air. According to the measurements, the resistance increased about 10 % in the case of the 10 μm gap and up to 2000 times for the 1 μm gap.

In addition to end-point sensing experiments, real-time measurements of 10 mM MCH target molecule binding were conducted with the round electrodes having the 1 μm gap. Figure 7.4 presents results from such a measurement. As can be seen from the figure, the target molecule could be sensed in real time as an increase in resistance and hence decrease in the conductance. However, it was observed that the real time monitoring worked only with chains having lower resistance than the surrounding media. Otherwise the current flew through the surrounding media instead of the particle chains and hence instead a raise of current with high resistance chains was observed.

The possibility of assembly AuNP chains in the nanoscale was demonstrated with an array of nanoelectrodes arranged parallel to form in total 50 gaps ranging from 40-100 nm. The Figure 7.5 presents results from the chain formation with 30 nm AuNPs (a) and with 15 nm AuNPs (b). As can be observed the chains formed with high yields. The resistance was measured to be 3 MΩ for the 30 nm particles and 30 MΩ for the 15 nm case, respectively. These values indicate non-fused particle chains as can be observed also from the scanning electron microscope images.
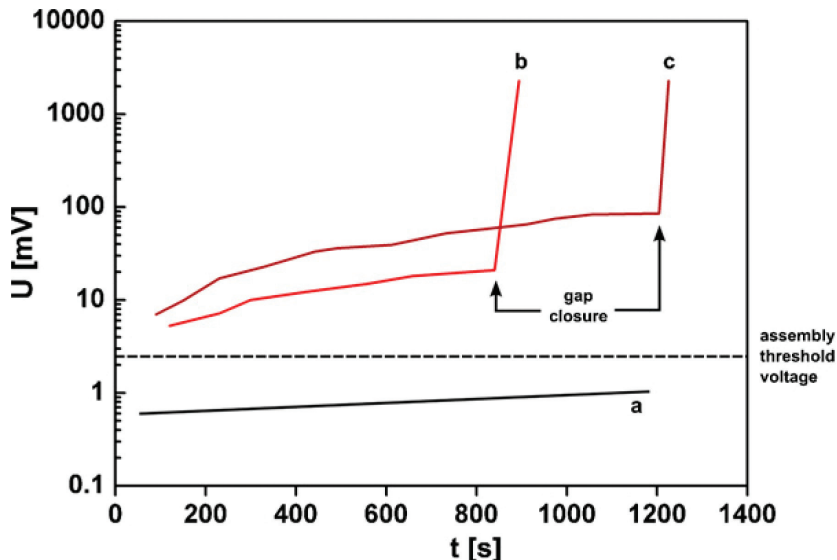
Figure 7.3. The particle chain formation between the electrodes could be monitored in real time. When a chain of particles formed a complete bridge between the electrodes, the voltage started to increase rapidly (points b and c). The two measurements have been done in identical conditions, consequently the time particle chains are assembled until connection cannot be predicted. The chain formation required magnitudes above a threshold value in order for the chain formation to start. In the case of having voltages below the threshold value (point a), no voltage increase could be observed. Reproduced with permission from Publication V of this thesis.

7.2 Conclusions

The results verified that AuNP chains could be assembled with the help of dielectrophoresis in both cases, with the microelectrodes as well as with the nanoelectrodes, in high yield. In the case of large 10 μm gap electrodes, the voltage used for trapping had to be slowly ramped down. In addition, the trapping process had to be stopped immediately after bridge formation due to the fact that with these electrodes the particle chains tended to melt into fused wires. This led into high currents due to short cut electrodes which could immediately break the formed bridges. This was not an issue with the round electrodes with the 1 μm gap and there the thickness of the particle chains could be controlled by trapping time. In the case of nanoelectrodes caution had to be taken by using lower voltage values than with microelectrodes in order not to damage nanoelectrodes. In addition, prolonged trapping times could lead to damaged electrodes.

The experiments revealed also that the AuNP chains could be used for sensing applications for both end-point and real time measurements. Best performance for the end-point measurements was obtained when non-fused particle chains
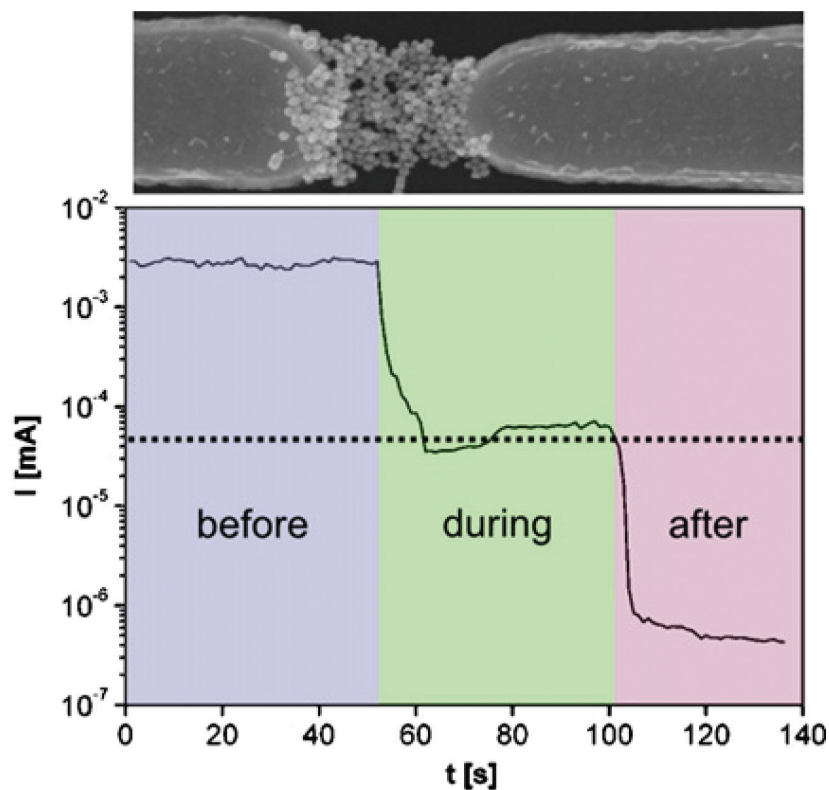
Figure 7.4. Scanning electrode microscope image reveals efficient trapping of AuNPs in a 1 μm gap between the round microelectrodes. The resistance between the electrodes, having the particle chains as a bridge across the electrode gap, was monitored in real time upon injection of 1-mercapto-6-hexanol target molecule. The change in conduction of the chain channel upon binding of the target molecule is evident. Reproduced with permission from Publication V of this thesis.
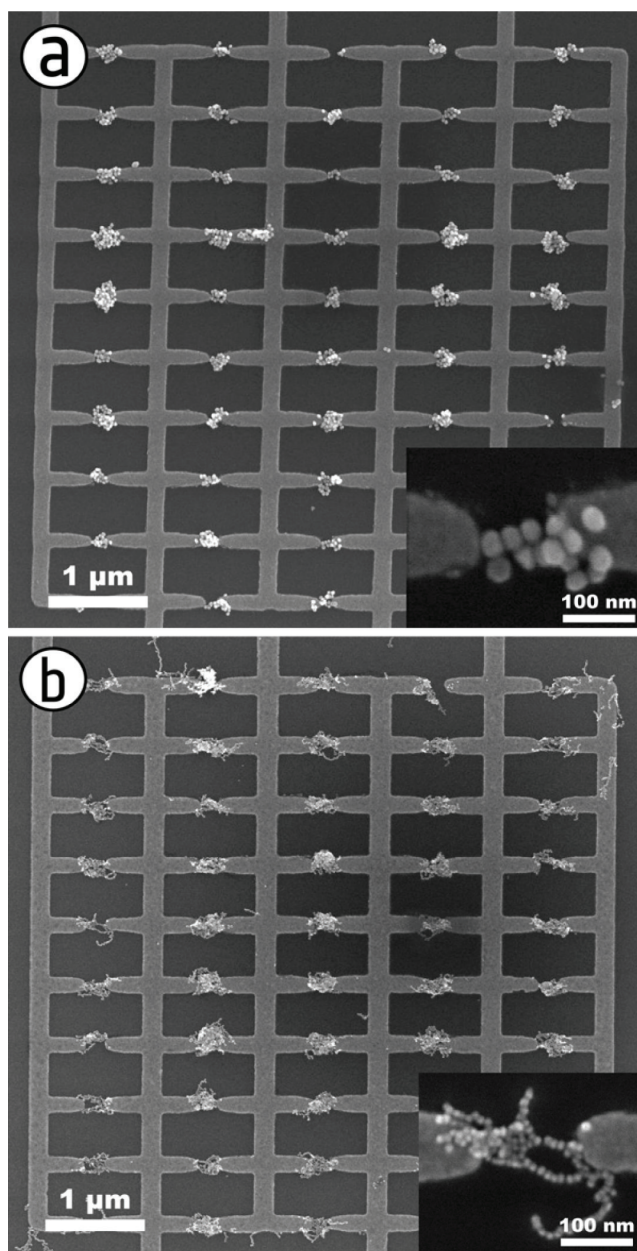
Figure 7.5. Scanning electron microscope images of dielectrophoretically trapped AuNPs ((a) 30 nm and (b) 15 nm in diameter) with nanoelectrodes. Reproduced with permission from Publication V of this thesis.

were used. These were obtained mainly with the round electrodes. Then the resistance grew up roughly 2000 times larger compared to resistance measured before applying the target molecule. The real-time measurements required a particle chain lower in resistance compared to the surrounding medium to operate. But in that case the change upon target molecule binding could clearly be seen.

8. Conclusions

In this thesis it was demonstrated that the DNA origami method provides a powerful tool for assembling complicated structures at the nanoscale with nanometer range precision. The presented method for assembling and aligning single-walled carbon nanotubes offered a means for efficient electrical contact forming as well as a platform that could be turned into a sensor after attachment of other functional nanoparticles. Moreover, a crossed SWCNT-junction was produced - a geometry that is extremely difficult to realize with conventional approaches. Although the DNA origami structures were used for assembling and aligning SWCNTs, the method is not restricted to carbon nanotubes; other wires such as silicon nanowires could be assembled as well. In addition to the SWCNTs, silver nanoparticles were assembled into bow-tie antenna configuration. Moreover, the configuration was demonstrated, with numerical simulations, to be suitable for DNA sensing applications. It was also demonstrated that the DNA origami structure itself could be controlled with dendrons and external trigger signals.

In the two final chapters of this thesis, dielectrophoresis was used for controlling nanoparticle assembly. Dielectrophoresis is a versatile tool that can be applied to various micro-and nanoparticles, the only requirement being that the particles have to be polarizable. The method is extremely valuable also in the sense that it can be used for combining the two manufacturing strategies in nanotechnology, namely the top-down and bottom-up approaches. In this thesis a new nanoimprint lithography technique as well as formation of gold nanoparticle chains for sensing applications, both based on dielectrophoresis, were successfully demonstrated.

The DNA origami technique was developed in 2006. Since then the DNA structures have become ever more complicated and research has moved from two- to three-dimensional shapes. However, the formation of 3-D DNA origami structures is a time-consuming process with decreased yields compared to the

2-D counterpart. Therefore, there is still plenty to explore even in the structure formation process. One appealing research direction could be addition of a control mechanism, similar to what was introduced in this thesis with dendrons, in the DNA origami annealing to speed up the process and to ramp up the yields.

Functionalization of the DNA structures has also been a very popular research topic. This is understandable due to the structure programmability offered by DNA and the ability for assembling various kinds of nano-objects with roughly 6 nm resolution. In the future, this high-precision assembly could open up possibilities for using the functionalized DNA origami structure as a calibration standard. The precise positioning also offers many possibilities in the nano-optics related research as was also demonstrated in this thesis with the bow-tie antenna structures. Another appealing application for functionalized DNA origami structures could be cell targeting. There the DNA origami structure would operate as a vessel for cargo delivery into cells.

As a conclusive remark: there is still plenty to explore with DNA origami structures. However, DNA nanotechnology is not only about DNA origamis. Other approaches, such as DNA-tiles [185, 186], are constantly gaining momentum as well. Furthermore, a completely new competitive method has been developed, namely the protein origamis [187]. The future will reveal which of the construction materials, DNA or proteins, will eventually offer the route for realizing functional applications in the commercial scale.

References

[1] Jena library of biological macromolecules, `http://jenalib.fli-leibniz.de/IMAGE_DNA_MODELS.html`

[2] S. Zameroff, F. Bravermann, E. Chargaff, *On the deoxypentose nucleic acids from several microorganisms*, Biochem. Biophys. Acta, **9**, 402, (1952).

[3] Z.G. Kudritskaya, V.I. Danilov, *Quantum mechanical study of bases interactions in various associates in atomic dipole approximation*, J. Theor. Biol., **59**, 303, (1976).

[4] R.L. Ornstein, R. Rein, D.L. Breen, R.D. MacElroy, *An optimized potential function for calculation of nucleic acid interaction energies. I. Base stacking*, Biopolymers, **17**, 2341, (1978).

[5] L. Pauling, *The nature of the chemical bonds*, Cornell Univ. Press, Ithaca, New York, (1978).

[6] S. Burge, G.N. Parkinson, P. Hazel, A. K. Todd, S. Neidle, *Quadruplex DNA: sequence, topology and structure*, Nucl. Acids. Res., **34**, 5402, (2006).

[7] N.C. Seeman, *Nucleic acid junctions and lattices*, J. Theor. Biol., **99**, 237, (1982).

[8] N.C. Seeman, *DNA in a material world*, Nature, **421**, 427, (2003).

[9] N.C. Seeman, *Nanotechnology and the double helix*, Sci. Am., **290**, 64, (2004).

[10] N.R. Kallenbach, R. Ma, N.C. Seeman, *An immobile nucleic acid junction constructed from oligonucleotides*, Nature, **305**, 829, (1983).

[11] J. Chen, N.C. Seeman, *The synthesis from DNA of a molecule with the connectivity of a cube*, Nature, **350**, 631, (1991).

[12] W.M. Shih, J.D. Quispe, G.F. Joyce, *A 1.7-kilobase single-stranded DNA that folds into a nanoscale octahedron*, Nature, **427**, 618, (2003).

[13] R.P. Goodman, I.A.T. Schaap, C.F. Tardin, C.M. Erben, R.M. Berry, C. F. Schmidt, A.J. Turberfield, *Rapid chiral assembly of rigid DNA building blocks for molecular nanofabrication*, Science, **310**, 5754, (2005).

[14] X. Li , X. Yang , J. Qi , N.C. Seeman, *Antiparallel DNA double crossover molecules as components for nanoconstruction*, J. Am. Chem. Soc., **118**, 6131, (1996).

[15] P.W.K. Rothemund, A. Ekani-Nkodo, N. Papadakis, A. Kumar, D.K. Fygenson, E. Winfree, *Design and characterization of programmable DNA nanotubes*, J. Am. Chem. Soc., **126**, 16344, (2004).

[16] T.H. LaBean, H.Yan, J. Kopatsch, F. Liu, E. Winfree, J.H. Reif, N.C. Seeman, *Construction, analysis, ligation, and self-Assembly of DNA triple crossover complexes*, J. Am. Chem. Soc., **122**, 1848, (2000).

[17] Y. Ke, L.L. Ong, W.M. Shih, P. Yin, *Three-dimensional structures self-assembled from DNA bricks*, Science, **338**, 1177, (2012).

[18] P.W.K. Rothemund, *Folding DNA to create nanoscale shapes and patterns*, Nature, **440**, 297, (2006).

[19] CadNano, *http://cadnano.org/gallery.*

[20] S.M. Douglas, H. Dietz, T. Liedl, B. Högberg, F. Graf, W.M. Shih, *Self-assembly of DNA into nanoscale three-dimensional shapes*, Nature, **459**, 414, (2009).

[21] R. Jungmann, T. Liedl, T.L. Sobey, W. Shih, F.C. Simmel, *Isothermal assembly of DNA origami structures using denaturing agents*, J. Am. Chem. Soc., **130**, 10062, (2008).

[22] C.E. Castro, F. Kilchherr, D.-N. Kim, E.L. Shiao, T. Wauer, P. Wortmann, M. Bathe, H. Dietz, *A primer to scaffolded DNA origami*, Nat. Methods, **8**, 221, (2011).

[23] H.R. Drew, R.M. Wing, T. Takano, C. Broka, S. Tanaka, K. Itakura, R.E. Dickerson, *Structure of a B-DNA dodecamer: conformation and dynamics*, Proc. Natl. Acad. Sci. USA, **78**, 2179, (1981).

[24] N.C. Seeman, *DNA double-crossover molecules*, Biochemistry, **32**, 3211, (1993).

[25] Y. Ke, S.M. Douglas, M. Liu, J. Sharma, A. Cheng, A. Leung, Y. Liu, W.M. Shih, H. Yan, *Multilayer DNA origami packed on a square lattice*, J. Am. Chem. Soc., **131**, 15903, (2009).

[26] H. Dietz, S.M. Douglas, W.M. Shih, *Folding DNA into twisted and curved nanoscale shapes*, Science, **325**, 725, (2009).

[27] E.S. Andersen, M. Dong, M.M. Nielsen, K. Jahn, A. Lind-Thomsen, W. Mamdouh, K.V. Gothelf, F. Besenbacher, J. Kjems, *DNA origami design of dolphin-shaped structures with flexible tails*, ACS Nano, **2**, 1213, (2008).

[28] S.M. Douglas, A.H. Marblestone, S. Teerapittayanon, A. Vazquez, C.M. Church, W.M. Shih, *Rapid prototyping of 3D DNA-origami shapes with caDNAno*, Nucleic Acids Res., **37**, 5001, (2009).

[29] Computer-aided engineering of DNA origami, `http://cando-dna-origami.org/`.

[30] S. Woo, P.W.K. Rothemund, *Programmable molecular recognition based on the geometry of DNA nanostructures*, Nat. Chem., **3**, 620, (2011).

[31] A. Kuzyk, K.T. Laitinen, P. Törmä, *DNA origami as a nanoscale template for protein assembly*, Nanotechnology, **20**, 235305, (2009).

[32] S.F.J. Wickham, M. Endo, Y. Katsuda, K. Hidaka, J. Bath, H. Sugiyama, A.J. Turberfield, *Direct observation of stepwise movement of a synthetic molecular transporter*, Nat. Nanotechnol., **6**, 166, (2011).

[33] H.T. Maune, S. Han, R.D. Barish, M. Bockrath, A. Goddard III William, P.W.K. Rothemund, E. Winfree, *Self-assembly of carbon nanotubes into two-dimensional geometries using DNA origami templates*, Nat. Nanotechnol., **5**, 61, (2010).

[34] A.-P. Eskelinen, A. Kuzyk, T.K. Kaltiaisenaho, M.Y. Timmermanns, A.G. Nasibulin, E. Kauppinen, P. Törmä, *Assembly of single-walled carbon nanotubes on DNA-origami templates through streptavidin-biotin interaction*, Small, **7**, 746, (2011).

[35] Z. Zhao, Y. Liu, H. Yan, *DNA origami templated self-assembly of discrete length single wall carbon nanotubes*, Org. Biomol. Chem., **11**, 596, (2013).

[36] N. Stephanopoulos, M. Liu, G.J. Tong, Z. Li, Y. Liu, H. Yan, M.B. Francis, *Immobilization and one-dimensional arrangement of virus capsids with nanoscale precision using DNA origami*, Nano Lett., **10**, 2714, (2010).

[37] A.E. Gerdon, S.S. Oh, K. Hsieh, Y. Ke, H. Yan, H.T. Soh, *Controlled delivery of DNA origami on patterned surfaces*, Small, **5**, 1942, (2009).

[38] B. Ding, Z. Deng, H. Yan, S. Cabrini, R.N. Zuckermann, J. Bokor, *Gold nanoparticle self-similar chain structure organized by DNA origami*, J. Am. Chem. Soc., **132**, 3248, (2010).

[39] S. Pal, Z. Deng, B. Ding, H. Yan, Y. Liu, *DNA-origami-directed self-assembly of discrete silver-nanoparticle architectures*, Angew. Chem. Int. Ed., **49**, 2700, (2010).

[40] A.M. Hung, C.M. Micheel, L.D. Bozano, L.W. Osterbur, G.M. Wallraff, J.N. Cha, *Large-area spatially ordered arrays of gold nanoparticles directed by lithographically confined DNA origami*, Nat. Nanotechnol., **5**, 121, (2010).

[41] G.P. Acuna, F.M. Möller, P. Holzmeister, S. Beater, B. Lalkens, P. Tinnefeld, *Fluorescence enhancement at docking sites of DNA-directed self-assembled nanoantennas*, Science, **338**, 506, (2012).

[42] A. Kuzyk, R. Schreiber, Z. Fan, G. Pardatscher, E.-M. Roller, A. Högele, F.C. Simmel, A.O. Govorov, T. Liedl, *DNA-based self-assembly of chiral plasmonic nanostructures with tailored optical response*, Nature, **438**, 311, (2012).

[43] G.P. Acuna, M. Bucher, I.H. Stein, C. Steinhauer, A. Kuzyk, P. Holzmeister, R. Schreiber, A. Moroz, F.D. Stefani, T. Liedl, F.C. Simmel, P. Tinnefeld, *Distance dependence of single-fluorophore quenching by gold nanoparticles studied on DNA origami*, ACS Nano, **6**, 3189, (2012).

[44] X. Shen, C. Song, J. Wang, D. Shi, Z. Wang, N. Liu, B. Ding, *Rolling up gold nanoparticle-dressed DNA origami into three-dimensional plasmonic chiral nanostructures*, J. Am. Chem. Soc., **134**, 146, (2012).

[45] R. Wang, C. Nuckolls, S.J. Wind, *Assembly of heterogeneous functional nanomaterials on DNA origami scaffolds*, Angew. Chem. Int. Ed., **51**, 11325, (2012).

[46] Z. Zhao, H. Yan, Y. Liu, *A route to scale up DNA origami using DNA tiles as folding staples*, Angew. Chem. Int. Ed., **122**, 1456, (2010).

[47] Z. Li, M. Liu, L. Wang, J. Nangreave, H. Yan, Y. Liu, *Molecular behavior of DNA origami in higher-order self-assembly*, J. Am. Chem. Soc., **132**, 13545, (2010).

[48] W. Liu, H. Zhong, R. Wang, N.C. Seeman, *Crystalline two-dimensional DNA-origami arrays*, Angew. Chem. Int. Ed., **50**, 264, (2011).

[49] E. Czeizler, T. Lempiäinen, P. Orponen, *A design framework for carbon nanotube circuits affixed on DNA origami tiles*, Proc. FNANO11: 8th Annual Conference on Foundations of Nanoscience (Snowbird UT), 186, (2011).

[50] J. Chaste, L. Lechner, P. Morfin, G. Fève, T. Kontos, J.-M. Berroir, D.C. Glattli, H. Happy, P. Hakonen, B. Plaçais, *Single carbon nanotube transistor at GHz frequency*, Nano Lett., **8**, 525, (2008).

[51] M. Rinkiö, A. Johansson, G.S. Paraoanu, P. Törmä, *High-speed memory from carbon nanotube field-effect transistors with high-κ dielectric*, Nano Lett., **9**, 643, (2009).

[52] A. Jorio, M.S. Dresselhaus, G. Dresselhaus, *Carbon nanotubes – advanced topics in synthesis, structure, properties and applications*, Springer, (2008).

[53] H. Dai, *Carbon nanotubes: synthesis, integration, and properties*, Acc. Chem. Res., **35**, 1035, (2002).

[54] M. F. L. De Volder, S. H. Taefick, R. H. Baughmann, A. J. Hart, *Carbon nanotubes: Present and future commercial applications*, Science, **339**, 535, (2013).

[55] J.L. Bahr, E.T. Mickelson, M.J. Bronikowski, *Dissolution of small diameter single-wall carbon nanotubes in organic solvents*, Chem. Commun., **2**, 193, (2000).

[56] R.H. Baughman, A.A. Zakhidov, W.A. de Heer, *Carbon nanotubes–the route toward applications*, Science, **297**, 787, (2002).

[57] J. Liu, A.G. Rinzler, H. Dai, J.H. Hafner, R.K. Bradley, P.J. Boul, A. Lu, T. Iverson, K. Shelimov, C.B. Huffman, F. Rodriguez-Macias, Y.-S. Shon, T.R. Lee, D.T. Colbert, R.E. Smalley, *Fullerene pipes*, Science, **22**, 1253, (1998).

[58] J. Chen, M.A. Hamon, H. Hu, Y. Chen, A.M. Rao, P. C. Eklund, R.C. Haddon, *Solution properties of single-walled carbon nanotubes*, Science, **282**, 95, (1998).

[59] S. Ramesh, L.M. Ericson, V.A. Davis, R.K. Saini, C. Kittrell, M. Pasquali, W.E. Billups, W.W. Adams, R.H. Hauge, R.E. Smalley, *Dissolution of pristine single walled carbon nanotubes in superacids by direct protonation*, J. Phys. Chem., **108**, 8794, (2004).

[60] J. Zhu, M. Yudasaka, M. Zhang, S. Iijima, *Dispersing carbon nanotubes in water: A noncovalent and nonorganic Way*, Phys. Chem. B., **108**, 11317, (2004).

[61] K. Kurppa, H. Jiang, G.R. Szilvay, A.G. Nasibulin, E.I. Kauppinen, M.B. Linder, *Controlled hybrid nanostructures through protein-mediated noncovalent functionalization of carbon nanotubes*, Angew. Chem. Int. Ed., **119**, 6566, (2007).

[62] M.J. O'Connell, P. Boul, L.M. Ericson, C. Huffman, Y. Wang, E. Haroz, C. Kuper, J. Tour, K.D. Ausman, R.E. Smalley, *Reversible water-solubilization of single-walled carbon nanotubes by polymer wrapping*, Chem. Phys. Lett., **342**, 265, (2001).

[63] V.C. Moore, M.S. Strano, E.H. Haroz, R.H. Hauge, R.E. Smalley, *Individually suspended single-walled carbon nanotubes in various surfactants*, Nano Lett., **3**, 1379, (2003).

[64] R. Shvartzman-Cohen, Y. Levi-Kalisman, E. Nativ-Roth, R. Yerushalmi-Rosen, *Generic approach for dispersing single-walled carbon nanotubes: the strength of a weak interaction*, Langmuir, **20**, 6085, (2004).

[65] M.J. O'Connell, S.M. Bachilo, C.B. Huffman, V.C. Moore, M.S. Strano, E.H. Haroz, K.L. Rialon, P.J. Boul, W.H. Noon, C. Kittrell, J. Ma, R.H. Hauge, R.B. Weisman, R.E. Smalley, *Band gap fluorescence from individual single-walled carbon nanotubes*, Science, **297**, 5581, (2002).

[66] P.W. Barone, S. Baik, D.A. Heller, M.S. Strano, *Near-infrared optical sensors based on single-walled carbon nanotubes*, Nat. Mater., **4**, 86, (2004).

[67] C. Staii, M. Chen, A. Gelperin, *DNA-decorated carbon nanotubes for chemical Sensing*, Nano Lett., **5**, 1774, (2005).

[68] E.S. Jeng , A.E. Moll , A.C. Roy , J.B. Gastala, M.S. Strano, *Detection of DNA hybridization using the near-infrared band-gap fluorescence of single-walled carbon nanotubes*, Nano Lett., **6**, 371, (2006).

[69] A. Star, E. Tu, J. Niemann, J.-C.P. Gabriel, C.S. Joiner, C. Valcke, *Label-free detection of DNA hybridization using carbon nanotube network field-effect transistors*, PNAS, **103**, 921, (2005).

[70] Y. Lu, S. Bangsaruntip, X. Wang, L. Zhang, Y. Nishi, H. Dai, *DNA Functionalization of carbon nanotubes for ultrathin atomic layer deposition of high κ dielectrics for nanotube transistors with 60 mV/decade wwitching*, J. Am. Chem. Soc., **128**, 3518, (2006).

[71] N.W.S. Kam, M. O'Connell, J.A. Wisdom, H. Dai, *Carbon nanotubes as multifunctional biological transporters and near-infrared agents for selective cancer cell destruction*, Proc. Natl. Acad. Sci. U. S. A., **102**, 11600, (2005).

[72] R.R. Johnson, A.T.C. Johnson, M.L. Klein, *The nature of DNA-base-carbon-nanotube interactions*, Small, **6**, 31, (2010).

[73] R.R. Johnson , A.T.C. Johnson , M.L. Klein, *Probing the structure of DNA-carbon nanotube hybrids with molecular dynamics*, Nano Lett., **8**, 69, (2008).

[74] F. Albertorio, M.E. Hughes, J.A. Golovchenko, D. Branton, *Base dependent DNA-carbon nanotube interactions: activation enthalpies and assembly-disassembly control*, Nanotechnology, **20**, 395101, (2009).

[75] M. Zheng, A. Jagota, E.D. Semke, B.A. Diner, R.S. Mclean, S.R. Lustig, R.E. Richardson, N.G. Tassi, *DNA-assisted dispersion and separation of carbon nanotubes*, Nat. Mater., **2**, 338, (2003).

[76] X. Tu, S. Manohar, A. Jagota, M. Zheng, *DNA sequence motifs for structure-specific recognition and separation of carbon nanotubes*, Nature, **460**, 250, (2009).

[77] R.R. Johnson, A. Kohlmeyer, A.T.C. Johnson, M.L. Klein, *Free energy landscape of a DNA-carbon nanotube hybrid using replica exchange molecular dynamics*, Nano Lett., **9**, 537, (2009).

[78] A. Moisala, A.G. Nasibulin, D.P. Brown, H. Jiang, L. Khriachtchev, E. I. Kauppinen, *Single-walled carbon nanotube synthesis using ferrocene and*

iron pentacarbonyl in a laminar flow reactor, Chem. Eng. Sci., **61**, 4393, (2006).

[79] M.S. Dresselhaus, G. Dresselhaus, R. Saito, A. Jorio, *Raman spectroscopy of carbon nanotubes*, Phys. Rep., **409**, 47, (2005).

[80] S.R. Vogel, M.M. Kappes, F.K. Hennrich, C. Richert, *An unexpected new optimum in the structure space of DNA solubilizing single-walled carbon nanotubes*, Chem.–Eur. J., **13**, 1815, (2007).

[81] P. O'Neill, P.W.K. Rothemund, A. Kumar, D.K. Fygenson, *Sturdier DNA nanotubes via ligation*, Nano Lett., **6**, 1379, (2006).

[82] A. Kuzyk, B. Yurke, J.J. Toppari, V. Linko, P. Törmä, *Dielectrophoretic trapping of DNA origami*, Small, **4**, 447, (2008).

[83] J. Kong, N.R. Franklin, C. Zhou, M.G. Chapline, S. Peng, K. Cho, H. Dai, *Nanotube molecular wires as chemical sensors*, Science, **287**, 622, (2000).

[84] L. Cognet, D.A. Tsyboulski, J.-D.R. Rocha, C.D. Doyle, J.M. Tour, R.B. Weisman, *Stepwise quenching of exciton fluorescence in carbon nanotubes by single-molecule reactions*, Science, **316**, 1465, (2007).

[85] D. Brunel, A. Mayer, T. Melin, *Imaging the operation of a carbon nanotube charge sensor at the nanoscale*, ACS Nano, **4**, 5978, (2010).

[86] T. Hertel, R.E. Walkup, P. Avouris, *Deformation of carbon nanotubes by surface van der Waals forces*, Phys. Rev. B., **58**, 13870, (1998).

[87] M.S. Fuhrer, J. Nygård, L. Shih, M. Forero, Y. Yoon, M.S.C. Mazzoni, H. J. Choi, J. Ihm, S. G. Louie, A. Zettl, P. L. McEuen, *Crossed nanotube junctions*, Science, **288**, 494, (2000).

[88] G. Bellot, M.A. McClintock, C. Lin, W. Shih, *Recovery of intact DNA nanostructures after agarose gel-based separation*, Nano Lett., **8**, 192, (2011).

[89] A.G. Brolo, *Plasmonics for future biosensors*, Nat. Photonics, **6**, 709, (2012).

[90] B.E.A. Saleh, M.C. Teich, *Fundamentals of photonics*, John Wiley & Sons Ltd, 2nd. edition, (2007).

[91] U. Kreipig, M. Vollmer, *Optical properties of metal clusters*, Springer, (1995).

[92] S. V. Gaponenko, *Introduction to nanophotonics*, Cambridge University Press, 1st. edition, (2010).

[93] H. Ehrenreich, H.R. Philipp, *Optical properties of Ag and Cu*, Phys. Rev., **128**, 1622, (1962).

[94] L. Novotny, B. Hecht, *Principles of nano-optics*, Cambridge University Press, (2006).

[95] A.V. Zayats, I.I. Smolyaninov, A.A. Maradudin, *Nano-optics of surface plasmon polaritons*, Physics Reports, **408**, 131, (2005).

[96] S. Nie, S. R. Emory, *Probing single molecules and single nanoparticles by surface-enhanced raman scattering*, Science, **275**, 1102, (1997).

[97] J.-H. Song, T. Atay, S. Shi, H. Urabe, A.V. Nurmikko, *Large enhancement of fluorescence efficiency from CdSe/ZnS quantum dots induced by resonant coupling to spatially controlled surface plasmons*, Nano Lett., **5**, 1557, (2005).

[98] D. Sarid, W. Challener, *Modern introduction to surface plasmons*, Cambridge University Press, (2010).

[99] C. Kittel, *Introduction to solid state physics*, John Wiley & Sons Ltd, 8th edition (2005).

[100] E. Prodan, C. Radloff, N.J. Halas, P. Nordlander, *A hybridization model for the plasmon responce of complex nanostructures*, Science, **302**, 5644, (2003).

[101] E. Prodan, P. Nordlander, *Plasmon hybridization in spherical nanoparticles*, J. Chem. Phys., **120**, 5444, (2004).

[102] P. Nordlander, C. Oubre, E. Prodan, K. Li, M.I. Stockman, *Plasmon hybridization in nanoparticle dimers*, Nano Lett., **4**, 899, (2004).

[103] W. Rechberger, A. Hohenau, A. Leitner J.R. Krenn, B. Lamprecht, F.R. Aussenegg, *Optical properties of two interacting gold nanoparticles*, Opt. Commun., **220**, 137, (2003).

[104] P.K. Jain, M.A. El-Sayed, *Plasmonic coupling in noble metal nanostructures*, Chem. Phys. Lett., **487**, 153, (2010).

[105] P.K. Jain, W. Huang, M.A. El-Sayed, *On the universal scaling behavior of the distance decay of plasmon coupling in metal nanoparticle pairs: a plasmon ruler equation*, Nano Lett., **7**, 2080, (2007).

[106] J. Yan, S. Gao, *Plasmon resonances in linear atomic chains: free-electron behavior and anisotropic screening of d electrons*, Phys. Rev. B, **78**, 235413, (2008).

[107] J. Zuloaga, E. Prodan, P. Nordlander, *Quantum description of the plasmon resonances of a nanoparticle dimer*, Nano Lett., **9**, 887, (2009).

[108] L.V. Brown, H. Sobhani, J.B. Lassiter, P. Nordlander, N.J. Halas, *Heterodimers: plasmonic properties of mismathced nanoparticle pairs*, ACS Nano, **4**, 819, (2010).

[109] O. Peña-Rodrìguez, U. Pal, M. Campoy-Quiles, L. Rodrìguez-Fernàndez, M. Garriga, M. I. Alonso, *Enhanced fano resonance in asymmetrical Au:Ag heterodimers*, Phys. Chem. C, **115**, 6410, (2011).

[110] A.M. Schwartzberg, T.Y. Olson, C.E. Talley, J.Z. Zhang, *Synthesis, characterization, and tunable optical properties of hollow gold nanospheres*, J. Phys. Chem. B, **110**, 19935, (2006).

[111] Y. Xiong, H. Cai, B.J. Wiley, J. Wang, M.J. Kim, Y. Xia, *Synthesis and mechanistic study of palladium nanobars and nanorods*, J. Am. Chem. Soc., **12**, 3665, (2007).

[112] M.J. Mulvihill, X.Y. Ling, J. Henzie, P. Yang, *Anisotropic etching of silver nanoparticles for plasmonic structures capable of single-particle SERS*, J. Am. Chem. Soc., **132**, 268, (2009).

[113] B.J. Wiley, S.H. Im, Z.-Y. Li, J. McLellan, A. Siekkinen, Y. Xia, *Maneuvering the surface plasmon resonance of silver nanostructures through shape-controlled synthesis*, J. Phys. Chem. B, **110**, 15666, (2006).

[114] Y.J. Min, M. Akbulut, K. Kristiansen, Y. Golan, J. Israelachvili, *The role of interparticle and external forces in nanoparticle assembly*, Nat. Mater., **7**, 527, (2008).

[115] E.V. Shevchenko, D.V. Talapin, N.A. Kotov, S. O'Brien, C.B. Murray, *Structural diversity in binary nanoparticle superlattices*, Nat. Mater., **439**, 55, (2006).

[116] A. Badia, S. Singh, L. Demers, L. Cuccia, G.R. Brown, R.B. Lennox, *Self-assembled monolayers on gold nanoparticles*, Chem.–Eur. J., **2**, 359, (1996).

[117] A.C. Templeton, W.P. Wuelfing, R.W. Murray, *Monolayer-protected cluster molecules*, Acc. Chem. Res., **33**, 27, (2000).

[118] K. Aslan, V.H. Pèrez-Luna, *Surface modification of colloidal gold by chemisorption of alkanethiols in the presence of a nonionic surfactant*, Langmuir, **18**, 6059, (2002).

[119] C.A. Mirkin, R.L. Letsinger, R.C. Mucic, J.J. Storhoff, *A DNA-based method for rationally assembling nanoparticles into macroscopic materials*, Nature, **382**, 607, (1996).

[120] A.P. Alivisatos, K.P. Johnsson, X. Peng, T.E. Wilson, C.J. Loweth, M.P. Bruchez Jr, P.G. Schultz, *Organization of 'nanochrystal molecules' using DNA*, Nature, **382**, 609, (1996).

[121] C.J. Loweth, W.B. Caldwell, X. Peng, A.P. Alivisatos, P.G. Schultz, *DNA-based assembly of gold nanocrystals*, Angew. Chem. Int. Ed., **38**, 1808, (1999).

[122] J. Sharma, R. Chhabra, A. Cheng, J. Brownell, Y. Liu, H. Yan, *self-assembly of DNA tubules through integration of gold nanoparticles*, Science, **323**, 112, (2009).

[123] J.D. Le, Y. Pinto, N.C. Seeman, K. Musier-Forsyth, T.A. Taton, R.A. Kiehl, *DNA-templated self-assembly of metallic nanocomponent arrays on a surface*, Nano Lett., **4**, 2343, (2004).

[124] M.M. Maye, M.T. Kumara, D. Nykypanchuk, W.B. Sherman, O. Gang, *Switching binary states of nanoparticle superlattices and dimer clusters by DNA strands*, Nat. Nanotechnol., **5**, 116, (2010).

[125] S.J. Tan, M.J. Campolongo, D. Luo, W. Cheng, *Building plasmonic nanostructures with DNA*, Nat. Nanotechnol., **6**, 268, (2011).

[126] M.M. Maye, D. Nykypanchuk, M. Cuisinier, D. van der Lelie, O. Gang, *Stepwise surface encoding for high-throughput assembly of nanoclusters*, Nat. Mater., **8**, 388, (2009).

[127] J.H. Lee, D.P. Wernette, M.V. Yigit, J. Liu, Z. Wang, Y. Lu, *Site-specific control of distances between gold nanoparticles using phosphorothioate anchors on DNA and a short bifunctional molecular fastener*, Angew. Chem. Int. Ed., **119**, 9164, (2007).

[128] J.-S. Lee, A.K.R. Lytton-Jean, S.J. Hurst, C.A. Mirkin, *Silver nanoparticle-oligonucleotide conjugates based on DNA with triple cyclic disulfide moieties*, Nano Lett., **7**, 2112, (2007).

[129] J.A. Dougan, C. Karlsson, W.E. Smith, D. Graham, *Enhanced oligonucleaotide-nanoparticle conjugate stability using thiotic acid modified oligonucleotides*, Nucl. Acids Res., **35**, 3668, (2007).

[130] S. Pal, J. Sharma, H. Yana, Y, Liu, *Stable silver nanoparticle-DNA conjugates for directed self-assembly of core-satellite silver-gold nanoclusters*, Chem. Commun., 6059, (2009).

[131] J.I.L. Chen, Y.C. Chen, D.S. Ginger, *Plasmonic nanoparticle dimers for optical sensing of DNA in complex media*, J. Am. Chem. Soc, **132**, 98195, (2010).

[132] E. D. Palik, *Handbook of Optical Constants of Solids: Index*, Academic Press, (1991).

[133] D.A. Tomalia, H. Baker, J.R. Dewald, M. Hall, G. Kallos, S. Martin, J. Roeck, J. Ryder, P. Smith, *A new class of polymers: Starburst-dendritic macromolecules*, Polym. J., **17**, 117, (1985).

[134] G.R. Newkome, Z.Q. Yao, G.R. Baker, V.K Gupta, *Cascade molecules: a new approach to micelles, A[27]-arborol.*, J. Org. Chem., **50**, 2003, (1985).

[135] B. Klajnert, M. Bryszewska, *Dendrimers: properties and applications*, Acta Biochim. Pol., **48**, 199, (2001).

[136] M.A. Kostiainen, J.G. Hardy, D.K. Smith, *High-affinity multivalent DNA binding by using low-molecular-weight dendrons*, Angew. Chem. Int. Ed., **44**, 2556, (2005).

[137] M.A. Kostiainen, H. Rosilo, *Low-molecular-weight dendrons for DNA binding and release by reduction-triggered degradation of multivalent interactions*, Chem. Eur. J., **15**, 5656, (2009).

[138] M.A. Kostiainen, G.R. Szilvay, D.K. Smith, M.B. Linder, O. Ikkala *Multivalent dendrons for high-affinity adhesion of proteins to DNA*, Angew. Chem. Int. Ed., **45**, 3538, (2006).

[139] M.A. Kostiainen, D.K. Smith, O. Ikkala *Optically triggered release of DNA from multivalent dendrons by degrading and charge-switching multivalency*, Angew. Chem. Int. Ed., **46**, 7600, (2007).

[140] W.R. Browne, B.L. Feringa, *Making molecular machines work*, Chem. Eur. J., **1**, 25, (2006).

[141] G. ten Brinke, J. Ruokolainen, O. Ikkala, *Supramolecular materials based On hydrogen-bonded polymers*, Adv. in Polym. Science, **207**, 113, (2007).

[142] Y.-M. Go, D. P. Jones, *Redox compartmentalization in eukaryotic cells*, Biochim. Biophys. Acta, **1780**, 1273, (2008).

[143] S.Y. Chou, P.R. Krauss, P.J. Renstrom, *Imprint lithography with 25-nanometer resolution*, Science, **5**, 85, (1996).

[144] S.Y. Chou, P.R. Krauss, P.J. Renstrom , *Nanoimprint lithography*, J. Vac. Sci. Technol. B, **14**, 4129, (1996).

[145] S.Y. Chou, C. Keimel, J. Gu, *Ultrafast and direct imprint of nanostructures in silicon*, Nature, **417**, 835, (2002).

[146] K.H. Hsu, P.L. Schultz, P.M. Ferreira, N.X. Fang, *Letter electrochemical nanoimprinting with solid-state superionic stamps*, Nano Lett., **7**, 446, (2007).

[147] J.M. Kontio, H. Husu, J. Simonen, M. J. Huttunen, J. Tommila, M. Pessa, M. Kauranen, *Nanoimprint fabrication of gold nanocones with ~10 nm tips for enhanced optical interactions*, Opt. Lett., **34**, 1979, (2009).

[148] A. Kumar, G.M. Whitesides, *Features of gold having micrometer to centimeter dimensions can be formed through a combination of stamping with an elastomeric stamp and an alkanethiol "ink" followed by chemical etching*, Appl. Phys. Lett., **63**, 2002, (1993).

[149] H.A. Pohl, *The motion and precipitation of suspensoids in divergent electric fields*, J. Appl. Phys., **22**, 869, (1951).

[150] J.S. Shim, Y.-H. Yun, M.J. Rust, J.Do, V. Shanov, M.J. Schulz, C.H. Ahn, *MEMS 2008*, Tucson, AZ, USA, January 13-17 (2008).

[151] A.E. Cohen, *Control of nanoparticles with arbitrary two-dimensional force fields*, Phys. Rev. Lett., **94**, 118102, (2005).

[152] H.O. Jacobs, G.M. Whitesides, *Submicrometer patterning of charge in thin-film electrets*, Science, **291**, 1763, (2001).

[153] R.C. Hayward, D.A. Saville, I.A. Aksay, *Electrophoretic assembly of colloidal crystals with optically tunable micropatterns*, Nature, **404**, 56, (2000).

[154] S. Kumar, Y.-K. Seo, G.-H. Kim, *Focused patterning of nanoparticles by controlling electric field induced particle motion*, Appl. Phys. Lett., **94**, 053104, (2009).

[155] P.Y. Chiou, A.T. Ohta, M.C. Wu, *Massively parallel manipulation of single cells and microparticles using optical images*, Nature, **436**, 370, (2005).

[156] L. Jauffred , A.C. Richardson, L.B. Oddershede, *Three-dimensional optical control of individual quantum dots*, Nano Lett., **8**, 3376, (2008).

[157] M. Righini, A.S. Zelenina, C. Girard, R. Quidant, *Parallel and selective trapping in a patterned plasmonic landscape*, Nature Phys., **3**, 447, (2007).

[158] Y. Rondelez, G. Tresset, T. Nakashima, Y. Kato-Yamada, H. Fujita, S. Takeuchi, H. Noji, *Highly coupled ATP synthesis by F1-ATPase single molecules*, Nat. Phys., **433**, 773, (2004).

[159] M. Dienerowitz, M. Mazilu, P.J. Reece, T.F. Krauss, K. Dholakia, *Optical vortex trap for resonant confinement of metal nanoparticles*, Opt. Express, **16**, 4991, (2008).

[160] P. Y. Chiou, *Manipulating nanoparticles and macromolecules with light patterned microfluidic flow*, Proc. IEEE Int. Conf. Nano/Micro Eng. Mol. Sys., 1204, (2008).

[161] A. Vijayaraghavan, S. Blatt, D. Weissenberger, M. Oron-Carl, F. Hennrich, D. Gerthsen, H. Hahn, R. Krupke, *Ultra-large-scale directed assembly of single-walled carbon nanotube devices*, Nano Lett., **7**, 1556, (2007).

[162] R.W. Clarke, J.D. Piper, L. Ying, D. Klenerman, *Surface conductivity of biological macromolecules measured by nanopipette dielectrophoresis*, Phys. Rev. Lett., **98**, 198102, (2007).

[163] S. Elliot, *The physics and chemistry of solids*, John Wiley & Sons Ltd, (2000).

[164] Y. Kayanuma, *Quantum-size effects of interacting electrons and holes in semiconductor microcrystals with spherical shape*, Phys. Rev. B., **38**, 9797, (1988).

[165] R.J. Moerland, H.T. Rekola, G. Sharma, A.-P. Eskelinen, A.I. Väkeväinen, P. Törmä, *Surface plasmon polariton-controlled tunable quantum-dot emission*, Appl. Phys. Lett, **100**, 221111, (2012).

[166] J. Bang, H. Yang, P.H. Holloway, *Enhanced and stable green emission of ZnO nanoparticles by surface segregation of Mg*, Nanotechnology, **17**, 973, (2006).

[167] Y. Wang, N. Herron, *Nanometer-sized semiconductor cluster-materials synthesis, quantum size effect, and photophysical properties*, J. Phys. Chem., **95**, 525, (1991).

[168] D. Bera, L. Qian, T.-K. Tseng, P.H. Holloway, *Quantum dots and their multimodal applications: a review*, Materials, **3**, 2260, (2010).

[169] X.G. Peng, M.C. Schlamp, A.V. Kadavanich, A.P. Alivisatos, *Epitaxial growth of highly luminescent CdSe/CdS core/shell nanocrystals with photostability and electronic accessibility*, J. Am. Chem. Soc., **119**, 7019, (1997).

[170] B.G. Streetman, B. Sanjay, *Solid state electronic Devices*, New Jersey: Prentice Hall., 5th edition, (2000).

[171] T.B. Jones, *Electromechanics of particles*, Cambridge university press, (1995).

[172] T.B. Jones, *Basic theory of dielectrophoresis and electrorotation*, IEEE EMBS Magazine, **22**, 33, (2003).

[173] L. Zhenga, J.P. Brodyb, P.J. Burke, *Electronic manipulation of DNA, proteins, and nanoparticles for potential circuit assembly*, Biosens. Bioelectron., **20**, 606, (2004).

[174] M. Washizu, *Equivalent multipole-moment theory for dielectrophoresis and electrorotation in electromagnetic field*, J. Electrostat., **62**, 15, (2004).

[175] X. Wang, X.-B. Wang, P.R.C. Gascoyne, *General expressions for dielectrophoretic force and electrorotational torque derived using the Maxwell stress tensor method*, J. Electrostat., **39**, 277, (1997).

[176] A. Castellanos, A. Ramos, A. Gonzalez, N.G. Green, H. Morgan, *Electrohydrodynamics and dielectrophoresis in microsystems: scaling laws*, J. Phys. D: Appl. Phys., **36**, 2584, (2003).

[177] H.A. Pohl, *Dielectrophoresis: The behavior of neutral matter in nonuniform electric fields*, Cambridge university press, (1978).

[178] E. Katz, I. Willner, *Integrated nanoparticle-biomolecule hybrid systems: synthesis, properties, and applications*, Angew. Chem. Int. Ed., **43**, 6042, (2004).

[179] H. Wohltjen, A.W. Snow, *Colloidal metal-insulator-metal ensemble chemiresistor sensor*, Anal. Chem., **70**, 2856, (1998).

[180] S.I. Khondaker, K. Luo, Z. Yao, *The fabrication of single-electron transistors using dielectrophoretic trapping of individual gold nanoparticles* , Nanotechnology, **21**, 095204, (2010).

[181] L. Bernard, M. Calame, S.J. van der Molen, J. Liao, C. Schönenberger, *Controlled formation of metallic nanowires via Au nanoparticle ac trapping*, Nanotechnology, **18**, 235202, (2007).

[182] C.T. Harrower, D.R. Oliver, *Electronic transport in dielectrophoretically grown nanowires*, J. Mater. Sci., **41**, 8166, (2006).

[183] J.M. Slocika, S.N. Kima, T. Auvila, E.R. Goldmanb, J. Liub, R.R. Naik, *Single domain antibody templated nanoparticle resistors for sensing*, Biosens. Bioelectron., **25**, 1908, (2010).

[184] J. Lee, S. Mubeen, C.M. Hangarter, A. Mulchandani, W. Chen, N.V. Myung, *Selective and rapid room temperature detection of H2S using gold nanoparticle chain arrays*, Electroanalysis, **23**, 2623, (2011).

[185] P.R. O'Neill, K. Young, D. Schiffels, D. K. Fygenson, *Few-atom fluorescent silver cluster assembly at programmed sites on DNA nanotubes*, Nano Lett., **11**, 5464, (2012).

[186] B. Wei, M. Dai, P. Yin, *Complex shapes self-assembled from single-stranded DNA tiles*, Nature, **485**, 623, (2012).

[187] M. Peplow, *Protein gets in on DNA's origami act*, Nature news, (2013).

BUSINESS +
ECONOMY

ART +
DESIGN +
ARCHITECTURE

SCIENCE +
TECHNOLOGY

CROSSOVER

DOCTORAL
DISSERTATIONS